

**On the Origin of Micro-Cracking in Zn-Coated Press Hardened  
Steels**

**On the Origin of Micro-Cracking in Zn-Coated Press Hardened Steels**

**By**

**Khatereh Maleki**

A Thesis

Submitted to the School of Graduate Studies

In Partial Fulfillment of the Requirements

For the Degree

Master of Applied Science in Materials Science and Engineering

McMaster University

© Copyright by Khatereh Maleki, August 2019

Title: On the Origin of Micro-Cracking in Zn-Coated Press Hardened Steels

Author: Khatereh Maleki (McMaster University)

Supervisors: Dr. Nabil D. Bassim and Dr. Joseph R. McDermid

Pages: 125

## Abstract

Zn-coated press hardened steels are in high demand in the automotive industry because their high strength enhances passenger safety while supplying cathodic corrosion protection. However, micro-crack formation after thermomechanical processing is an issue that limits full deployment. One of the most commonly used mechanisms for micro-cracking in Zn-coated press hardened steels (PHS) is liquid metal embrittlement (LME). During hot press forming, LME is induced by the penetration of liquid zinc along the grain boundaries of the substrate which negatively impacts mechanical properties by causing premature failure of the part. The mechanism of LME is well-established; however, it can not be applied to all cases of embrittlement in Zn-coated PHS. Therefore, the objective was to determine a new mechanism for micro-cracking in Zn-coated PHS. The focus was to address the relationship between the origin of micro-cracking and final coating microstructure created by an inward diffusion between the Zn-based overlay and underlying ferrous substrate as a function of annealing time.

Zn-coated 22MnB5 steel sheets were annealed at 900 °C for different annealing times (30 s, 60 s, 120 s, 180 s, 240 s, 300 s, 420 s, 600 s, 780 s), and were then planar or U-shaped die-quenched with an average cooling rate of 100 °Cs<sup>-1</sup>, resulting in a fully martensitic substrate microstructure. In order to precisely determine the zinc distribution and degree of Zn penetration into the bulk substrate, four sets of samples were examined. The first set of samples were annealed for 30 s (the shortest time) and 780s (the longest time) and die-quenched while the second set comprised tensile specimens from the 30 s and 780 s annealing times which were subsequently pulled to failure. The third and fourth set of samples were selected from two areas (top surface and outer

wall surface) on the U-shaped die-quenched samples that were annealed for 30 s and 780 s. U-shaped die-quenched DHPF allowed for the production of in-situ micro-cracks during forming rather than the ex-situ cracks formed during tensile testing of the planar die quench samples. The PAGBs of the substrate and GBs of the  $\alpha$ -Fe(Zn) coating were studied before tensile testing to observe how zinc diffusion in these regions can contribute to later micro-crack formation. The micro-crack tips were investigated after tensile testing and micro-crack formation.

Scanning electron microscopy (SEM), X-ray diffraction (XRD) and energy-dispersive X-ray spectroscopy (EDS) results showed that, by increasing annealing time, the zinc concentration in the coating decreased while the coating thickness increased parabolically. The coating microstructure underwent a transformation from a dual phase ( $\Gamma$ -Fe<sub>3</sub>Zn<sub>10</sub> +  $\alpha$ -Fe(Zn)) layer to a single-phase layer ( $\alpha$ -Fe(Zn)) after annealing for 300s. Electron backscatter diffraction (EBSD) and scanning transmission electron microscopy coupled with electron energy loss spectroscopy (STEM-EELS) were performed on four sets of samples. EBSD determined that for a  $\alpha$ -Fe(Zn) or dual-phase ( $\Gamma$ -Fe<sub>3</sub>Zn<sub>10</sub> +  $\alpha$ -Fe(Zn)) coating layer, a transition layer of Zn-enriched martensite (Zn- $\alpha'$ ) was present in the as-quenched samples. STEM-EELS results for both ex-situ and in-situ micro-cracking, in the absence or presence of tension, indicated zinc enrichment in the PAGBs, GBs and, at the micro-crack tip in the PAGB region for both the 30 s and 780 s DHPF samples. In addition, EELS semi-quantitative analysis of zinc concentration in the  $\alpha$ -Fe(Zn) GBs and in the coincident PAGBs implied the presence of a thin  $\alpha$ -Fe(Zn) layer in these regions.

Based upon the current results, a new mechanism was proposed for the origin of micro-cracking in Zn-coated 22MnB5 DHPF. A coincident PAGB in the substrate and a coincident GB in the  $\alpha$ -Fe(Zn) became Zn-enriched and a thin layer of  $\alpha$ -Fe(Zn) formed along the PAGBs as a result of

the solid-state diffusion of zinc during austenitization annealing at 900 °C. During tensile testing, the micro-crack propagated along the Zn-enrichment weakened coincident PAGBs.

## Acknowledgements

First and Foremost, I would like to express my sincere gratitude to my supervisors Dr. Joseph McDermid and Dr. Nabil Bassim. I am truly appreciative of their unconditionally guidance, support, and encouragement from the initial to the final level enabled me to develop an understanding of this research. It was an honour and pleasure to be able to work with them throughout my project.

I would also like to thank many people for their training and technical knowledge. I would like to thank Dr. Moisei Bruhis, Dr. Elizabeth McNally, John Thomson and Doug Culley for their technical assistance, Chris Butcher, Travis Casagrande, Natalie Hamada, and Andy Duft for electron microscopy training, Victoria Jarvis and Dr. Jim Britten for X-ray diffraction measurements. I would like to acknowledge ArcelorMittal Dofasco for the provision of the steels used in this research and the International Zinc Association - Galvanized Autobody Partnership (IZA-GAP) for their financial support. I would also like to thank the members of my both research groups for their support and suggestions.

At last but not least, I would like to thank my parents, my siblings and my friends for their constant support, loving and inspiration throughout my graduate studies.

# Table of Contents

1. Introduction	1
2. Literature Review	2
2.1 Continuous Galvanizing Line	2
2.2 Direct Hot Press Forming (DHPF)	4
2.3 Fe-Zn Phase Transformations	5
2.4 High Temperature Fe-Zn Phase Evolution	9
2.5 Micro-Cracking Mechanisms	11
2.5.1 Liquid Metal Embrittlement (LME)	11
2.5.2 Liquid Metal Embrittlement (LME) Mechanisms	13
2.5.3 Solid Metal Embrittlement (SME)	17
2.6 LME and SME in Zn-Coated Press Hardened Steel	20
2.7 Diffusion of Zn in Steels	22
2.8 Mechanical Properties of Zn-Coated PHS	26
2.9 Corrosion Properties Zn-Coated Press Hardened Steels	30
2.10 Weldability and Paintability Properties of Zn-Coated Press Hardened Steels	31
3. Research Objectives	32

4. Experimental Methods	34
4.1 Steel Chemistry and Sample Preparation	34
4.2 Heat Treatments	35
4.2.1. Coating Microstructural Evolution	35
4.2.2. Planar die Direct Hot Press Forming (DHPF)	37
4.2.3. U-Shaped Die Direct Hot Press Forming (DHPF)	39
4.3 Tensile Testing	41
4.3.1. Planar Die DHPF Samples	41
4.3.2. U-Shaped DHPF Samples	41
4.4 Digital Image Correlation (DIC) in Three Dimensions (3D) Analysis	42
4.5 X-Ray Diffraction (XRD)	44
4.6 Electron Microscopy (SEM-EBSD) Sample Preparation	44
4.7 Scanning Electron Microscopy (SEM) Analysis of the Coating Microstructure	46
4.8 Scanning Auger Microscopy (SAM)	47
4.9 Electron Backscattered Diffraction (EBSD)	48
4.10 Transmission Electron Microscopy (TEM) Sample Preparation by Focused Ion Beam (FIB)	
Milling	50
4.11 Scanning Transmission Electron Microscopy - Electron Energy Loss Spectroscopy (STEM-EELS)	50

5. Results	51
5.1 SEM Analysis of As-Received Uncoated and Coated 22MnB5 Steel	51
5.2 SEM and EDS Related Analysis of the Coating Microstructural Evolution after Heat Treatment and Quenching Processes	54
5.3 XRD Analysis of the Coating Microstructural Evolution After Heat Treatment and Cooling Processes	58
5.4 Tensile Tested Samples	59
5.5 SEM Analysis of As-Quenched and Tensile Tested Samples	61
5.6 EBSD Analysis on As-Quenched Samples	64
5.7 EBSD Analysis on As-Quenched Samples After Tensile Testing	65
5.8 Prior Austenite Grain Boundary Detection	66
5.9 STEM-EELS Analysis on GBs Before Tensile Testing	68
5.10 STEM-EELS Analysis on GBs after Tensile Testing and Formation of Micro-Cracks	72
5.11 SEM and EDS Analysis on the Coating Microstructural Evolution for U-Shaped Die-Quenched Samples	75
5.12 EBSD Analysis of U-Shaped Press Hardened Samples	81
5.13 STEM-EELS Analysis on GBs of U-shaped Die-Quenched Samples	82
6. Discussion	89
6.1 Coating Microstructural Evolution	89

6.1 Planar Die and U-shaped DHPF Process	92
6.1.1 Ex-Situ Micro-Cracking	92
6.1.2 In-Situ Micro-Cracking	96
7. Conclusions	97
8. References	99

## Table of Figures

Figure 2. 1: Sendzimir continuous galvanizing line [9].	3
Figure 2. 2: Schematic of the direct and indirect hot stamping process [2].	5
Figure 2. 3: Fe–Zn binary phase diagram [1].	6
Figure 2. 4: A schematic diagram of Fe-Zn phase layer formation in a 0.00 wt.% Al-Zn galvanizing [8].	7
Figure 2. 5: SEM images on Zn-coated steel after annealing at different temperatures and times [15].	9
Figure 2. 6: SEM micrographs of a GI coating annealed at 900°C for 4min, a) microstructure, b) Zn distribution, c) Al distribution by WDS [1].	10
Figure 2. 7: Propagation rate of the LME induced crack as a function of strain rate [19].	13
Figure 2. 8: Schematic representation of crack in a stressed metal exposed to liquid metal environment X [40].	15
Figure 2. 9: Schematic diagram of the enhanced dislocation emission model for liquid metal environments [34].	17
Figure 2. 10: Schematic diagram of embrittling atoms transport to crack tips by a surface diffusion process during SME [22].	18
Figure 2. 11: Scanning electron micrograph of the fracture surface produced by solid-cadmium-induced embrittlement (at 295°C) of a mill-annealed Ti- 6 wt.%Al- 4 wt.%V alloy, showing fluted	

intercrystalline facets (F) and cleavage-like area (C). Islands of cadmium film are also evident [22].

19

Figure 2. 12: (a) SEM micrograph and corresponding (b) FE-EPMA Zn elemental distribution map of a Zn-coated 22MnB5 PHS [4].

20

Figure 2. 13: Schematic diagram of liquid metal embrittlement process in Zn-coated PHS [4].

21

Figure 2. 14: TEM cross-section (left) of zinc diffusion in a Zn coated 22MnB5 PHS. (Right) EDS linescan analysis across the grains [4].

22

Figure 2. 15: 1D finite difference model of Zn-coated 22MnB5 at 900°C [46].

23

Figure 2. 16: Schematic of the SME mechanism of micro-cracking in Zn-coated press hardened boron steels [46].

25

Figure 2. 17: SEI micrograph of the  $\alpha$ -Fe(Zn) grain boundary and the corresponding Zn EDS analysis (map and linescan) [46].

26

Figure 2. 18: Zn-coating effect on the mechanical properties of a PH 22MnB5 steel at 850°C [2].

27

Figure 2. 19: Stress-strain curves for samples deformed at different conditions [1].

27

Figure 2. 20: Zinc distribution obtained by WDS for a GI 22MnB5 sample annealed at (a) 850°C for 4min and subsequently 40% strained at 700°C and (b) at 850°C for 20min and 40% strained [1].

29

Figure 2. 21: High-temperature stress-strain curves for a Zn-1.6% Al-1.6% Mg coated PH steel, influence of (a) initial zinc coating weight (38 g/m<sup>2</sup> vs. 63 g/m<sup>2</sup> vs. 105 g/m<sup>2</sup>), (b) annealing time (2min vs. 5min), (c) higher Al content (3.2 wt.%) in the coating composition for different zinc

coating weights – Note that in the case of higher Al content, higher loading of Zn didn't exhibit LME [2]. 30

Figure 4. 1: Schematic of the tube furnace set up for the coating microstructural and diffusion study [51]. 36

Figure 4. 2: Typical time-temperature profile for microstructural evolution samples. 37

Figure 4. 3: Experimental apparatus for DHPF including a conventional box furnace and a conventional 250kN MTS tensile frame [51]. 38

Figure 4. 4: Time-temperature profile for a conventional box furnace. 39

Figure 4. 5: Dimensions of the U-shaped die used in 250kN MTS tensile frame for DHPF. 40

Figure 4. 6: 3D DIC strain profiles for tension (major strain) and compression (minor strain) on a GI70 coated 22MnB5 substrate after U-shaped die DHPF. 43

Figure 5. 1: SE image of the as-received GI70 22MnB5 substrate. 52

Figure 5. 2: Optical image of GI70 22MnB5 substrate annealed at 900°C for 780s and compressed air quenched. 52

Figure 5. 3: BSE image of an AR GI70 coated 22MnB5 substrate in cross-sectional view. 53

Figure 5. 4: EDS a) Zn distribution, b) Fe distribution, and c) Al distribution map of an AR GI70 22MnB5 substrate in cross-sectional view. 53

Figure 5. 5: BEI-SEM micrographs GI70 samples in the as-received (AR) condition, and annealed at 900°C for 30 s, 120s, 300s, 420s, and 780s and compressed air gas quenched. 55

Figure 5. 6: BEI-SEM micrographs GI70 samples in the as-received (AR) condition, and annealed at 900°C for 30 s, 180s, 240s, 300s, and 780s and die-quenched. 57

Figure 5. 7: a) Squared coating thickness as a function of annealing time (240s to 780s), and b) zinc concentration (at%) as a function of the distance of the coating-substrate interface to top surface, GI70 samples annealed at 900°C for all the annealing times, as-quenched in compressed air condition. 58

Figure 5. 8: Phase ratio of a) compressed gas quenched b) water-cooled planar die-quenched GI70 samples annealed at 900°C for all the annealing times. 59

Figure 5. 9: Summative plot of  $\sigma$ (UTS) as a function of all varying annealing times at 900°C for the planar and U-shaped die-quenched Zn-coated 22MnB5 steel samples. 60

Figure 5. 10: BEI-SEM micrographs of (a,c) as-quenched and (b,d) after tensile testing GI70 samples annealed at 900°C for 30 s and 780s, and subsequently quenched by water-cooled planar dies. 63

Figure 5. 11: Cross-sectional view on the fracture surfaces of a die-quenched Zn-coated sample annealed at 900°C for 180s. 63

Figure 5. 12: EBSD phase maps of as-quenched after tensile testing samples, annealed at 900°C for a) 30 s and b) 780s. 65

Figure 5. 13: a,b) EBSD phase maps, c,d) EBSD Euler maps after tensile testing for samples annealed at 900°C for 30 s and 780s - Noted that micro-cracks on the samples are highlighted with a red circle on the EBSD phase maps. 66

Figure 5. 14: APRGE austenite grain reconstruction on the die-quenched Zn-coated sample annealed at 900°C for 780s. 67

Figure 5. 15: STEM ADF images and EELS maps of the GB in the coating and substrate from a 30AQ sample.	69
Figure 5. 16: STEM ADF images and EELS maps of the GB in the coating and substrate from a 780AQ sample.	70
Figure 5. 17: Zinc distribution profile to a) the coating GB and b) the PAGB Zn EELS map Zn EELS map for a 780AQ sample.	71
Figure 5. 18: STEM ADF images and EELS maps of 30TS, a) along the crack, and b) the micro-crack tip.	73
Figure 5. 19: STEM ADF images and EELS maps of 780TS, a) along the crack, and b) the micro-crack tip.	74
Figure 5. 20: Schematic cross-sectional view of Zn-coated PHS U-shaped die-quenched [5].	76
Figure 5. 21: BSE images and their corresponding EDS Zn elemental distribution of the U-shaped Zn-coated PHS sample annealed at 900°C for 30 s.	79
Figure 5. 22: BSE images and their corresponding EDS Zn elemental distribution of the U-shaped Zn-coated PHS sample annealed at 900°C for 780s.	80
Figure 5. 23: EBSD phase maps of area 1 of the U-shaped samples annealed at 900°C for (a) 30 s and (b) 780s.	82
Figure 5. 24: STEM ADF images and EELS maps of the GB in the coating and PAGB in the substrate, 30UR1 sample.	84
Figure 5. 25: STEM ADF images and EELS maps of the GB in the coating and PAGB in the substrate, 780UR1 sample.	85

Figure 5. 26: Cross-sectional view SAM-AES map images of a GI70 sample annealed at 900°C for 30 s. 86

Figure 5. 27: STEM ADF images and EELS maps of 30UR4, a) along the crack, and b) the micro-crack tip. 87

Figure 5. 28: STEM ADF images and EELS maps of 780UR4, a) along the crack, and b) the micro-crack tip. 88

Figure 6. 1: A schematic of the microstructural evolution in GI70 22MnB5 DHPF samples as a function of temperature and holding time at 900°C. 90

Figure 6. 2: A schematic of the proposed micro-cracking mechanism in Zn-coated DHPF steels annealed at 900°C: a) before the application of tension; solid-state diffusion of zinc along the grain boundaries results in the formation of a Zn-enriched  $\alpha$ -Fe(Zn) layer in the  $\alpha$ -Fe(Zn) GBs and in the PAGBs - Note that different shades of blue in the GBs indicate that Zn enrichment was slightly declining from the coating to the Zn-martensite layer and finally to the fully lath martensitic substrate. b) after tensile testing; micro-cracking showed three stages of crack initiation, crack propagation, and crack blunting - Note that the cracking process initiated along the Zn-enriched  $\alpha$ -Fe(Zn) GBs and propagated along the weaker  $\alpha$ -Fe(Zn) layer in the PAGBs. 95

## Table of Tables

Table 4. 1. Chemical composition of the as-received 22MnB5 steel grade (wt.%).	35
Table 4. 2. Experimental annealing and cooling conditions.	38
Table 4. 3. Metallographic preparation for SEM-EBSD.	46
Table 4. 4. EBSD phases, and their related crystal structure and zinc content.	48
Table 4. 5. Details on the samples examined for zinc distribution using SEM-EBSD and STEM-EELS techniques.	49
Table 5. 1. Details on the examined samples for zinc distribution using EM techniques.	61
Table 5. 2. Detailed conditions of each region on U-shaped sample after press forming process [5].	76
Table 5. 3. Details on the examined U-shaped samples for zinc distribution using EM techniques.	81

## List of Abbreviations

PHS	Press Hardened Steels
DHPF	Direct Hot Press Formed
LME	Liquid Metal Embrittlement

SME	<b>Solid Metal Embrittlement</b>
GB	<b>Grain Boundary</b>
PAGB	<b>Prior Austenite Grain Boundary</b>
GI	<b>Galvanized</b>
GA	<b>Galvannealed</b>
SEM	<b>Scanning Electron Microscopy</b>
SE	<b>Secondary Electron</b>
BSE	<b>Backscattered Electron</b>
WDS	<b>Wavelength Dispersive X-ray Spectroscopy</b>
EPMA	<b>Electron Probe Micro Analyzer</b>
UTS	<b>Ultra High Strength</b>
AR	<b>As-received</b>
ICP-OES	<b>Inductively Coupled Plasma - Optical Emission Spectroscopy</b>
TD	<b>Transverse Direction</b>
RD	<b>Rolling Direction</b>
ADF	<b>Annular Dark Field</b>

AQ	<b>As-quenched</b>
DIC	<b>Digital Image Correlation</b>
XRD	<b>X-ray Diffraction</b>
OM	<b>Optical Microscope</b>
OPS	<b>Active Oxide Polishing Suspension, Colloidal Silica</b>
DI	<b>Deionized water</b>
CSP	<b>Cross-Sectional Polisher</b>
SEM	<b>Scanning Electron Microscopy</b>
EBSD	<b>Electron Backscattered Diffraction</b>
EDS	<b>Energy Dispersive X-ray Spectroscopy</b>
EELS	<b>Electron Energy Loss Spectroscopy</b>
FE	<b>Field Emission</b>
FEG	<b>Field Emission Gun</b>
STEM	<b>Scanning Transmission Electron Microscopy</b>
TEM	<b>Transmission Electron Microscopy</b>
AES	<b>Auger Electron Spectroscopy</b>
UHSS	<b>Ultra-High Strength Steel</b>

## 1. Introduction

The automotive industry has expressed a high demand for ultra-high strength steels (UHSS) due to increasing passenger safety requirements and lower vehicle weights for increased fuel efficiency. In order to acquire precise dimensional accuracy for automotive parts, such as, side impact beams, bumpers, A- and B-pillars, and roof rails, press hardening is the most commonly used method [1, 2] for steel fabrication. Therefore, press hardened steels (PHS) are widely used for providing these lightweight, high strength, anti-intrusion components [1, 3].

Press hardened parts are often exposed to corrosive environments as well as oxidation during the process. In order to provide cathodic protection against these environments, in addition to preventing decarburization of the steel sheet during austenitization, Zn-based metallic coatings are employed due to their effectiveness and reasonable cost.

Micro-crack formation after thermomechanical processing is an issue that limits full deployment of Zn-coated PHS. After the application of tension, micro-cracks can propagate into the PHS substrate and negatively affect the mechanical properties of the resulting components. Several mechanisms for micro-crack formation have been proposed, including the currently popular theory of liquid metal embrittlement (LME). Some groups have also reported potential methods to mitigate micro-cracking into the PHS substrate [2, 4-6]. However, none of the proposed formation mechanisms can explain all observed cases of micro-cracking, as there are a wide variety of processing conditions under which these occur.

In the present project, the origin of microcracking in die-quenched Zn-coated 22MnB5 steel was determined by tracking zinc diffusion through the coating and into the substrate, focusing on the role of grain boundaries (GBs) within the  $\alpha$ -Fe(Zn) coating and the prior austenite grain boundaries (PAGBs) in the underlying substrate. It is proposed that due to the presence of a Zn-enriched layer as a resultant of solid-state zinc diffusion along the PAGBs of the substrate, these areas are susceptible to micro-crack propagation after the application of tension.

## **2. Literature Review**

### **2.1 Continuous Galvanizing Line**

Figure 2.1 shows a Sendzimir continuous Zn-coating line which is commonly used to galvanize steels. Prior to a typical continuous hot-dip galvanizing process, cleaning is required in order to remove organic contaminants and surface oxides that are introduced during rolling of the feedstock steel. This process usually takes place by immersing the strip of substrate material in an aqueous alkali solution, typically a 5-10% NaOH solution, to degrease and clean the steel substrate. After the cleaning process, the sheet is heated to above the recrystallization temperature; the peak annealing temperature is determined by the steel composition and the desired final microstructure. Subsequently, the substrate material is cooled to 460°C so that it is in thermal equilibrium with the bath, which is normally maintained at 440-460°C [7, 8].

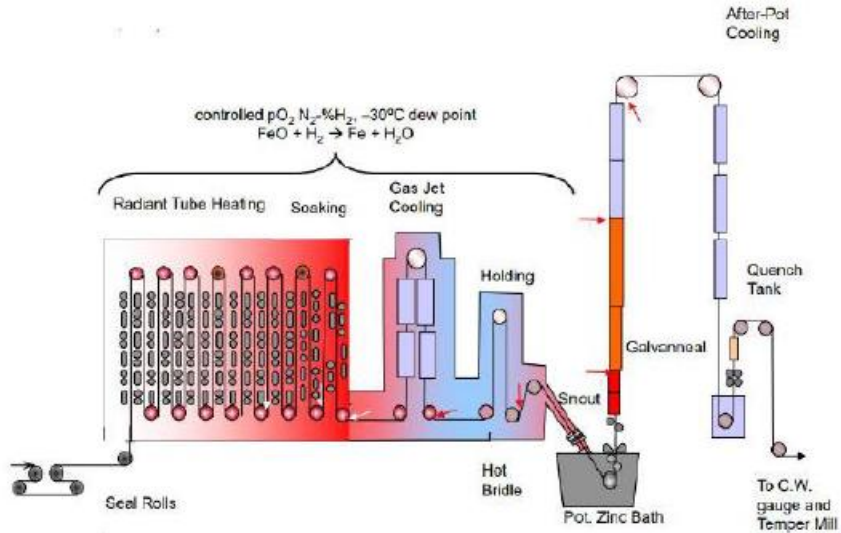


Figure 2. 1: Sendzimir continuous galvanizing line [9].

The steel substrate is then fully immersed in an almost pure molten zinc (minimum of 98%) bath. As soon as the steel substrate enters to the molten bath, Fe-Zn intermetallic phases start to form while the molten zinc and the steel react with each other. One of the important constituents of the bath is dissolved Al, which increases the coating performance by reducing the rate of zinc oxidation by formation of an  $Fe_2Al_{5-x}Zn_x$  inhibition layer during the hot dip process [7]. This inhibition layer also reduces the brittleness of the coating, improving its formability. The most commonly used industrial hot-dip zinc coatings have Al range of 0.15-0.2 wt.% [10].

Various parameters can affect the microstructure and properties of the developed hot-dip zinc coatings such as bath temperature, dipping time, withdrawal speed, bath composition [7, 11]. A typical dipping process takes 4 to 6 seconds with a line speed of around 175 m/min [7]. After dipping, the steel sheet is removed from the bath and the coating thickness is controlled using air knives, which skim off excess Zn. Subsequently, the coated sheet is either cooled by forced air

in order to create galvanized coatings (GI) or subjected to an in-line heat treatment in order to produce galvanized coatings (GA) [7, 8].

## **2.2 Direct Hot Press Forming (DHPF)**

To design and produce a car body part, hot press forming (HPF) is commonly employed. Direct and indirect hot press forming are two main methods as outlined in Figure 2.2 [1]. In the case of the direct process, the initially ferritic and pearlitic steel substrate is heated above the austenitization temperature, in the range of 900-950°C, for 3-10min in a conventional furnace, resulting in a fully austenitic microstructure. Steel sheets are then press formed and subsequently die-quenched with a cooling rate in excess of  $25^{\circ}\text{C}\text{s}^{-1}$ , resulting in a fully martensitic substrate with a total strength of over 1500MPa [1].

For indirect forming, an initial pre-press forming step is added prior to the direct hot press forming process. Although the indirect method can facilitate the production of automotive parts with more complex shapes, it is a more expensive method with increased springback issues for industrial production lines. Therefore, the direct method is more commonly used in the automotive industry [1, 12].

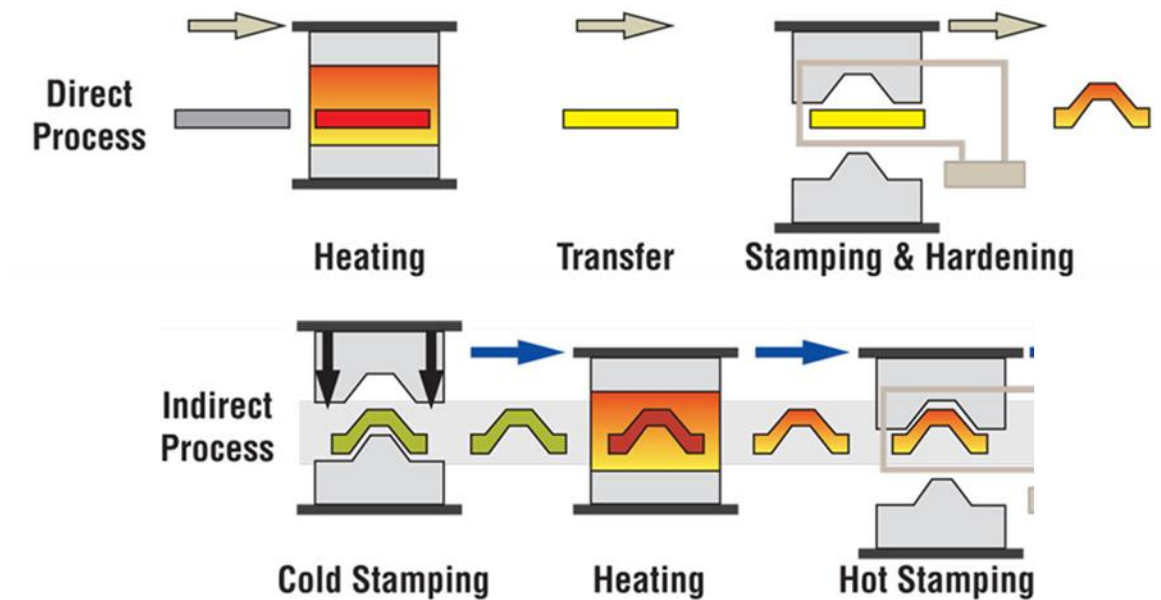


Figure 2. 2: Schematic of the direct and indirect hot stamping process [2].

To manufacture lightweight vehicle parts while maintaining passenger safety by introducing high strength to body parts, press hardened boron alloyed ( $\sim 0.002$  wt.% B) steel sheet is typically used. The most commonly used steel grade for this application is 22MnB5 [1]. In low carbon steels ( $\sim 0.22$  wt.% C), Mn and B additions improve the hardenability and result in an almost fully martensitic microstructure [1, 6, 13]. The presence of Mn retards austenite decomposition and small additions of B retard ferrite nucleation at austenite boundaries.

### 2.3 Fe-Zn Phase Transformations

When the steel sheet is introduced to the galvanizing bath, zinc and iron chemically react to form Fe-Zn intermetallic phases. The Fe-Zn phase diagram is outlined in Figure 2.3 [1]. Horstmann proposed the formation of the following layers (starting with the innermost layer in the coating) while dipping the steel sheet in a 450-490°C zinc bath: initially a zinc saturated  $\alpha$ -iron ( $\alpha$ -Fe(Zn)),

followed by a gamma ( $\Gamma$ ) phase, then a gamma<sub>1</sub> ( $\Gamma_1$ ) phase, fourth a delta ( $\delta$ ) phase, fifth a zeta ( $\zeta$ ) phase and finally an eta ( $\eta$ ) phase. At the Fe-Zn interface, first the zeta ( $\zeta$ ) phase nucleated, then the delta ( $\delta$ ) phase layer and, after some incubation time, a thin layer of gamma ( $\Gamma + \Gamma_1$ ) phases formed [14]. Figure 2.4 schematically shows the Fe-Zn phase layer evolution during immersion of steel in a zinc bath. By increasing incubation time from  $t_1$  to  $t_4$ , when  $t_0$  corresponded to zero time, immediately after zeta ( $\zeta$ ) nucleation ( $t_2 \sim 5$  s after immersion), delta ( $\delta$ ) formed at the coating-substrate interface. After  $t_3$  ( $\sim 30$  s) immersion, the gamma phase layer formed. Depending on the level of Fe supersaturation by Zn, two zeta phases could form by increasing the incubation time ( $t_4 > 30$  s) [8].

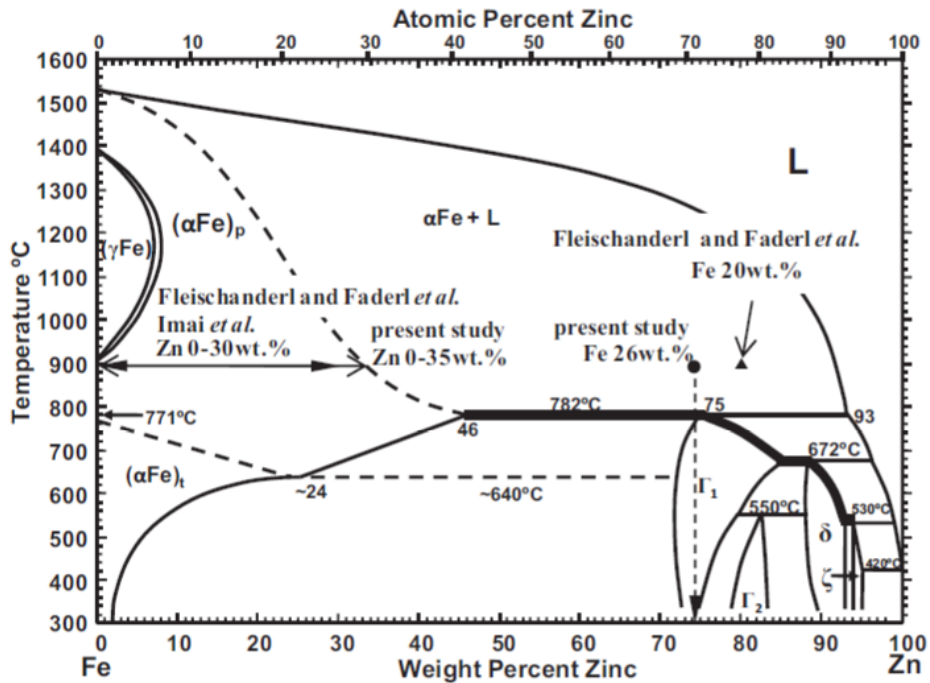


Figure 2. 3: Figure 2.3. Fe–Zn binary phase diagram [1].

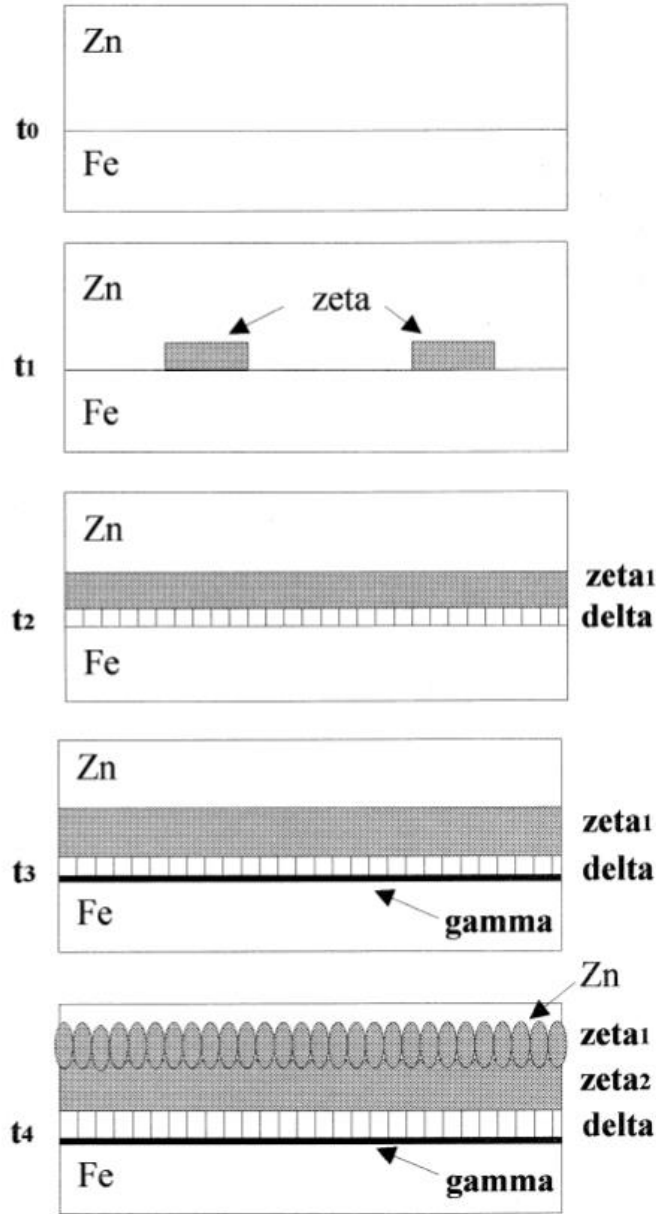


Figure 2. 4: A schematic diagram of Fe-Zn phase layer formation in a 0.00 wt.% Al-Zn galvanizing [8].

Temperature is the other important processing variable for diffusion couple driven growth; time spent at higher temperatures result in further iron and zinc interactions and consequently the formation of different Fe-Zn intermetallic phases. Figure 2.5 depicts how these phase

transformations occur gradually as the annealing temperature increases from 400°C to 900°C [15]. At 400°C, the surface coating contained an almost pure Zn eta ( $\eta$ ) phase layer. By increasing the temperature to between 450°C and 500°C, columnar zeta ( $\zeta$ ) phase particles started nucleating at the Fe-Zn interface [7]. At 550°C, the transformation to delta ( $\delta$ ) phase with an iron content of 11 wt.% was completed [16]. At 600°C, the  $\Gamma_1$  phase began to form out of the delta ( $\delta$ ) phase at the coating-steel interface, and by 700°C, the  $\Gamma$  phase transformation was complete. At 750°C and above, the transformation of  $\Gamma$  phase to zinc saturated solid  $\alpha$ -Fe phase (zinc ferrite) occurred. Further annealing to a typical press hardening processing temperature of around 900°C resulted in the growth of more zinc ferrite in the coating. According to the Fe-Zn phase diagram, 782°C is the peritectic point where conversion of the  $\Gamma$  phase to a mixture of liquid zinc and zinc ferrite phase occurs. However, some of Fe-Zn phases were still above their thermodynamically stable regions. For instance, Figure 2.5 clearly shows remaining traces of  $\Gamma$  phase at 900°C which was caused by fast heating rates [15].

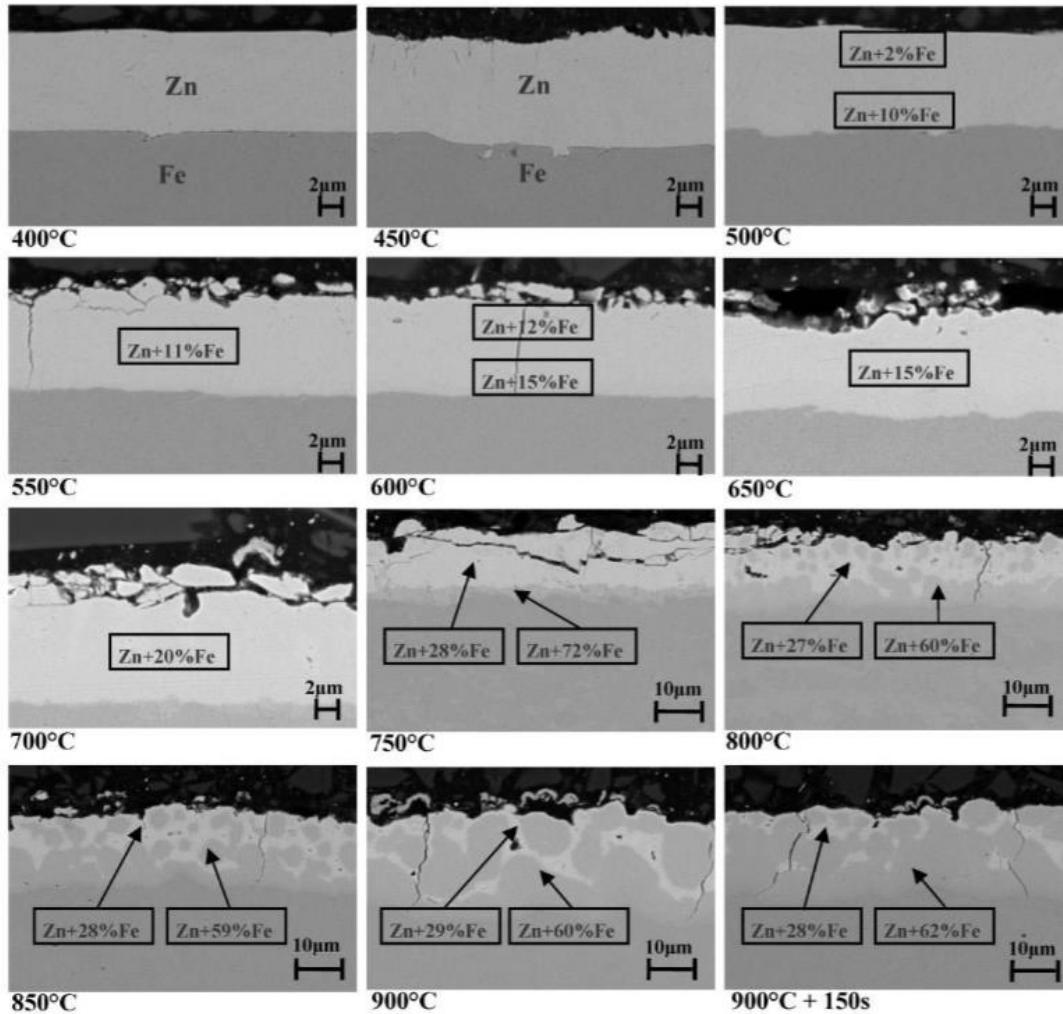


Figure 2. 5: Figure 2.5. SEM images on Zn-coated steel after annealing at different temperatures and times [15].

## 2.4 High Temperature Fe-Zn Phase Evolution

During the thermomechanical processing of a typical direct hot press forming (DHPF) workflow, time and temperature are both increasing continuously before cooling. These two main parameters act as a driving force for the inward diffusion of zinc into the austenitic substrate.

During the DHPF process, steel sheets are heated up to the austenitization temperature of 900°C which leads to iron and zinc chemically reacting. By holding the material at 900°C, the coating layer grows as a result of diffusion driven growth. Figure 2.6 shows SEM micrographs of a typical microstructure of a GI coating after the DHPF process. The initial coating thickness was 17  $\mu\text{m}$ ; however, after DHPF it increased to 30  $\mu\text{m}$ . As shown in Figure 2.6 b, it is observed that after a few minutes of annealing the coating normally consisted of 1) thin layer(s) of oxide ( $\text{ZnO-Al}_2\text{O}_3$ ) on the top surface, 2)  $\Gamma$  intermetallic phase, 3) zinc-ferrite phase ( $\alpha\text{-Fe(Zn)}$ ) close to the coating-substrate interface. Likewise, zinc oxide ( $\text{ZnO}$ ) was one of the phases that developed at the outer surface during the heat treatment process. The presence of an oxide layer is beneficial because it suppresses further zinc evaporation. According to several studies, longer annealing times result in inward diffusion of zinc into the substrate leaving behind a thicker coating with lowered zinc concentration [1].

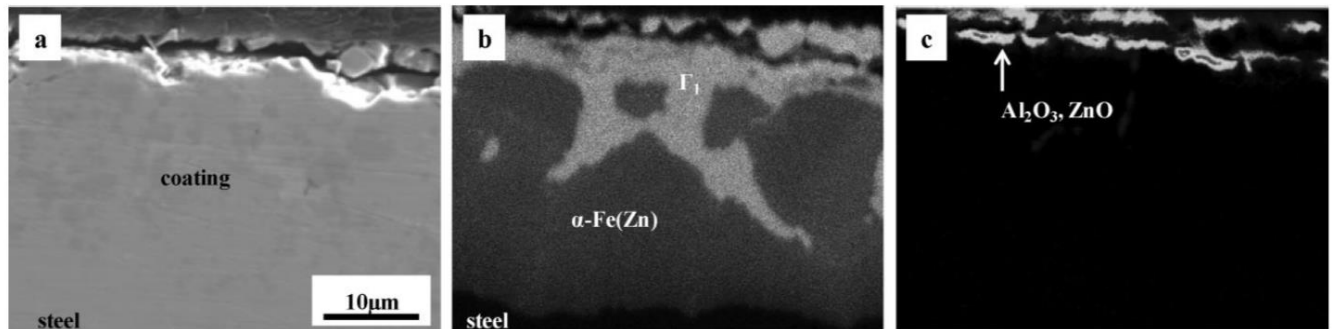


Figure 2. 6: SEM micrographs of a GI coating annealed at 900°C for 4min, a) microstructure, b) Zn distribution, c) Al distribution by WDS [1].

## **2.5 Micro-Cracking Mechanisms**

Generally, fatigue, hydrogen embrittlement (HE), and stress corrosion cracking are among the commonly known failure processes for a substrate material [17]. Liquid metal embrittlement (LME) and solid metal embrittlement (SME) have been reported less, specifically in zinc-coated steel systems [6, 18, 19]. LME and SME mostly occur when the material is in contact with an embrittling system. LME occurs when a material is in contact with a liquid embrittler whereas SME takes place when the embrittler is solid. Accordingly, experimental variables, like temperature, applied load and the initial coating composition, play an important role in the occurrence and extent of LME or SME [20, 21]. Generally, a material's resistance to crack formation and micro-crack growth is higher in an inert (air) environment than liquid or solid metal environments [22]. Furthermore, cracking rates are controlled by the transport of the embrittler atoms to the micro-crack tips, by capillary flow in LME cases [23], and by the diffusion of atoms in SME cases, [19]. Therefore, the velocity of cracking in LME is faster than in SME cases [22].

### **2.5.1 Liquid Metal Embrittlement (LME)**

LME is caused by the loss of ductility of substrate material under a critical load due to rapid percolation of secondary liquid material into the substrate [5, 24]. During LME, the liquid metal atoms penetrate through defects, especially along grain boundaries. The resulting wetted pathways, specifically along grain boundaries of the substrate material, create potential sites for crack initiation and propagation (due to the lowered fracture stress at these boundaries) during the application of a critical stress. There are two necessary, but not sufficient, prerequisites in order to have LME occur in a system [2]. The first condition is applying a critical stress to produce

plastic deformation [2], although there have been some exceptional cases in which LME was observed below the bulk yield stress [25]. The second prerequisite is the direct contact of a liquid phase with the stressed solid such that penetration of liquid metal either along the grain boundaries or pre-existing cracks can occur. Hancock and Ives [26] have shown that oxide formation at the liquid-solid interface could impede embrittlement since it delayed liquid and solid direct contact. When stress was applied, oxide films ruptured and resulted in solid-liquid contact. LME barely depends on the liquid-solid contact time unless an applied stress level exceeds the critical stress value which can result in fast failures.

Among all the mechanical characteristics of a material, ultimate tensile strength and ductility are two features that are consequently affected by LME. The most common mode of fracture for metals failed to LME is intergranular fracture; however, in some cases, transgranular fracture has been observed [27, 28]. The propagation rate of the LME induced cracks, along either grain boundaries or grains, depending upon strain rate, varies linearly (Figure 2.7).

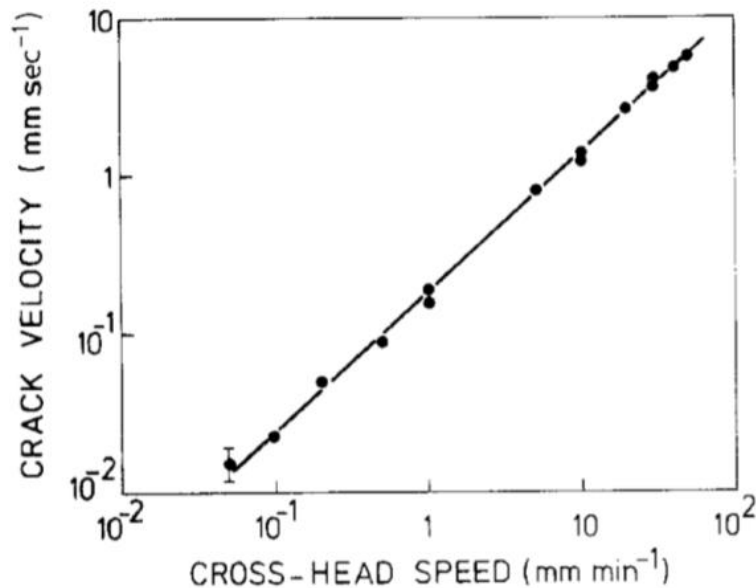


Figure 2. 7: Propagation rate of the LME induced crack as a function of strain rate [19].

The usual minimum temperature for LME is the melting point of the embrittler, since atoms are more mobile in the liquid phase. This is the case with austenitic steels and zinc coatings, for example, where LME occurs at temperature ranges above 750°C. However, in some cases, LME has been observed to happen below the melting point (details are explained in section 2.5.3) [29].

Therefore, LME occurrence involves a combination of solid-liquid material, metallurgical condition, and exposure conditions [30]. The necessity of high temperatures in some industrial manufacturing conditions, such as the hot press forming process, escalates LME failures. Pre-straining by cold working [31], grain boundary chemistry modification by addition of other elements [32] and, hardness and deformation behaviour of the solid [33] are amongst the reported examples influencing LME [30].

## 2.5.2 Liquid Metal Embrittlement (LME) Mechanisms

Several LME mechanisms have been proposed in the literature. A few of these mechanisms are discussed in more detail in the following paragraphs.

**Reduction in surface energy model:** liquid adsorption by the solid material, particularly in the crack region, results in the reduction of the required applied stress for fracture [34]. According to this mechanism, Griffith [35] showed that the required stress for the fracture relates to the specific surface energy in an elastic material by the following equation:

$$\sigma_a = \left( \frac{2E\gamma_e}{\pi a} \right)^{\frac{1}{2}} \quad (2.1)$$

Where  $\sigma_a$  is the applied stress,  $E$  is the Young's modulus,  $\gamma_e$  is the special surface energy and,  $a$  is the crack length [35]. The mentioned equation was modified later by adding a term representing not only elastic energy but also plastic energy which can affect the total fracture energy in the surface energy model [36]:

$$\sigma_a = \left( \frac{2E\gamma_f}{\pi a} \right)^{1/2} \quad (2.2)$$

Where  $\gamma_f = A\gamma_e$ , and  $A$  is a constant. Therefore, any changes in  $\gamma_e$  will be considered in the total fracture energy.

Eborall and Gregory [37] observed a reduction in fracture stress due to the reduction in surface energy while liquid metal was present at the crack tip. If LME is considered as a special type of brittle fracture, then many experimental cases can fall into the category of the surface energy model like an increase in brittle to ductile transition temperature due to the presence of a liquid metal. Although the model explains LME fracture occurrence, it does not consider atomistic arguments for the occurrence of embrittlement.

**Adsorption-induced reduction in cohesion model:** this model is an extended form of the surface energy model that emphasizes the decohesion of interatomic bonds at the crack tip by the presence of liquid metal atoms [38, 39], as shown in Figure 2.8. Thus, the crack can propagate along the cleavage plane where the decohesion of the interatomic bonds had occurred. Likewise, the crack can blunt due to the gliding of dislocations along the slip plane. The required tensile stress for the propagation of a sharp crack is stated in the following equation [38, 39]:

$$\sigma_p = \left( \frac{E\gamma_e}{4a} \right)^{1/2} \quad (2.3)$$

However, crack blunting is more probable in practice, and the required stress for that is [40]:

$$\sigma_{p(blunted)} = \left( \frac{E\gamma_f}{4a} \right)^{1/2} \quad (2.4)$$

Where  $\gamma_f = \chi\gamma_e$ ,  $\chi$  is the dimensionless constant related to plastic relaxation at the crack tip.

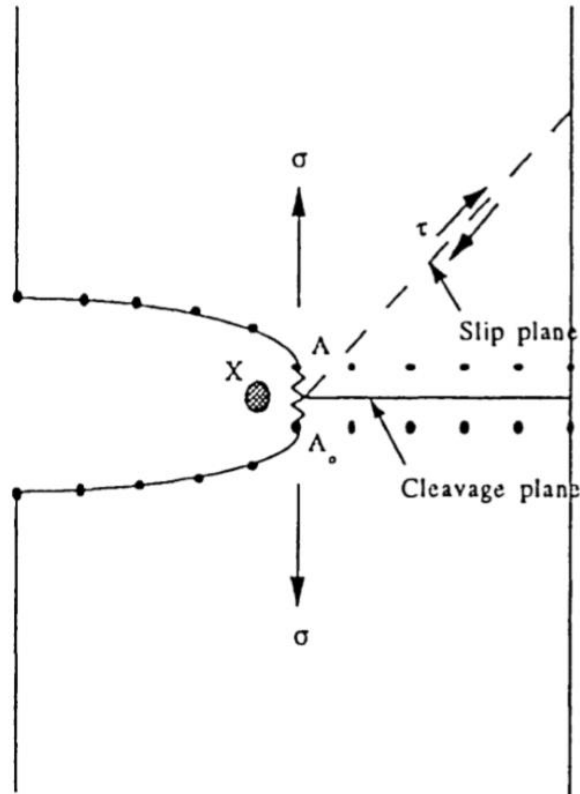


Figure 2. 8: Schematic representation of crack in a stressed metal exposed to liquid metal environment X [40].

Kamdar studied the steel-lead system using notched samples where the stresses at the notch were pure shear. He found that the crack initiation occurred in the plane of the notch (plane of maximum shear stress) and the crack growth occurred at 45° to the plane of the notch (the plane

of maximum tensile stress). This observation confirmed that LME occurred along the maximum tensile stress planes as predicted by the adsorption-induced reduction in cohesion model [34].

In some cases, the embrittler atoms may bond with the atoms at the crack tip and form a compound. Alternatively, the embrittler atoms can diffuse into the solid metal and form a solid solution. In both cases, crack propagation will be blocked due to the formation of a new compound at the crack tip. Slavin and co-workers [41] observed the occurrence of LME in metallic glasses under compression which showed a limitation to the adsorption-induced reduction in cohesion model.

**Enhanced dislocation emission model:** this model elucidates the reduction in the shear strength of the atomic bonds at the crack tip, unlike the adsorption-induced mechanism which focuses on the tensile strength of the interatomic bonds [42, 43]. According to the enhanced dislocation emission model, dislocation nucleation occurs at the crack tip and leads to failure because of localised plasticity in the region ahead of the crack. The nucleated dislocations are on the slip planes which facilitates crack growth subsequently. Therefore, fractography shows fracture surfaces with small and shallow dimples. The schematic diagram of the enhanced dislocation emission model is shown in Figure 2.9. Fractography also proved the presence of small and shallow dimples on LME fractured samples [41] such as precipitate hardened aluminum alloys (Al- 6Zn- 3Mg) [19]. Kapp showed that in torsion experiments on notched brass samples, crack propagation occurred along the plane of maximum tensile stress, which was inconsistent with this model [34]. It is worth mentioning that the process of sample preparation for the fractography may introduce artefacts into the fractured surface which is usually covered with liquid and affects the final observation [34].

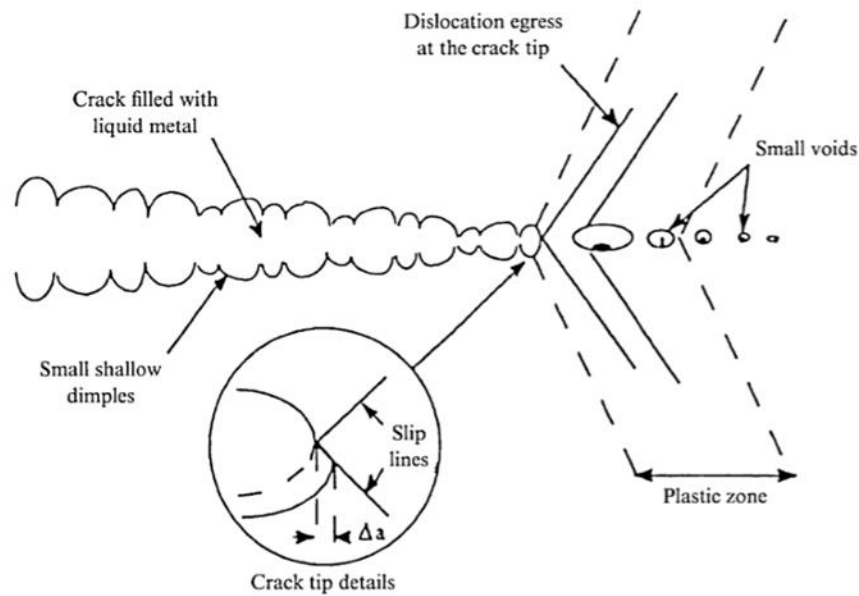


Figure 2. 9: Schematic diagram of the enhanced dislocation emission model for liquid metal environments [34].

**Embrittlement associated with diffusion:** another theory for LME occurrence is the diffusion of liquid metal atoms along the grain boundaries of the solid. For example, before applying any stress, liquid gallium penetrated along the grain boundaries of aluminum and zinc polycrystals. This led to the formation of a thin liquid film along the grain boundaries of the solid. Above a critical stress level, transgranular fracture took place on aluminium and zinc polycrystals [24, 44].

### 2.5.3 Solid Metal Embrittlement (SME)

SME is similar to LME, however in SME, embrittlement mostly occurs below the melting point of the embrittler ( $T_m$ ) at temperatures as low as about  $0.3T/T_m$  [22, 29]. Some of the proposed mechanisms for LME may be applied to SME. One of the suggested controlling mechanisms for SME by Lynn et al. was crack extension by multilayer surface self-diffusion of the embrittler through the substrate metal or along its grain boundaries [29]. In another study Lynch reported

that the cracking rate was controlled by the movement of embrittling atoms to crack tips through a surface diffusion process [22] which is shown schematically in Figure 2.10. Therefore, based on  $x$  (crack length) vs.  $t$  (time) curves for the aluminum alloy 7075 cracked in indium [22], the surface diffusion coefficient ( $D_s$ ) for this purpose was calculated for various temperatures;

$$D_s = \frac{x^2}{2t} \quad (2.5)$$

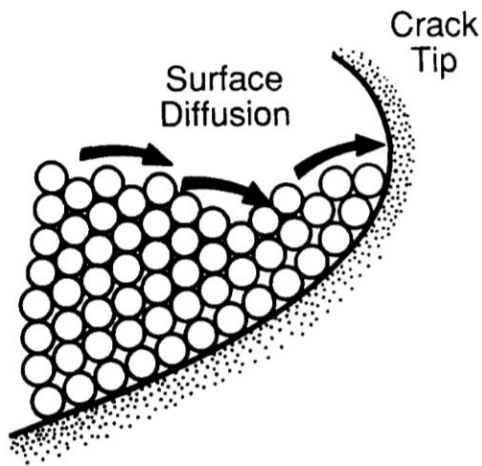


Figure 2. 10: Schematic diagram of embrittling atoms transport to crack tips by a surface diffusion process during SME [22].

Surface oxides can lower the embrittler surface diffusion to the crack tip. Additionally, the embrittler itself can sometimes inhibit crack propagation by sealing the crack tip [22]. Different variables, such as temperature, substrate-embrittler degree of contact, and micro-crack environment (i.e. whether air is eliminated from the cracks or not), impact micro-crack formation.

Fractography of SME induced cracks [22, 45] exhibited intercrystalline facets as well as shallow dimples on the fracture surface. Figure 2.11 shows a fracture surface created by solid-cadmium-induced embrittlement of a mill-annealed Ti- 6 wt.% Al- 4 wt.% V alloy. These observations can explain the adsorption-induced SME mechanism in the materials. Adsorption weakens interatomic bonds and enhances dislocations nucleation at the crack tip. During crack growth, the coalescence of voids leads to the formation of shallow dimples on fracture surfaces.

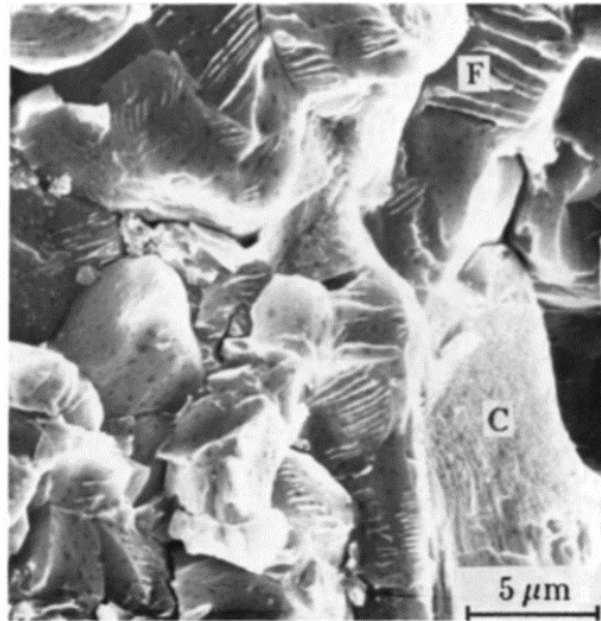


Figure 2. 11: Scanning electron micrograph of the fracture surface produced by solid-cadmium-induced embrittlement (at 295°C) of a mill-annealed Ti- 6 wt.%Al- 4 wt.%V alloy, showing fluted intercrystalline facets (F) and cleavage-like area (C). Islands of cadmium film are also evident

[22].

## 2.6 LME and SME in Zn-Coated Press Hardened Steel

Multiple possible mechanisms of Zn-coated PHS micro-cracking have been proposed [22, 29, 30, 34]. Any of the mechanisms specified previously can be employed to explain embrittlement in Zn-coated PHS. Depending on the experimental conditions (i.e. in-service temperature, annealing time, initial coating thickness, etc.), micro-cracking may occur due to one of the possible mechanisms. LME has been referred to as the most common failure mechanism for PHS micro-cracking. Figure 2.12 (a) shows a typical morphology of a LME micro-crack enriched with  $\Gamma\text{-Fe}_3\text{Zn}_{10}$  in a Zn-coated PHS. Figure 2.12 (b) shows Zn elemental distribution along the LME crack and the micro-crack.

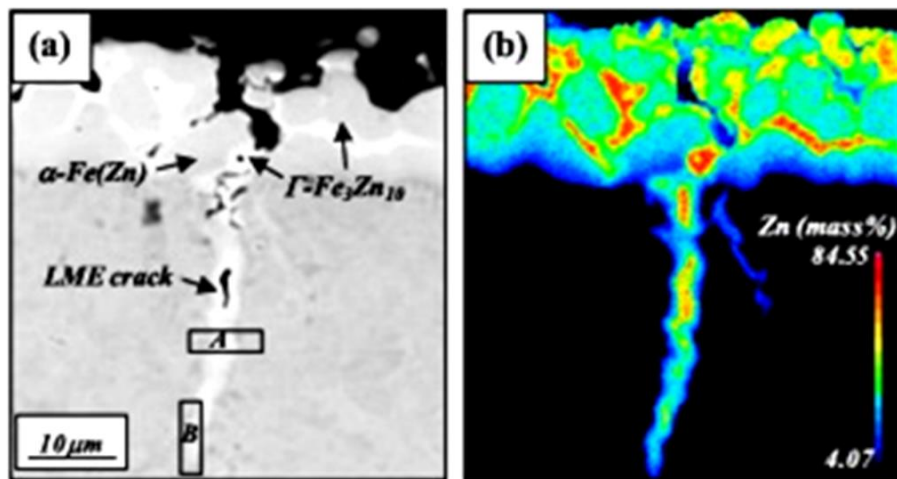


Figure 2. 12: (a) SEM micrograph and corresponding (b) FE-EPMA Zn elemental distribution map of a Zn-coated 22MnB5 PHS [4].

Figure 2.13 schematically demonstrates the LME process in the Zn-coated PHS. It can be observed that by holding the Zn-coated steel at 900°C for a short time (i.e. 30 s), the coating consisted of  $\alpha\text{-Fe(Zn)}$  and solidified liquid zinc or  $\Gamma\text{-Fe}_3\text{Zn}_{10}$ . During holding the sample at 900°C, the liquid zinc

started to diffuse into the coating grain boundaries or initial cracks and subsequently penetrated along the prior austenite grain boundaries (PAGBs) of the substrate. Longer holding times led to further diffusion of liquid zinc into the PAGBs. After hot press forming, the PAGBs enriched with liquid zinc transformed into  $\Gamma$ -Fe<sub>3</sub>Zn<sub>10</sub> phase, which acted as potential sites for crack initiation and micro-crack propagation [4]. Cho et al. also suggested that, as a result of grain boundary diffusion along the PAGBs, a thin layer of  $\alpha$ -Fe(Zn) can form in between  $\Gamma$ -Fe<sub>3</sub>Zn<sub>10</sub> and martensite boundaries [4]. Figure 2.14 shows EDS analysis along a PAGB in a Zn-coated PHS which demonstrates the formation of  $\alpha$ -Fe(Zn) thin layer in between  $\Gamma$ -Fe<sub>3</sub>Zn<sub>10</sub> and martensite ( $\alpha'$ ) by indicating the zinc concentration profile.

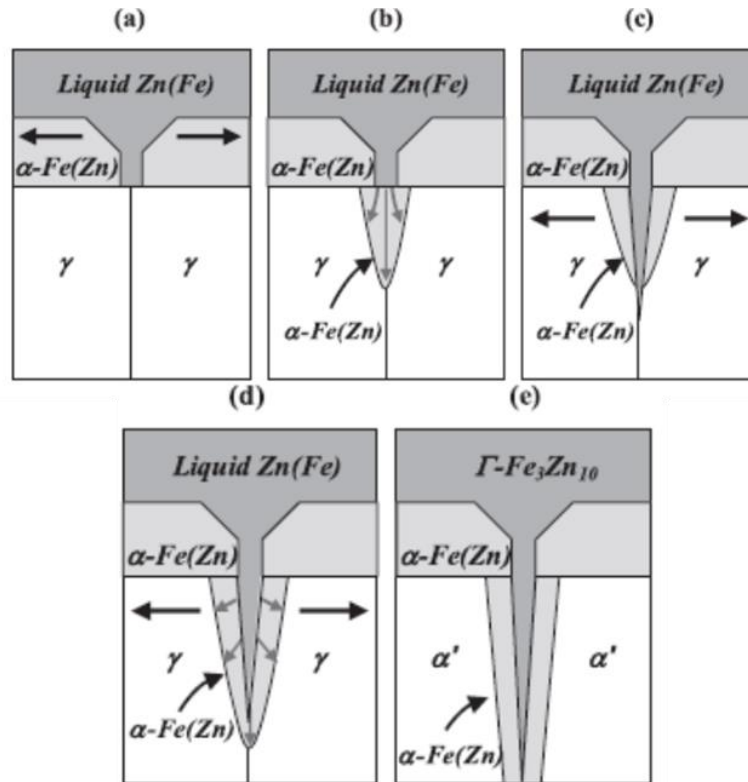


Figure 2. 13: Schematic diagram of liquid metal embrittlement process in Zn-coated PHS [4].

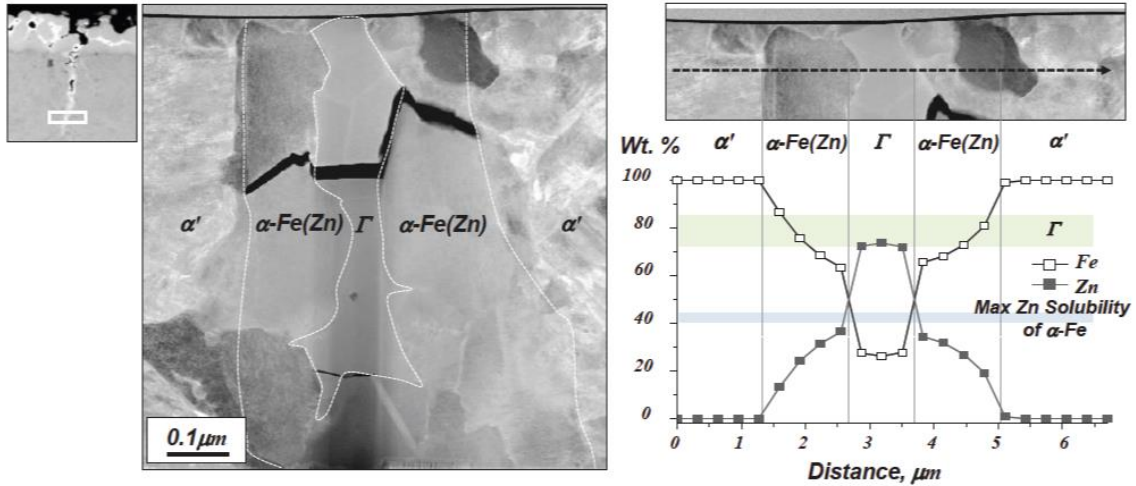


Figure 2. 14: TEM cross-section (left) of zinc diffusion in a Zn coated 22MnB5 PHS. (Right) EDS linescan analysis across the grains [4].

## 2.7 Diffusion of Zn in Steels

It has been observed in the literature that in the case of Zn-coated PHS studies, zinc diffusion at high temperatures plays an extremely important role in embrittlement [1, 46]. Janik et al. studied the extent of zinc diffusion into the  $\gamma$ -Fe(Zn) austenite phase during the annealing process prior to hot press forming and its correlation to crack depth in  $\gamma$ -Fe(Zn) substrate [46]. A finite difference model (FDM) was created to explain zinc diffusion and growth of the coating thickness during the isothermal annealing of the Zn-coated 22MnB5 at 900°C. Figure 2.15 shows the schematic 1D model of zinc diffusion at 900°C. The model consisted of the  $\gamma$ -Fe(Zn) substrate, the  $\alpha$ -Fe(Zn) coating, and the (ZnO) oxide layer on the outer surface. Zinc diffusion occurred from the interface  $S_2$  through the  $\alpha$ -Fe(Zn) coating into the  $\gamma$ -Fe(Zn) substrate. A Stefan condition was used to calculate the mass transfer rate through  $S_1$  interface [46].

$$v|_{x=S_1} = \left( D_{Zn}^{\gamma} \frac{\partial C_{Zn}^{\gamma}}{\partial x} - D_{Zn}^{\alpha} \frac{\partial C_{Zn}^{\alpha}}{\partial x} \right) (C_{Zn}^{\alpha/\gamma} - C_{Zn}^{\gamma/\alpha}) \quad (2.6)$$

Where  $D_{Zn}^{\gamma}$  and  $D_{Zn}^{\alpha}$  are effective diffusion coefficients,  $C_{Zn}^{\gamma}$  and  $C_{Zn}^{\alpha}$  are zinc concentrations in  $\gamma$ -Fe(Zn) and  $\alpha$ -Fe(Zn), respectively.  $C_{Zn}^{\alpha/\gamma}$  and  $C_{Zn}^{\gamma/\alpha}$  are equilibrium concentrations at both sides of the coating-substrate interface  $S_1$ . Concentration gradients followed Fick's second law [46]:

$$\frac{\partial C}{\partial t} = D \frac{\partial^2 C}{\partial x^2} \quad (2.7)$$

Where  $C$ ,  $D$ ,  $t$ , and  $x$  are zinc concentration (wt.%), diffusion coefficient ( $m^2s^{-1}$ ), time (s) and space coordinates (m), respectively.

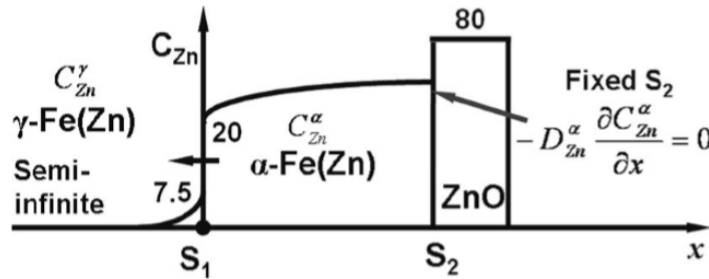


Figure 2. 15: 1D finite difference model of Zn-coated 22MnB5 at 900°C [46].

In this model, the interface  $S_2$  was considered stationary and the diffusion flux of this interface was equal to zero. Because the oxide layer was quite thin, the oxidation kinetics were linear. In this study, Zn-coated 22MnB5 samples were annealed at 900°C for 240s, 300s, 480s and 600s. The experimental data was in good agreement with the proposed model. In the end, diffusion calculations indicated that the effective diffusion coefficient of zinc is  $5.00 \times 10^{-13} m^2s^{-1}$  in the  $\alpha$ -Fe(Zn) and  $1.13 \times 10^{-14} m^2s^{-1}$  in the  $\gamma$ -Fe(Zn) substrate [46]. Janik reported that by increasing annealing times from 240s to 600s, the coating thickness increased while zinc concentration in

the coating layer decreased. Secondly, the zinc diffusion rate was close to that of bulk diffusion in the  $\alpha$ -Fe(Zn) coating, while the diffusion rate was between that of bulk and grain boundary diffusion in the  $\gamma$ -Fe(Zn) substrate [46].

Diffusion is a critical physical process for studying the micro-crack formation during the press hardening process. Likewise, Janik et al. stated that SME of zinc led to the formation of micro-cracks during the DHPF process. Figure 2.16 shows the proposed SME mechanism by Janik for micro-cracking in the Zn-coated PHS [46]. The schematic clearly shows that by increasing the annealing temperature from 800°C (Figure 2.16 a) to 900°C with a holding time of 240s (Figure 2.16 b), the  $\Gamma$ -Fe<sub>3</sub>Zn<sub>10</sub> phase (Zn-rich phase) disappeared. Due to variations of zinc concentration induced by changing the annealing time, the depth and the shape of the micro-cracks were also affected. According to the proposed SME mechanism, lower zinc concentrations could not sufficiently feed the micro-crack by the transportation of solid zinc atoms. Thus, blunted micro-cracks formed at longer annealing times.

Accordingly, Figure 2.17 shows an SEI image and corresponding Zn EDS analysis (map and linescan) of a Zn-coated 22MnB5 steel annealed at 900°C for 240s. It can be seen that zinc enrichment enhanced along the grain boundaries of an entirely  $\alpha$ -Fe(Zn) coating. Janik et al. reported this region might be the location of previous Zn-rich  $\Gamma$ -Fe<sub>3</sub>Zn<sub>10</sub> [46].

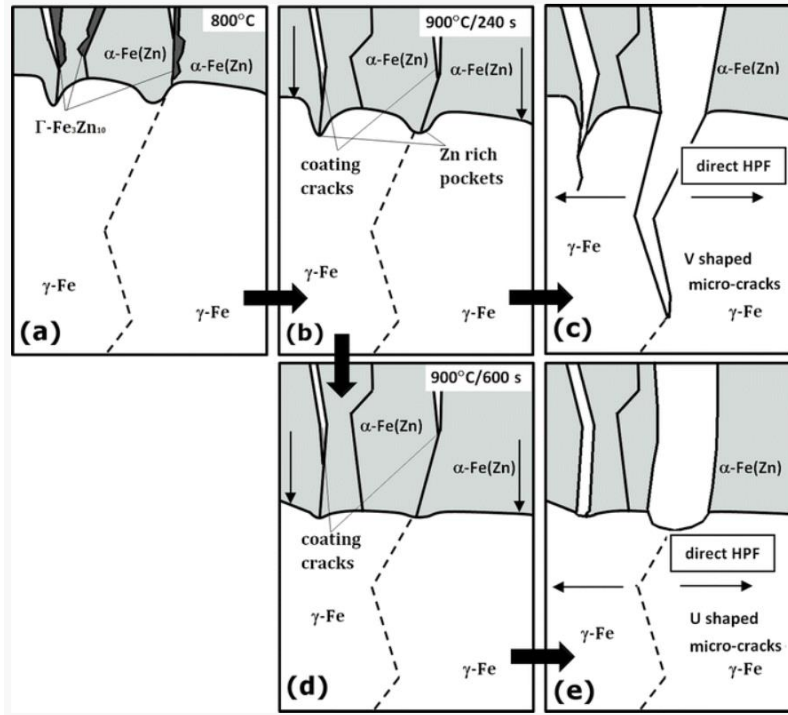


Figure 2. 16: Schematic of the SME mechanism of micro-cracking in Zn-coated press hardened boron steels [46].

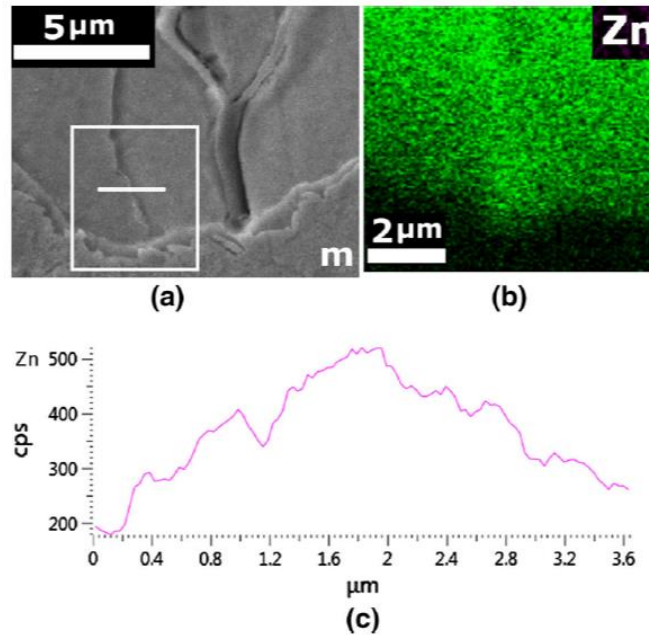


Figure 2. 17: SEI micrograph of the  $\alpha$ -Fe(Zn) grain boundary and the corresponding Zn EDS analysis (map and linescan) [46].

## 2.8 Mechanical Properties of Zn-Coated PHS

Figure 2.18 shows the engineering stress-strain curves for uncoated and Zn-coated 22MnB5 PHS deformed at 850°C reported by De Cooman [2]. Sharp losses in ultimate tensile strength (UTS) and ductility of the Zn-coated material were observed compared to the that of uncoated material as a result of LME.

Another study on the mechanical properties of the Zn-coated PHS was performed by Fan and De Cooman [1]. Figure 2.19 shows stress-strain curves for the deformed bare and coated samples prepared at different conditions. All bare and GI coated 22MnB5 samples were annealed at 850°C for 4min, then deformed to 40% engineering strain. The bare 22MnB5 steel annealed at 850°C for 4min showed a UTS of about 150 MPa with 40% elongation. However, the same steel with GI coating showed elongation of around 8%, with a lower UTS (Figure 2.19). Another sample that was studied was a GI coated 22MnB5 annealed at 850°C for 4min and subsequently deformed at 700°C which showed a higher UTS of 225 MPa with 40% elongation.

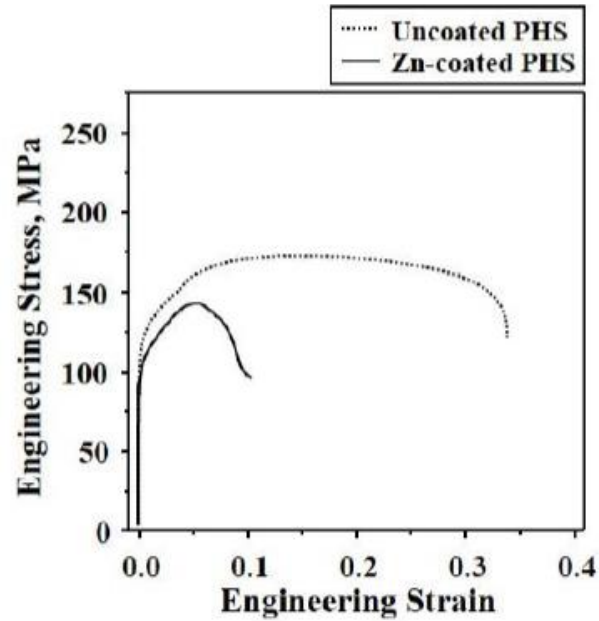


Figure 2. 18: Zn-coating effect on the mechanical properties of a PH 22MnB5 steel at 850°C [2].

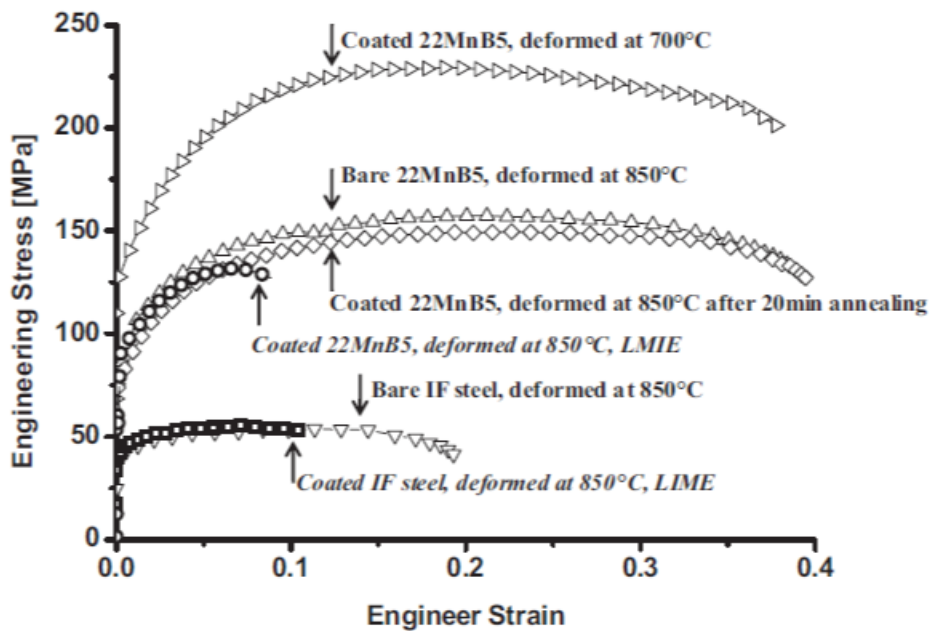


Figure 2. 19: Stress-strain curves for samples deformed at different conditions [1].

Therefore, LME clearly affects the mechanical properties of the stressed parts. Several suggestions have been proposed in order to mitigate LME occurrence in press hardened steels. One suggestion was to deform the material below the peritectic point such that no liquid zinc was present [1, 32]. Relatively, Figure 2.20 clarifies this solution by showing the corresponding BSE images of the two discussed conditions in Figure 2.19. Figure 2.20 shows zinc distribution obtained by WDS for GI 22MnB5 samples (a) annealed at 850°C for 4min and subsequently 40% strained at 700°C and (b) annealed at 850°C for 20min and then 40% strained at the same temperature. The sample strained at 700°C showed the presence of the  $\Gamma$ -Fe<sub>3</sub>Zn<sub>10</sub> phase which likely meant no liquid zinc was present during the deformation process. In Figure 2.19, it was observed that the stress-strain curve of the deformed sample at 700°C showed a highest UTS which confirmed LME was inhibited. The sample annealed at 850°C for 20min and 40% strained (Figure 2.20 b) showed better ductility compared to the sample annealed at 850°C for 4min and subsequently deformed. This implies that LME was likely prohibited by employing a longer annealing time; however, the UTS was not as high as the sample deformed below the peritectic point [1, 32].

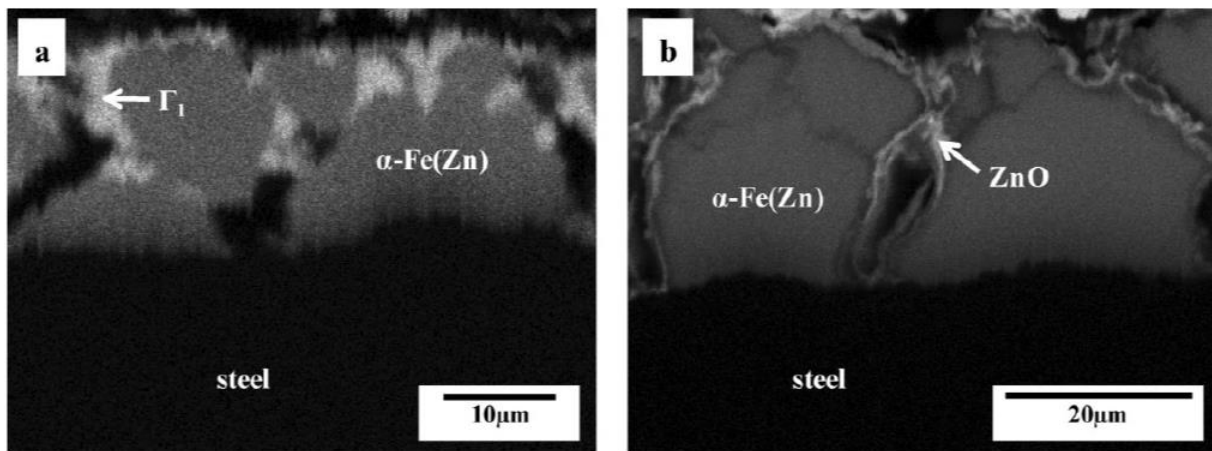


Figure 2. 20: Zinc distribution obtained by WDS for a GI 22MnB5 sample annealed at (a) 850°C for 4min and subsequently 40% strained at 700°C and (b) at 850°C for 20min and 40% strained [1].

Figure 2.21 shows the stress-strain curves for Zn-coated PHS with three proposed LME mitigation strategies [2]. Figure 2.21 shows (a) lower initial coating weight, (b) longer annealing time, (c) increased Al content in the coating composition. It can be seen that LME didn't occurred for lower zinc coating weights of 38 g/m<sup>2</sup> and 63 g/m<sup>2</sup>, however, the stress-strain curve for the highest zinc content of 105 g/m<sup>2</sup> illustrated that LME had occurred. For both 38 g/m<sup>2</sup> and 63 g/m<sup>2</sup> zinc contents, the  $\Gamma$ -Fe<sub>3</sub>Zn<sub>10</sub> phase was not observed. Therefore,  $\alpha$ -Fe(Zn), the main constituent of the coating of these two samples, was important for impeding LME.

Increasing the annealing time was another effective solution to reduce or eliminate LME with a similar explanation of developing a fully  $\alpha$ -Fe(Zn) coating (Figure 2.21 (b)) [1, 2]. An increase in the Al content from 1.6 wt.% to 3 wt.% (Figure 2.21 (c)) was observed to be beneficial to avoid LME. However, the detailed mechanism by which higher Al content retards LME is still being investigated.

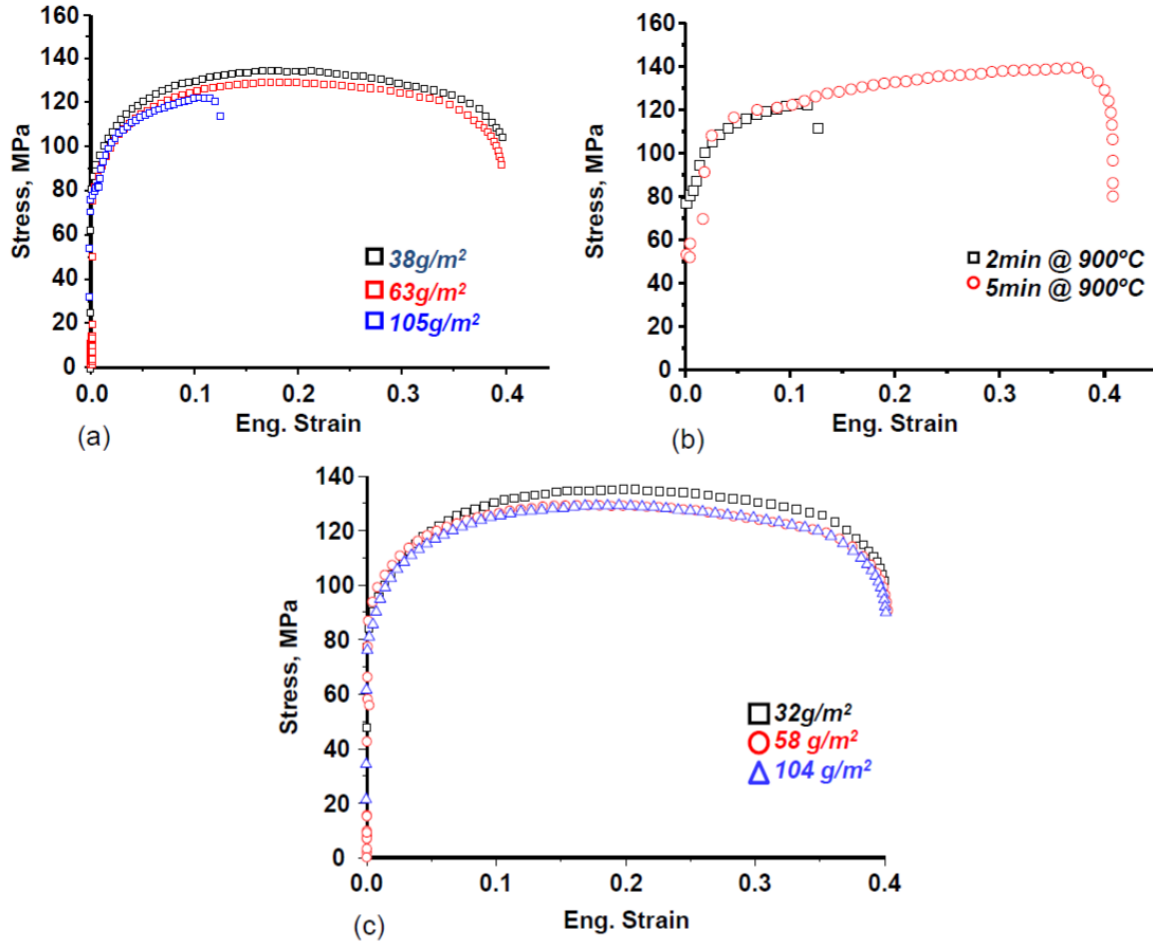


Figure 2. 21: High-temperature stress-strain curves for a Zn-1.6% Al-1.6% Mg coated PH steel, influence of (a) initial zinc coating weight (38 g/m<sup>2</sup> vs. 63 g/m<sup>2</sup> vs. 105 g/m<sup>2</sup>), (b) annealing time (2min vs. 5min), (c) higher Al content (3.2 wt.%) in the coating composition for different zinc coating weights – Note that in the case of higher Al content, higher loading of Zn didn't exhibit LME [2].

## 2.9 Corrosion Properties Zn-Coated Press Hardened Steels

Corrosion protection is another desired property for the application of Zn-coated press hardened steels in the automotive industry. Zn-based coatings are applied to act as sacrificial anodes to

protect the substrate from corrosion. The presence of different Fe-Zn phases and the thickness of the coating as a result of the heat treatment cycles influences the corrosion properties of the final part. As reported by Autengruber et al. [15], a 20  $\mu\text{m}$  coating layer consisting of  $(\alpha\text{-Fe})\text{Zn}$  and  $\Gamma\text{-Fe}_3\text{Zn}_{10}$  phases, created by austenitization at 910°C, showed five times longer corrosion protection compared to the as-received sample with a 10  $\mu\text{m}$  coating layer. Later galvanostatic measurements showed higher coating thickness leads to a higher corrosion resistance and lower corrosion rate [15].

During corrosion testing, red corrosion products were observed due to high Fe content in the Zn-coated sample, as reported by Faderl [1]. Furthermore, zinc concentration plays an important role for cathodic corrosion protection. Even when cracks form, the Zn coating layer can still protect the substrate. Several studies have reported that a zinc content in the  $(\alpha\text{-Fe})\text{Zn}$  coating layer within 17-44 wt.% [47] or 20-30 wt.% [48] is required for a robust cathodic protection. It was also reported that at least 15 vol%  $\Gamma\text{-Fe}_3\text{Zn}_{10}$  in the coating layer was necessary in order to provide robust cathodic protection [51].

## **2.10 Weldability and Paintability Properties of Zn-Coated Press**

### **Hardened Steels**

The resistance spot weldability of both GI and GA steel after the hot stamping process was studied by Faderl and Genderen [1], respectively. In both cases, the surface oxides increased the contact resistance [1]. Therefore, thorough surface cleaning prior to the spot welding must be considered. During DHPF, holding time can also have a significant role in contact resistance since

increasing annealing time resulted in the formation of thicker surface oxides. Tensile shear strengths of the welded parts were found to be equivalent regardless of the presence of the coating, indicating that the mechanical properties of the welded parts were unaffected by the zinc coating layer. On the other hand, Manzenreiter mentioned that partial heating can result in different mechanical properties of a welded Zn-coated PHS sheet [49].

Similar to the above weldability properties, surface oxides can impact the paintability properties of the Zn-coated press hardened steels. A phosphate layer is usually applied on the surface of the steel in order to increase paint adhesion for automotive applications. During this process the steel is immersed in a zinc phosphate solution to create a phosphate film on the steel surface. After the surface oxide removal process, the phosphate layer is thus more uniform and improves paint adhesion. Moreover, the phosphatability and paint adhesion to GI coatings after hot stamping has also been found to be sufficient [1].

### **3. Research Objectives**

Micro-cracking is a drawback of Zn-coated press hardened steels in the process of hot press forming. Previous literature has stated several mechanisms for the formation of the micro-cracking [19, 22, 34]. One of the most commonly used mechanisms for micro-cracking in Zn-coated press hardened steels is liquid metal embrittlement (LME) [4-6]. During hot press forming, LME is induced by the penetration of liquid zinc along the prior austenite grain boundaries of the substrate which negatively impacts mechanical properties by causing premature failure of the part [6]. The mechanism of LME is well-established; however, it can not be applied to all cases of

embrittlement in Zn-coated PHS. Therefore, in this project, the objective is to determine a new mechanism for micro-cracking in Zn-coated PHS. It is hypothesized that due to solid-state diffusion of zinc along the grain boundaries of the coating and the prior austenite grain boundaries of the substrate, a Zn-enriched layer ( $\alpha$ -Fe(Zn)) would form along these grain boundaries. Consequently, these areas are susceptible to crack initiation and propagation after tensile testing. Changing coating constituents as a function of annealing time was employed to assess zinc concentration variation at the grain boundaries.

Zn-coated 22MnB5 steel sheets were annealed at 900°C for different annealing times (30 s, 60s, 120s, 180s, 240s, 300s, 420s, 600s, 780s), and were then planar or U-shaped die-quenched with an average cooling rate of 100°Cs<sup>-1</sup>, resulting in a fully martensitic substrate microstructure. In order to determine the zinc distribution into the bulk substrate, four sets of samples were examined. The first set of samples were annealed for 30 s (the shortest time) and 780s (the longest time) and die-quenched while the second set comprised tensile specimens from the 30 s and 780s annealing times which were subsequently pulled to failure. The third and fourth set of samples were selected from two areas (top surface and outer wall surface) on the U-shaped die-quenched samples that were annealed for 30 s and 780s. U-shaped die-quenched DHPF allowed for the production of in-situ micro-cracks during forming while the ex-situ micro-cracks formed during tensile testing of the planar die-quenched sample.

## **4. Experimental Methods**

In order to determine the origin of micro-cracking, as-galvanized coatings were annealed at a typical press-hardening austenization temperature of 900°C. The primary experimental variable was annealing time which was varied from 30 s to 780s. Therefore, the coating thickness and microstructure were expected to be affected as a result of zinc diffusion and the austenite to martensite transformation. Finally, two sets of samples were chosen for high resolution electron microscopy to determine the zinc distribution along the: 1) coating grain boundaries, 2) prior austenite grain boundaries and 3) micro-cracks in the fractured samples.

### **4.1 Steel Chemistry and Sample Preparation**

The chemical composition of the as-received steel substrate (22MnB5) is shown in Table 4.1. The substrate composition was experimentally determined by the inductively coupled plasma - optical emission spectroscopy (ICP-OES) technique. All experimental steels were provided by ArcelorMittal Dofasco (Hamilton, ON) in the as-galvanized condition, having a thickness of 1.5 mm with a target Zn coating weight of 70 g/m<sup>2</sup>/side (i.e. GI70). In order to assess the coating weight of the GI70 samples, ASTM A90/A90M [50] was executed, which found that the zinc coating weight on the top and bottom sides averaged 72 to 75 g/m<sup>2</sup> per side, respectively.

Table 4. 1. Chemical composition of the as-received 22MnB5 steel grade (wt.%).

<b>Chemical Composition (mass%)</b>			
C	Mn	B	Si
0.22	1.17	0.0025	0.25

Two sizes of experimental coupons were prepared with dimensions of 30 mm (in the transverse direction (TD)) x 50 mm (in the rolling direction (RD)), and 120 mm × 120 mm, respectively. Smaller coupons were used for the tube furnace and larger coupons were used for the die-quenching process. Before any heat treatments, the experimental coupons were cleaned with acetone followed by cleaning with ethanol to remove all surface contaminants, followed by drying.

## **4.2 Heat Treatments**

### **4.2.1. Coating Microstructural Evolution**

This section details the heat treatments carried out to evaluate the effect of annealing time on Fe-Zn phase formation and, therefore, the microstructural evolution of the final coating. Two types of heat treatments were performed using two different furnaces in an ambient atmosphere: a tube furnace and a box furnace, with different cooling conditions being applied. Figure 4.1 shows the tube furnace with parallel gas quenching platens using compressed air. The purpose of annealing with the tube furnace was to study the coating microstructure microstructural evolution as a function of time at the peak annealing temperature of 900°C. The

30 mm x 50 mm coupons were used for these heat treatments such that the coupon surface was parallel to the cooling platens. The coupons were placed in the tube furnace using a slider and annealed at 900°C to reach the target temperature. For the annealing cycles, the start of the experimental annealing time began when the sample temperature reached 890°C in the furnaces. After reaching to 890°C, the actual experimental annealing time varied from 30 s to 780s began. Time-temperature profiles were measured using a 0.5 mm K-type thermocouple welded to the centre of each coupon. A typical time-temperature profile of the GI70 microstructural evolution samples prepared with the tube furnace can be found in Figure 4.2.

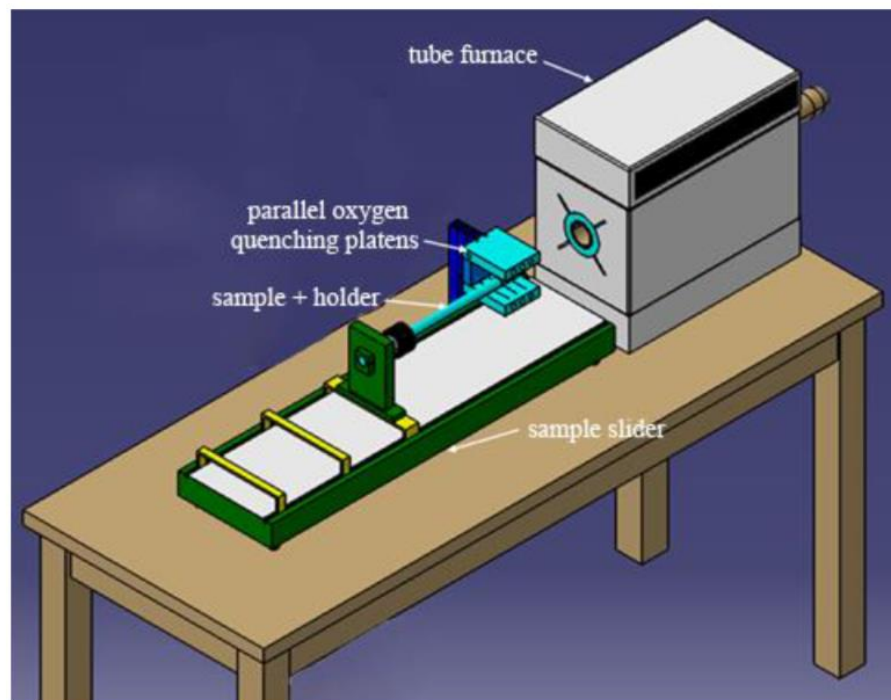


Figure 4. 1: Schematic of the tube furnace set up for the coating microstructural and diffusion study [51].

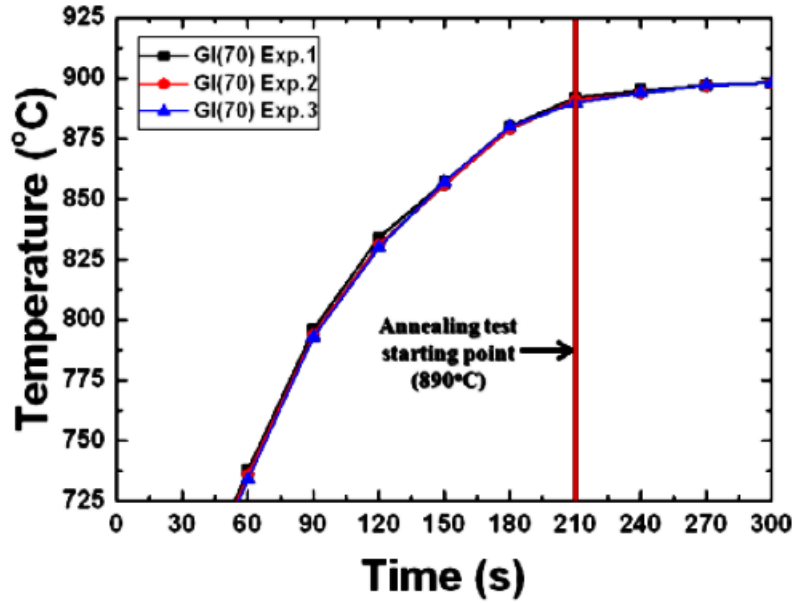


Figure 4. 2: Typical time-temperature profile for microstructural evolution samples.

#### 4.2.2. Planar die Direct Hot Press Forming (DHPF)

Figure 4.3 shows the thermomechanical set up for the direct hot press forming (DHPF) experiments on GI70 coated 22MnB5 substrates, a 250kN MTS tensile frame was used for this purpose. A conventional box furnace under air atmosphere was used to austenitize coated samples at 900°C prior to DHPF. The MTS frame had two parallel water-cooled flat dies system. The box furnace was located close to the die-quenching section in order to have a rapid transfer between heating and die-quenching sections. During DHPF, the frame speed was 1 mm/min, which applied an approximate compressive load of 350 kN on the coated samples.

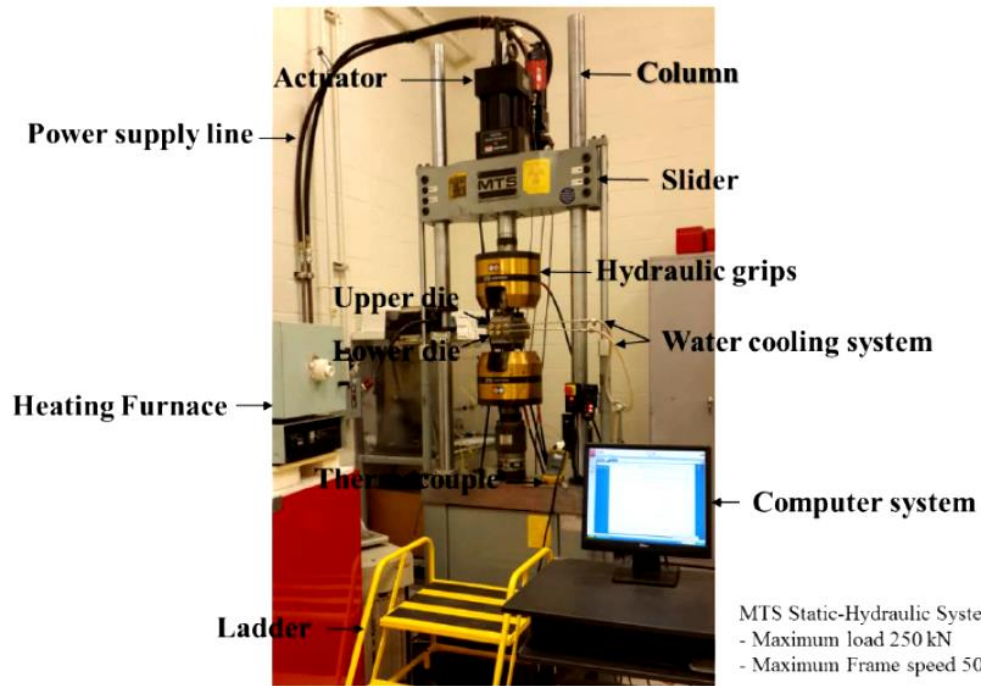


Figure 4. 3: Experimental apparatus for DHPF including a conventional box furnace and a conventional 250kN MTS tensile frame [51].

The cooling rates for both the water-cooled DHPF platens and parallel gas quenching platens are also stated in Table 4.2. The average calculated cooling rate obtained from compressed air quenching was  $75^{\circ}\text{Cs}^{-1}$ . The average cooling rate for DHPF was approximately  $100^{\circ}\text{Cs}^{-1}$ . Therefore, the microstructure of the substrate for all coated samples showed an almost to fully martensitic microstructure. Samples were held at  $900^{\circ}\text{C}$  for the annealing times presented in Table 4.2.

Table 4. 2. Experimental annealing and cooling conditions.

Heat treatment process	Annealing time (s)	Cooling rate ( $^{\circ}\text{Cs}^{-1}$ )

<b>Tube furnace - compressed air quenching</b>	30, 60, 120, 180, 240, 300, 420, 600, 780	75
<b>Box furnace - water-cooled die quenching</b>	30, 60, 120, 180, 240, 300, 420, 600, 780	100

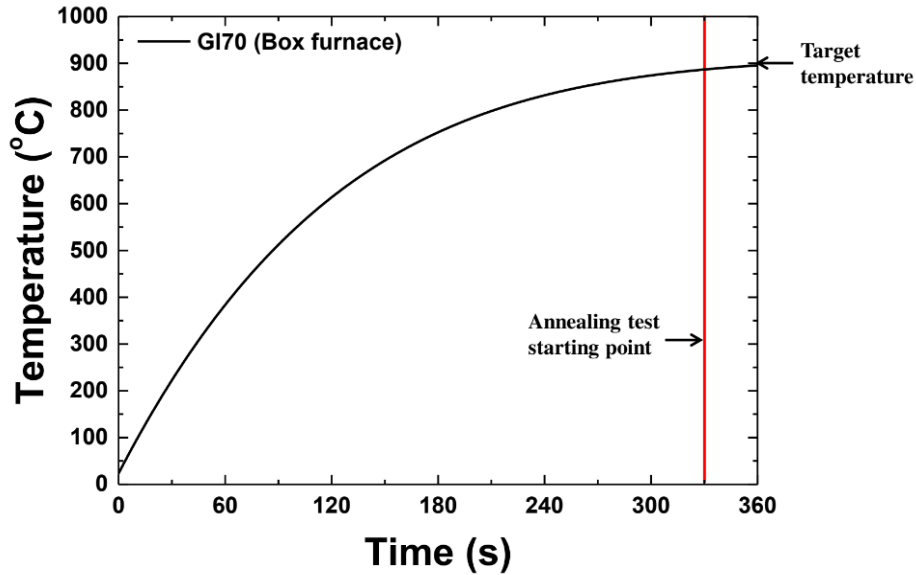


Figure 4. 4: Time-temperature profile for a conventional box furnace.

#### 4.2.3. U-Shaped Die Direct Hot Press Forming (DHPF)

Planar die DHPF followed by tensile testing (details are explained in section 4.3) was performed in order to study the basics of micro-cracking process in the Zn-coated 22MnB5 samples. For the U-shaped die-quenching experiments, the 120 mm x 120 mm panels were used and the procedure was similar to the planar die DHPF except that the planar dies were replaced by U-shaped dies in the tensile frame. This produced a more complex stress/strain state in the formed steel and allows for the production of in-situ micro-cracks during forming rather than the ex-situ cracks formed during tensile testing of the planar die-quenched samples.

Prior to U-shaped DHPF, panels were annealed in the box furnace, as specified in Table 4.2. Again, the box furnace is located close to the die-quenching apparatus in order to have the rapid transfer between two sections. During U-shaped die-quenching, various strain paths were applied to different portions of the panels since the samples underwent a mixture of tension, compression, and bending [5]. Figure 4.5 shows a as-formed U-shaped die sample. During this process, the coated samples were exposed to varying strain conditions throughout the part. This will be discussed further in detail.

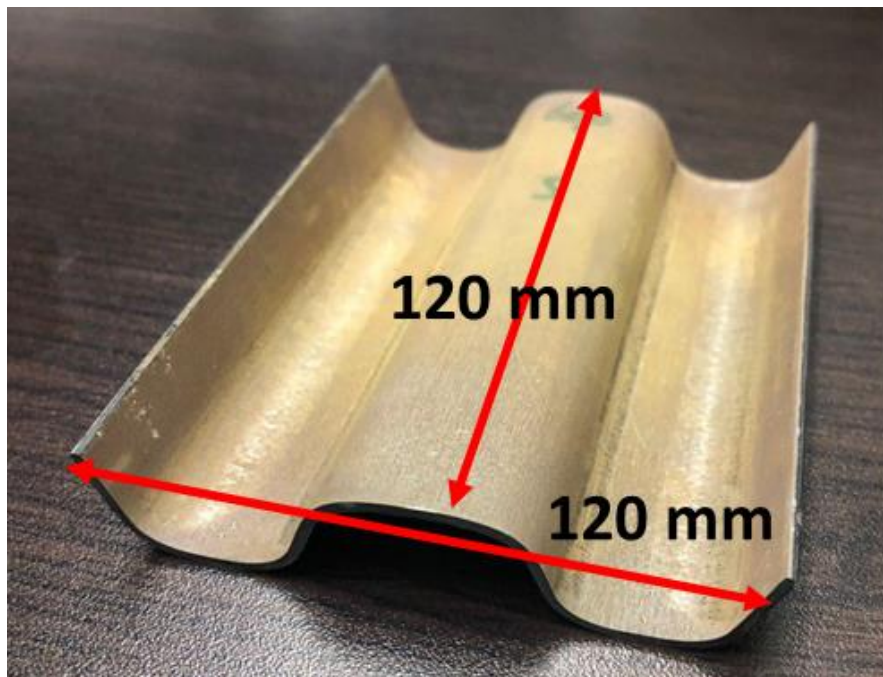


Figure 4. 5: Dimensions of the U-shaped die used in 250kN MTS tensile frame for DHPF.

## 4.3 Tensile Testing

### 4.3.1. Planar Die DHPF Samples

Uniaxial tensile tests were performed at room temperature using an Instron 100 kN testing frame with a cross-head speed of 1 mm/minute. Samples were first prepared by planar die DHPF as specified in section 4.2.2. Then, sub-sized tensile samples were machined using ASTM E8/E8M from the center of the experimental panels. Sample extension during tensile testing was monitored using a 5 mm contact extensometer in all cases. In order to calculate engineering stress and strain equations (4.1) and (4.2) were used.

$$\sigma = \frac{F}{A_0} \quad (4.1)$$

$$\varepsilon = \frac{\Delta L}{L_0} \quad (4.2)$$

Where  $\sigma$  is engineering stress in MPa,  $F$  is the tensile force in N,  $A_0$  is the original cross-sectional area prior to tensile testing of the tensile gauge in  $\text{mm}^2$ ,  $\varepsilon$  is the engineering strain,  $\Delta L$  is the change in gauge length in mm, and  $L_0$  is the original gauge length prior to testing in mm [52]. Tests were repeated in triplicate for all samples. Error bars were determined using the 95% confidence interval over three repeated experimental measurements per annealing time.

### 4.3.2. U-Shaped DHPF Samples

Sub-sized tensile samples for U-shaped DHPF were machined using ASTM E8/E8M from the walls and the top surface of the U-shaped samples. However, since the sub-sized samples were smaller than 100kN tensile frame 10kN tensile frame with a cross-head speed of 1 mm/minute was

executed instead. Engineering stress-strain curves were calculated using the same equations in section 4.3.1. Sample extension during tensile testing was monitored using a 5 mm contact extensometer in all cases. Tests were repeated in duplicate for all samples. Error bars were determined using the 95% confidence interval over two repeated experimental measurements per annealing time. After pulling the samples to fracture, the strain measurement was performed using Digital Image Correlation (DIC) in three dimensional analysis which is explained in detail in section 4.4.

#### **4.4 Digital Image Correlation (DIC) in Three Dimensions (3D) Analysis**

DIC in three dimensional (3D) analyses was used to determine major and minor strains for the U-shaped coupons during DHPF [53]. First, a random speckle pattern was sprayed on the object's surface with white and black spray paint. Therefore, it was possible to recognize and calculate the surface strain on the object under loading. This technique requires the use of images taken in sequence over a period of time [18]. Two sets of images of a target location were taken from separate camera angles for 3D correlation. A system calibration was needed to resolve the 3D space and then the acquired data was utilized to correlate the images for the determination of different portions of strains [53, 54]. The DIC software employed in these experiments was ARAMIS v 6.3.0 (GOM mbH, Braunschweig, Germany). A 120 mm x 120 mm panel was used for calibration of the ARAMIS system. The calibration deviation determined by the ARAMIS system was 0.1 pixels. This calibration deviation was within an acceptable range and resulted in a successful calibration. The determined measuring volume was 55/43/5 mm (Height/Width/Depth). Figure 4.6 shows 3D DIC strain profiles for tension (major strain) and

compression (minor strain) on a GI70 coated 22MnB5 substrate after U-shaped die DHPF. The outer wall of the deformed sample clearly underwent the highest tensile load while the top surface had barely deformed under compression. Although some areas were not pixelated, it did not negatively affect the final measurements. Three sections were performed on the U-shaped sample in order to minimize the calibration deviation.

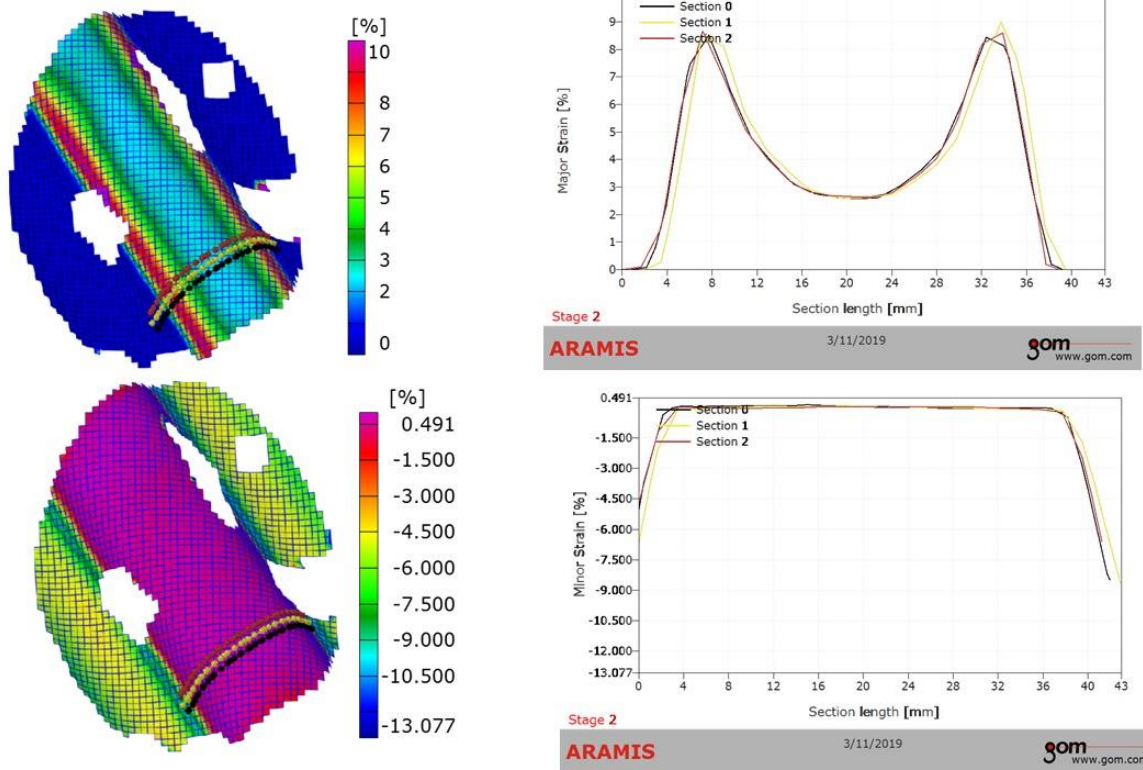


Figure 4. 6: 3D DIC strain profiles for tension (major strain) and compression (minor strain) on a GI70 coated 22MnB5 substrate after U-shaped die DHPF.

## 4.5 X-Ray Diffraction (XRD)

XRD was performed on the coated samples after annealing and subsequent quenching to quantitatively determine the volume percentage of each phase. A Bruker Mo Smart APEX2 diffractometer with Co  $K\alpha_1$  ( $\lambda = 1.79026 \text{ \AA}$ ) radiation was used, and each scan was conducted between the two-theta ( $2\theta$ ) angles of 10-90°. Diffraction angles were conducted with 0.02° step interval and total step times of 600s were used to collect the data. A 1 mm collimator and slit size were used. The diffraction data was then analyzed using Diffrac Eva and TOPAS5 software for quantitative phase ratio analysis. Each specimen was positioned such that the X-rays diffracted from the surface of the coating. The calculated penetration depth of the X-rays into the Fe-Zn coating was estimated up to about 40  $\mu\text{m}$ . Therefore, it was expected that X-ray diffraction would be sufficient for phase identification through the alloyed layers. Error bars were determined using the 95% confidence interval over three repeated experimental measurements per annealing time.

## 4.6 Electron Microscopy (SEM-EBSD) Sample Preparation

In order to prepare the annealed GI70 samples for scanning electron microscopy on the cross-sectional view. Polishing details are shown in Table 4.3. First, the samples were mounted and ground using abrasive SiC papers. Grinding was continued until no scratches from the previous grit could be seen under an optical microscope (OM). The samples were then polished with 3 and 1  $\mu\text{m}$  diamond suspensions. The samples were final polished using colloidal silica suspension (0.04  $\mu\text{m}$ ). After each polishing step, samples were dabbed with a cotton ball soaked in ethanol,

and ultrasonicated in ethanol for 1 min, then blown dry with a hot air stream. It was extremely important to ensure that the samples were not in contact with water (because corrosion of the coating can occur) by using water-free diamond suspensions for the polishing steps and ethylene glycol in OPS solution. All the grinding and polishing steps were performed using Struers automatic polisher.

For EBSD sample preparation, the importance of obtaining a scratch-free mirror-like surface is quite high. A cross-sectional polisher (CSP) can produce a surface with little roughness over a wide area (larger than 500  $\mu\text{m}$ ) because it can apply minimal distortion or strain on the sample compared to the other techniques of preparation. Additionally, by possessing an isolated system, CSP can eliminate exposure to air which is beneficial for sensitive samples. The CSP uses an argon beam to mill through the cross-section of the sample. Therefore, it is a perfect technique to take advantage of for EBSD sample preparation. Squared pieces with dimensions less than 8 mm x 8 mm were cut from the samples using Struers precision cutter. In order to impede curtaining while performing cross-sectional polishing, a sacrificial mask was placed on top of the sample cross-section. The masking material was a Si wafer with 280  $\mu\text{m}$  thickness and was glued on the sample using TEM epoxy. The samples then underwent the grinding and polishing steps specified in Table 4.3 to prepare a flush surface and minimize curtaining artefacts. A JEOL IB09010 Cross-Sectional Polisher (CSP) was used for final ion polishing using the polished sample/Si wafer assembly described above. A 5 keV argon (Ar) sputtering ion beam with a current varying from 90 to 120  $\mu\text{A}$  was used to do final polishing. Ar ion sputtering was performed for a duration of 10 h.

Table 4. 3. Metallographic preparation for SEM-EBSD.

Surface	Suspension	Lubricant	rpm	Force (N)	Time
SiC paper, #320		DI water	300	15	As needed
SiC paper, #600		DI water	300	10	2 min
SiC paper, #800		DI water	300	10	2 min
SiC paper, #1200		DI water	150	5	2 min
MD-Dac	Water free DP-Susp, 3 $\mu\text{m}$	DP-Blue		5	4 min
MD-Dur	Water free DP-Susp, 1 $\mu\text{m}$	DP-Blue	120	5	4 min
OP-Chem		1:1 OPS + ethylene glycol	120	5	4 min

## 4.7 Scanning Electron Microscopy (SEM) Analysis of the Coating

### Microstructure

In order to assess the morphology and the coating microstructure after heat treatment and die-quenching processes, scanning electron microscopy was carried out in a JEOL 7000F microscope

equipped with energy dispersive X-ray spectroscopy (EDS). All samples were examined in a cross-sectional view. Backscattered electron (BSE) mode was used for both SEM imaging and EDS analysis to investigate Zn diffusion depth and coating phases. Each phase appeared as a different gray level in the BSE images, due to the difference in atomic number contrast, with Zn-rich regions appearing bright, and Fe-rich regions appearing darker. Elemental point analysis, line scans, and map analysis by EDS were carried out to resolve the coating thickness and microstructural constituents. AZtec Oxford Instruments software was used to analyze the EDS data. Working distances of 10 mm and an acceleration voltage of 15 keV were utilized for all SEM-EDS analysis.

#### **4.8 Scanning Auger Microscopy (SAM)**

Auger electron spectroscopy (AES) was performed using a JEOL JAMP 9500F field emission - scanning auger microscope (FE-SAM). SAM-AES was used to provide elemental analysis within the first few atomic layers of the sample surface, specifically to detect the intermetallic phases along the grain boundaries on the fracture surface. The planar die-quenched sample annealed for 30 s was used for this experiment to perform in-situ fracture testing under vacuum. Auger elemental mapping was performed over the cross-section of one sample (30 s) to assess elemental distribution using a probe current of 70 nA. Fe and Zn were included within the scan.

## 4.9 Electron Backscattered Diffraction (EBSD)

A JEOL 7000F FEG-SEM equipped with a Nordlys II EBSD Camera was used to characterise the phase fraction and orientation relationships quantitatively. Additionally, EBSD enabled identification of the coating-substrate interface, which was an important step towards determining zinc distribution along the prior austenite grain boundaries (PAGBs) of the substrate and the grain boundaries (GBs) of the coating. Samples were prepared as specified in section 4.6. AZtec Oxford Instruments software was used for EBSD scanning, and HKL Channel EBSD post-processing software was used to perform map reconstruction. A working distance of 15 mm, step size of 50 to 70 nm and an acceleration voltage of 20 keV was used for all EBSD analyses. The specimen was tilted 70° towards the EBSD detector to increase the backscattered electron yield. When phases are crystallographically similar, EBSD alone cannot separate them. Therefore, a combination of EBSD and EDS ensured phase identification. All present phases in the annealed GI70 coated 22MnB5 substrates had a BCC crystal structure with an  $I-43m$  (217) space group, as shown in Table 4.4. In these cases, phase discrimination using both the EDS and EBSD signals can be applied during mapping, which enabled the phases to be identified separately in the sample.

Table 4. 4. EBSD phases, and their related crystal structure and zinc content.

Phase	Crystal structure/space group	Zn content (wt.%)
$\Gamma$ -Fe <sub>3</sub> Zn <sub>10</sub>	BCC / $I-43m$	60-78
$\alpha$ -Fe(Zn)		10-35
Martensite		

To fulfill the purpose of determining zinc distribution and degree of zinc penetration into the bulk substrate, two sets of samples were examined. The first set of samples were annealed for 30 s (the shortest time) and 780s (the longest time) and die-quenched (U-shaped and planar dies) while the second set comprised tensile specimens from the 30 s and 780s annealing times which were subsequently pulled to failure. The samples are referenced with the labels indicated in Table 4.5.

Table 4. 5. Details on the samples examined for zinc distribution using SEM-EBSD and STEM-EELS techniques.

<b>Material</b>	<b>Annealing time (s) at 900°C</b>	<b>Production history after annealing</b>	<b>Final coating microstructure</b>
<b>30AQ</b>	30	as-quenched by water-cooled U-shaped and planar dies	$\alpha$ -Fe(Zn) + $\Gamma$ -Fe <sub>3</sub> Zn <sub>10</sub>
<b>780AQ</b>	780		$\alpha$ -Fe(Zn)
<b>30TS</b>	30	as-quenched by water-cooled U-shaped and planar dies followed by uniaxial tensile testing	$\alpha$ -Fe(Zn) + $\Gamma$ -Fe <sub>3</sub> Zn <sub>10</sub>
<b>780TS</b>	780		$\alpha$ -Fe(Zn)

## **4.10 Transmission Electron Microscopy (TEM) Sample Preparation by Focused Ion Beam (FIB) Milling**

The Zeiss NVision40 Focused Ion Beam (FIB) using a gallium (Ga) source was utilized on the sample cross-sections for TEM sample preparation. FIB lift-outs were obtained from the samples shown in Table 4.5. For the as-quenched (AQ) samples, areas of interest on each sample were first selected from the EBSD maps. Subsequently, one lift-out was taken from each sample condition such that it contained a grain boundary of the coating, diffusion zone, and prior austenite grain boundary of the substrate. After tensile testing, one micro-crack of the sample that entered into a prior austenite grain boundary of the substrate was extracted by FIB.

## **4.11 Scanning Transmission Electron Microscopy - Electron Energy Loss Spectroscopy (STEM-EELS)**

A Thermo-Fisher-FEI Titan 80-300 HB equipped with a monochromator and a double aberration-corrected (Cs), operated at 200-300 keV was utilized to perform scanning transmission electron microscopy - electron energy loss spectroscopy (STEM-EELS) analysis on the TEM samples as specified in Table 4.5. For STEM imaging, high-angle annular dark field (HAADF) and annular dark field (ADF) detectors with a convergence angle of 19.1 mrad were used. EELS analysis, using a GIF Quantum-K2 prism spectrometer, with a dispersion of 0.1 eV/pixel and a collection semi-angle of 55 mrad was performed for elemental mapping on the samples. GMS3 software was used to

conduct the EELS elemental maps analysis using examined  $L_3$  edges for Zn (1020 eV) and Fe (708 eV) and K edge for O (532 eV).

## 5. Results

### 5.1 SEM Analysis of As-Received Uncoated and Coated 22MnB5 Steel

Figure 5.1 presents an optical image of the GI70 22MnB5 substrate before heat treatment. It can be seen that the as-received (AR) substrate microstructure consisted of pearlite and ferrite, with the grains elongated along the rolling direction. Figure 5.2 shows an optical image of a GI70 22MnB5 substrate after annealing at 900°C for 780s, compressed-air quenched, and subsequently etched with 2% Nital. Fractions of martensite and ferrite were observed in the sample microstructure. Figure 5.3 shows a BSE image of an AR GI70 coated 22MnB5 substrate in a cross-sectional view which displayed the presence of an intermetallic phase close to almost pure zinc on the surface with an average thickness of 10  $\mu\text{m}$ . In Figure 5.4, Al distribution obtained by EDS mapping can be observed at the coating-steel interface. This observation demonstrates the presence of an Al-rich boundary layer between the steel and coating layer known as the inhibition layer ( $\text{Fe}_2\text{Al}_{5-x}\text{Zn}_x$ ) in the AR GI70 coated 22MnB5 material. As was mentioned before, the purpose of the Al addition to the molten zinc bath is to suppress Zn oxidation and evaporation during austenization annealing of PHS [1].

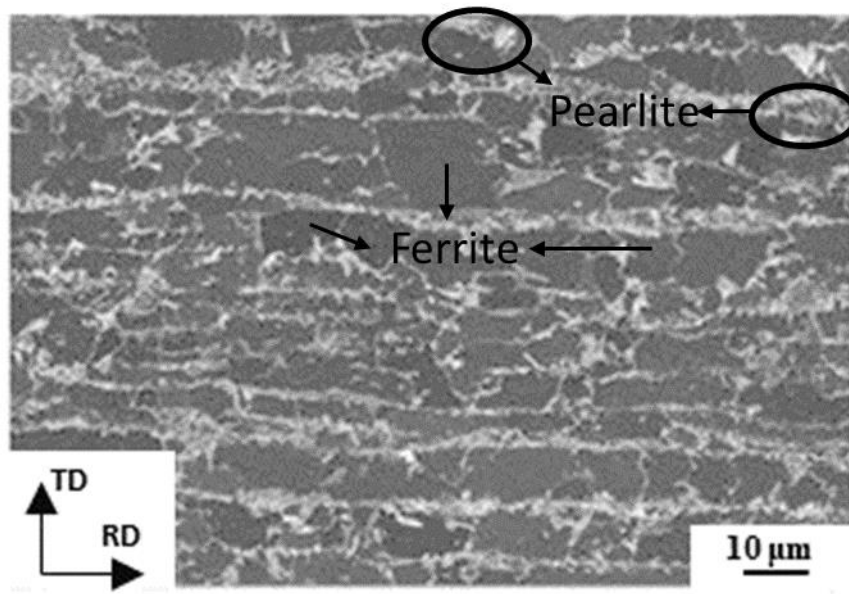


Figure 5. 1: SE image of the as-received GI70 22MnB5 substrate.

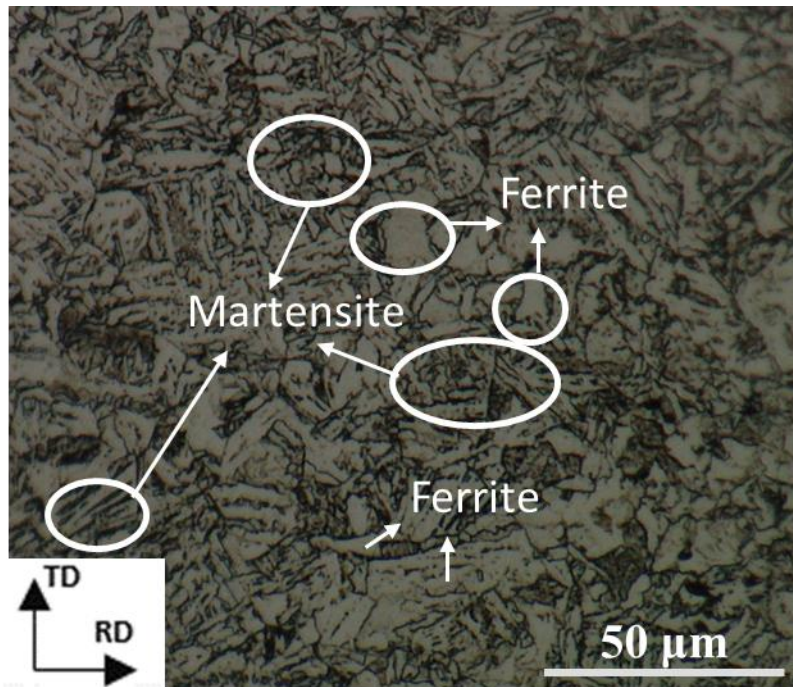


Figure 5. 2: Optical image of GI70 22MnB5 substrate annealed at 900°C for 780s and compressed air quenched.

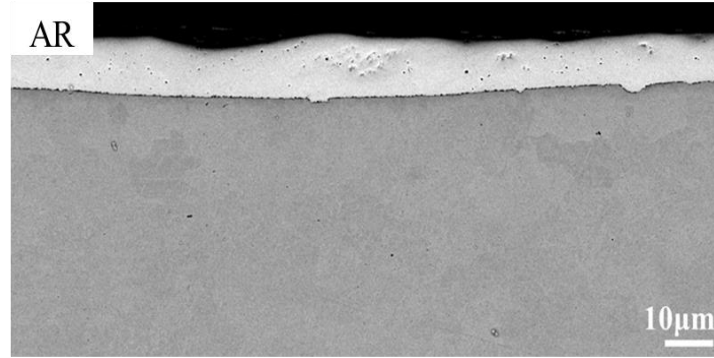


Figure 5. 3: BSE image of an AR GI70 coated 22MnB5 substrate in cross-sectional view.

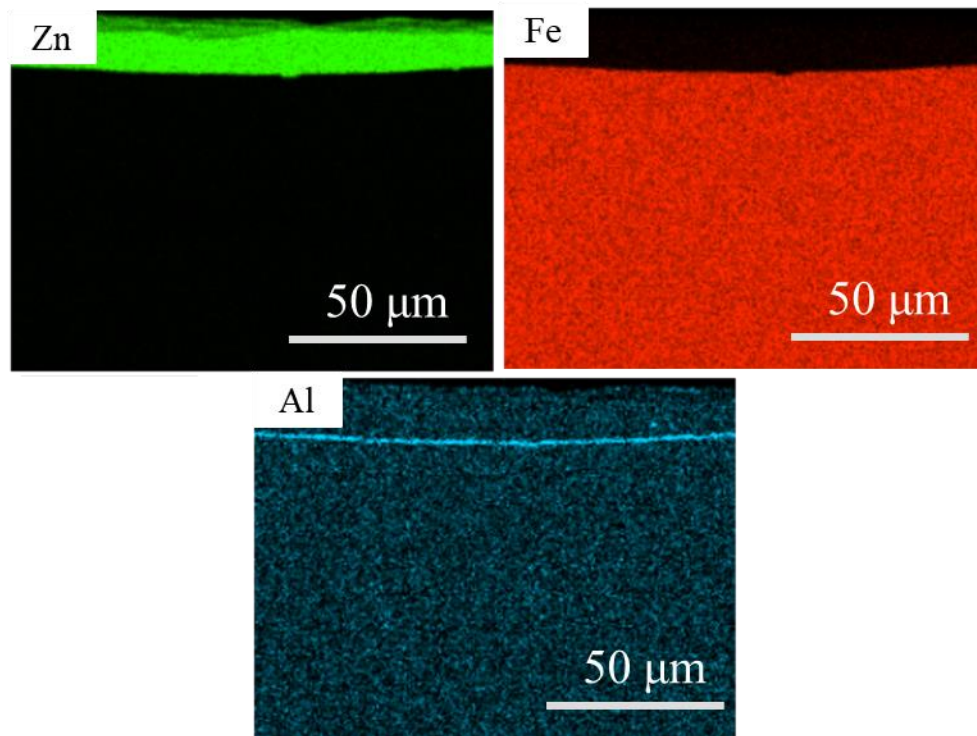


Figure 5. 4: EDS a) Zn distribution, b) Fe distribution, and c) Al distribution map of an AR GI70 22MnB5 substrate in cross-sectional view.

## 5.2 SEM and EDS Related Analysis of the Coating Microstructural Evolution after Heat Treatment and Quenching Processes

At the steel's austenitization temperature of 900°C, the coating had a mixture of solid and liquid phases, the presence and the ratio of these coating constituents changed by the annealing time. During the heating and cooling processes (compressed air gas quenching or die-quenching) the specimen undergoes the peritectic reaction ( $Zn_{liq} \rightarrow \alpha\text{-Fe(Zn)} + \Gamma\text{-Fe}_3\text{Zn}_{10}$ ) at 782°C [6]. However, at 700°C, it was observed that the coating was composed of only  $\Gamma\text{-Fe}_3\text{Zn}_{10}$  prior to passing through the peritectic temperature at 782°C [1, 51]. By holding the sample at 900°C, liquid zinc was being consumed by a diffusion couple process leaving behind  $\alpha\text{-Fe(Zn)}$  grains with lower zinc concentration.  $\Gamma\text{-Fe}_3\text{Zn}_{10}$  is a zinc-rich intermetallic compound and in other words a solidified liquid zinc phase after press hardening process.  $\Gamma\text{-Fe}_3\text{Zn}_{10}$  usually has zinc content of 72.0-76.5 wt.% [1]. Depending on the effective experimental parameters, i.e., initial zinc content, annealing temperature, and in this study different annealing times, the final coating microstructure changed.

Figure 5.5 depicts the coating microstructural evolution of GI70 coated sample annealed at 900°C for all holding times as a function of annealing at 900°C in the tube furnace and subsequently gas quenched with compressed air. After 30 s annealing, the coating consisted of a mixture of  $\alpha\text{-Fe(Zn)}$  and  $\Gamma\text{-Fe}_3\text{Zn}_{10}$  phases.  $\Gamma\text{-Fe}_3\text{Zn}_{10}$  appeared as a brighter phase in the BSE images since had a higher average atomic number versus  $\alpha\text{-Fe(Zn)}$ . By increasing annealing time, the fraction of  $\Gamma\text{-Fe}_3\text{Zn}_{10}$  decreased while  $\alpha\text{-Fe(Zn)}$  increased. Finally, after annealing for 300s,  $\Gamma\text{-Fe}_3\text{Zn}_{10}$  disappeared and only coarse  $\alpha\text{-Fe(Zn)}$  grains made the entire coating layer. This means that for

annealing times longer than 300s, the Zn-rich liquid zinc was consumed in favour of  $\alpha$ -Fe(Zn) formation.

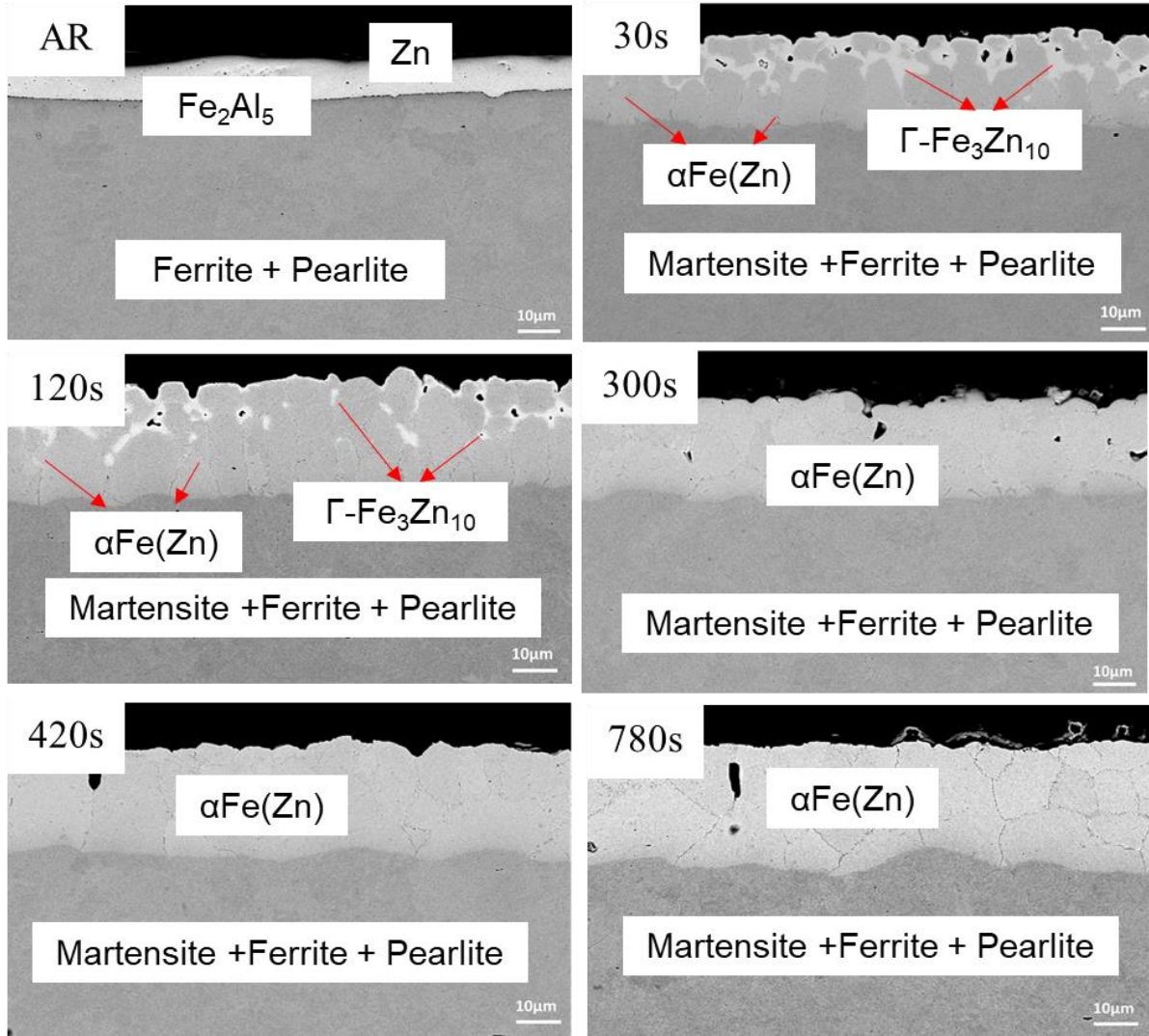


Figure 5. 5: BEI-SEM micrographs GI70 samples in the as-received (AR) condition, and annealed at 900°C for 30 s, 120s, 300s, 420s, and 780s and compressed air gas quenched.

Figure 5.6 displays cross-sectional BEI-SEM micrographs of GI70 coated sample annealed at 900°C for all annealing times in the box furnace and subsequently direct press hardened using the water-cooled planar dies. The coating microstructural evolution was quite similar to when

samples were quenched with compressed air. As described earlier, after annealing for 300s,  $\Gamma$ - $\text{Fe}_3\text{Zn}_{10}$  disappeared and the coating comprised only  $\alpha$ -Fe(Zn) phase. Also, a slight difference in  $\Gamma$ - $\text{Fe}_3\text{Zn}_{10}$  intermetallic phase was observed in SEM images of the gas quenched samples (Figure 5.5) compared to those of the die-quenched ones (Figure 5.6). Due to the higher cooling rates achieved in die-quenching, the phase configuration was slightly further from equilibrium condition; consequently, coating microstructures were slightly different. Therefore, since the whole coating microstructure evolution of both gas and die-quenched samples were quite similar, the focus will be on the DHPF results, which are more industrially relevant. Moreover, the fully martensitic microstructure was clear in the steel matrix at all annealing times (Figure 5.5 and Figure 5.6). A few observed coating cracks in the as-quenched samples were possibly formed due to the applied compression load of 350 kPa by the planar dies.

As specified in Figure 5.4, an EDS map revealed the presence of an  $\text{Fe}_2\text{Al}_{5-x}\text{Zn}_x$  inhibition layer at the coating-steel interface of as-received Zn-coated sample. However, no trace of Al was observed in the coating-substrate interface after the heat treatment. EDS maps of post-annealed samples showed Al enrichment as a thin  $\text{Al}_2\text{O}_3$  layer at the coating surface, which had also been found out by Lee and Fan to assist in retarding zinc evaporation during annealing in ambient air [6].

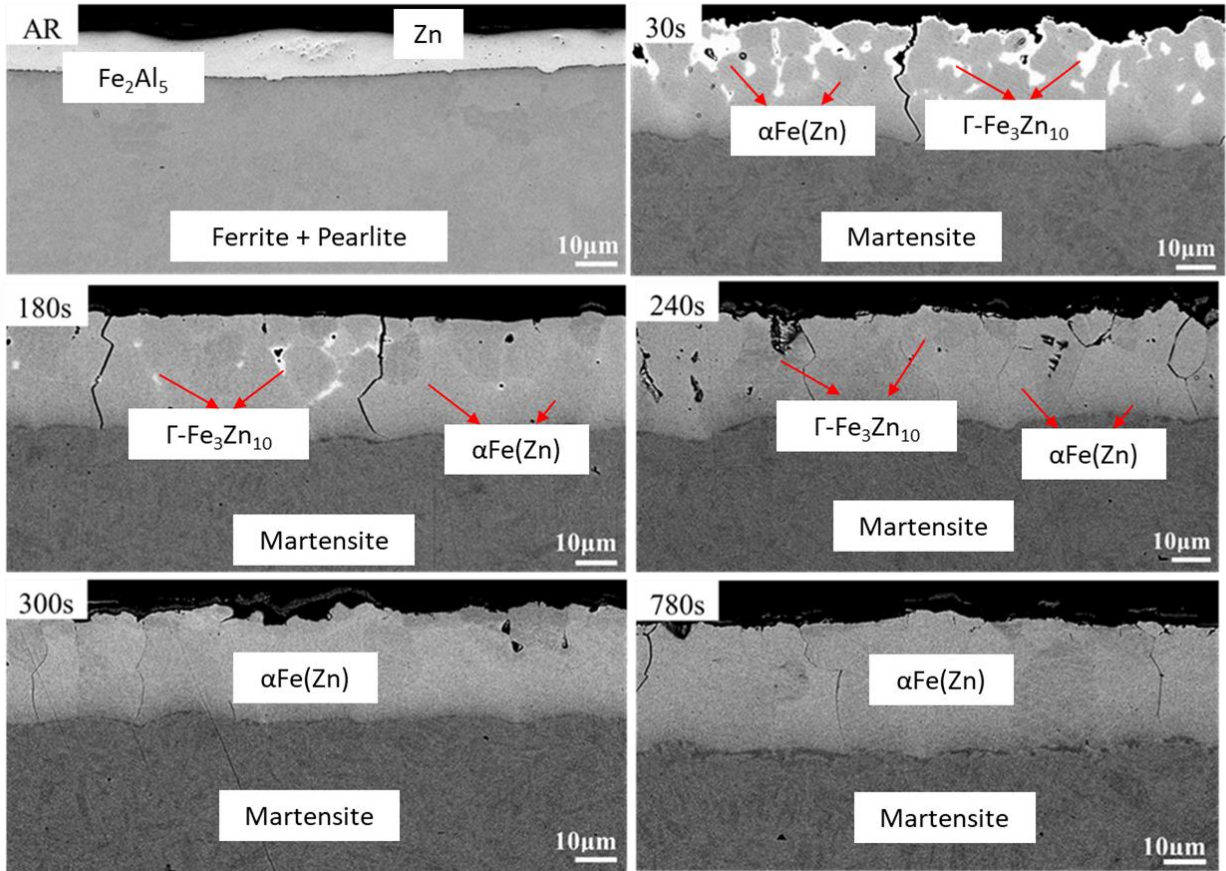


Figure 5. 6: BEI-SEM micrographs GI70 samples in the as-received (AR) condition, and annealed at 900°C for 30 s, 180s, 240s, 300s, and 780s and die-quenched.

Figure 5.7 a shows squared coating thickness ( $X^2$ ) of the as-quenched (compressed air and die-quenched) samples as a function of all annealing times starting from 240s to 780s, in those that the coating consisted of only  $\alpha$ -Fe(Zn). From Figure 5.7, it can be seen that the squared coating thickness ( $X^2$ ) increased linearly as a function of holding time (t) which demonstrated that the  $\alpha$ -Fe(Zn) phase grew by diffusion. Likewise, Figure 5.7 b shows zinc concentration (at%) as a function of coating interface distance ( $\mu\text{m}$ ) to the top surface. It is clear that by increasing the annealing time, zinc concentration decreased for both coating constituents  $\Gamma$ -Fe<sub>3</sub>Zn<sub>10</sub> and  $\alpha$ -

Fe(Zn) while the interface was shifting towards the substrate. It can be seen that the final thickness of the coating increased by increasing annealing time.

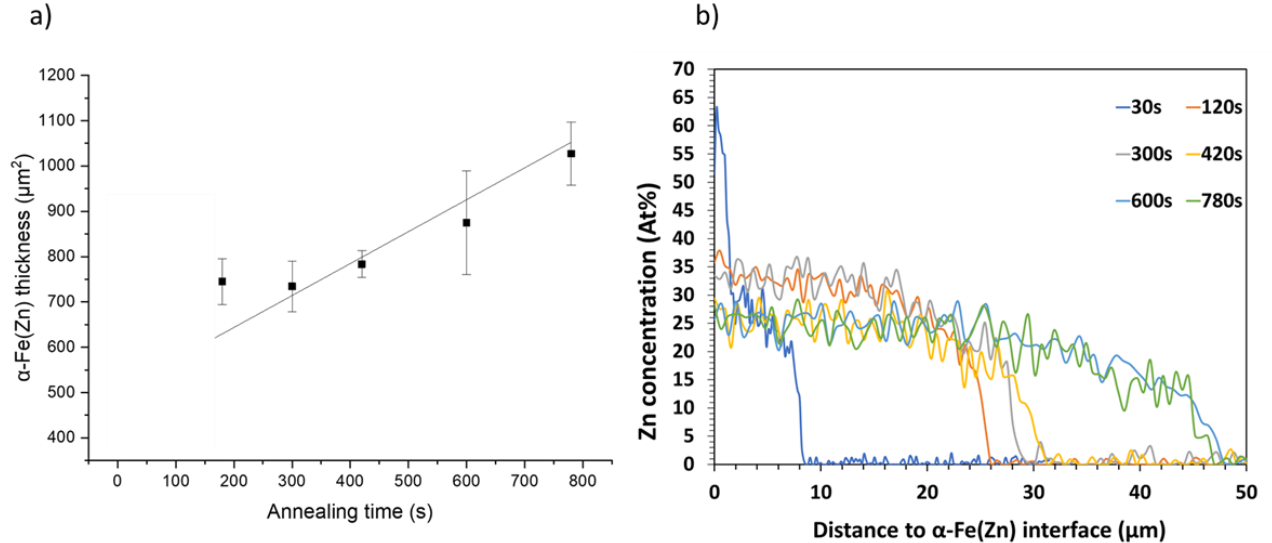


Figure 5. 7: a) Squared coating thickness as a function of annealing time (240s to 780s), and b) zinc concentration (at%) as a function of the distance of the coating-substrate interface to top surface, GI70 samples annealed at 900°C for all the annealing times, as-quenched in compressed air condition.

### 5.3 XRD Analysis of the Coating Microstructural Evolution After Heat Treatment and Cooling Processes

Figure 5.8 illustrates XRD results of the as-quenched (compressed gas and water-cooled planar dies) samples annealed at 900°C for all the annealing times (from 30 s to 780s). XRD confirmed the trends from the SEM data that longer annealing times result in higher  $\alpha$ -Fe(Zn) and lower  $\Gamma$ -Fe<sub>3</sub>Zn<sub>10</sub> contents. The general trends of the XRD result also showed a diffusion-controlled system.

Again, due to the higher cooling rate in die-quenched compared to compressed gas quenched process, a higher  $\Gamma$ -Fe<sub>3</sub>Zn<sub>10</sub> phase ratio was observed for these samples. The reason was because of less time for Zn diffusion in the planar die-quenched samples, more of  $\Gamma$ -Fe<sub>3</sub>Zn<sub>10</sub> was observed. Additionally, it was clearly observed zinc oxide (ZnO) slightly increased by increasing annealing time. The presence of ZnO was essential because it suppressed further Zn evaporation [6].

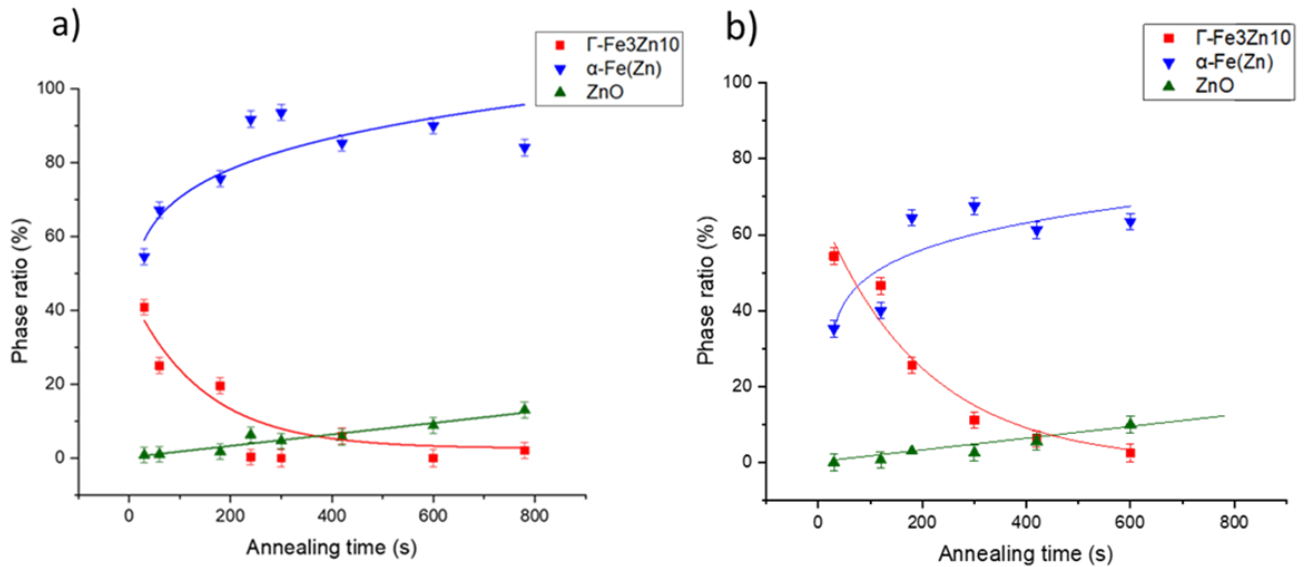


Figure 5. 8: Phase ratio of a) compressed gas quenched b) water-cooled planar die-quenched GI70 samples annealed at 900°C for all the annealing times.

## 5.4 Tensile Tested Samples

Uniaxial tensile testing was performed on both the planar and U-shaped die-quenched Zn-coated 22MnB5 steel samples annealed at 900°C for varying times. Tensile testing was performed on the planar die-quenched samples, the top surface (region 1) and the outer wall (region 4) of U-shaped die-quenched DHPF coated samples. The first purpose was to determine if the ultimate tensile

strength of the coated DHPF steels complied with the industrial target properties. The second purpose was to observe the influence of annealing time on the UTS of the substrates. In the previous literature, it has been pointed out that all 22MnB5 substrates with different annealing times met the target properties of  $\sigma_{(UTS)} \geq 150$  MPa with total elongation of approximately 7-9% [51]. Figure 5.9 shows summative plot of  $\sigma_{(UTS)}$  as a function of varying annealing times at 900°C for the planar and U-shaped die-quenched Zn-coated steel samples. Unlike the bare 22MnB5 substrates, tensile results obtained from the planar die and U-shaped DHPF coated samples revealed that as the annealing time increased, the UTS decreased until it no longer met the target UTS of at least 1500 MPa after annealing for 300s. All these three different tensile samples had similar properties in terms of UTS and total elongation.

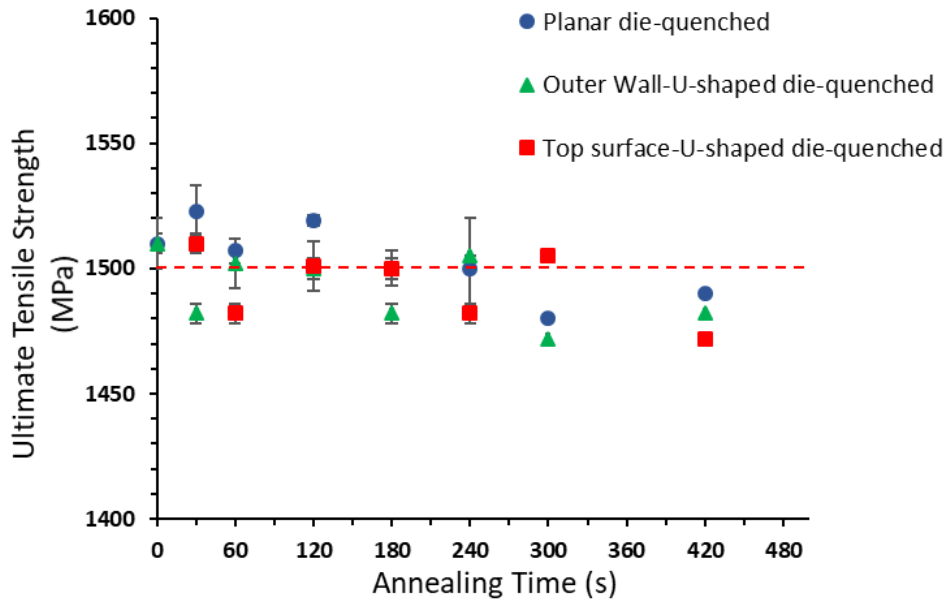


Figure 5. 9: Summative plot of  $\sigma_{(UTS)}$  as a function of all varying annealing times at 900°C for the planar and U-shaped die-quenched Zn-coated 22MnB5 steel samples.

## 5.5 SEM Analysis of As-Quenched and Tensile Tested Samples

In order to precisely determine the zinc distribution and degree of zinc penetration into the substrate, two sets of samples were examined. The first set of samples were annealed for 30 s (the shortest time) and 780s (the longest time) and planar die-quenched while the second set comprised tensile specimens from the 30 s and the 780s annealing times which were pulled to failure. A summary of the samples is shown in Table 5.1. The samples will be referenced with the labels indicated in Table 5.1 from now on.

Table 5. 1. Details on the examined samples for zinc distribution using EM techniques.

Material	Annealing time (s) at 900°C	Production history after annealing	Final coating microstructure
30AQ	30	as-quenched by water-cooled planar dies	$\alpha$ -Fe(Zn) + $\Gamma$ -Fe <sub>3</sub> Zn <sub>10</sub>
780AQ	780		$\alpha$ -Fe(Zn)
30TS	30	as-quenched by water-cooled planar dies followed by uniaxial tensile testing	$\alpha$ -Fe(Zn) + $\Gamma$ -Fe <sub>3</sub> Zn <sub>10</sub>
780TS	780		$\alpha$ -Fe(Zn)

The coating microstructural constituents and the diffusion depth of zinc for the longest (780s) and the shortest (30 s) annealing time were two critical reasons for performing further investigations on them. As specified in the previous paragraph, four samples were selected to undergo examination by a combination of the electron microscopy techniques. Figure 5.10 shows BSE images on the cross-sections of the 30AQ, 30TS, 780AQ, and 780TS samples, respectively. After tensile testing, the 30TS and 780TS samples, both exhibited crack formation and few of

them with a slight propagation into the substrate. Before tensile testing, on 30AQ and 780AQ samples, micro-cracks were not present. The presence of a few cracks in the as-quenched samples before tensile testing was probably due to the applied compressive load (350 kPa) during the die-quenching process. It should be noted that the cross-sections of the tensile tested samples were selected from the uniform elongation portion on the gauge length. Additionally, Figure 5.10 indicates that the tip of the micro-crack in the PAGB region appeared sharper for the samples with the shortest annealing time (30 s) whereas for 780s annealing time, the micro-crack tip was more blunted. According to the micro-cracking mechanism, it can be concluded that the sharpness or the bluntness of the micro-crack was dependent on the amount of zinc in the  $\alpha$ -Fe(Zn) thin layer at the crack tip region in the PAGB. Relatively, Janik et al. observed that the appearance and the penetration depth of cracking in Zn-coated 22MnB5 DHPF relied on the amount of embrittler atoms feeding the crack [46].

Figure 5.11 depicts micro-crack formation close to the fracture surface in the necking region where stress triaxiality occurred. The penetration of micro-cracks into the substrate close to the fracture was in excess of 15  $\mu\text{m}$ . For the purpose of a precise and easily-constrained micro-crack study, cracks were selected from the gauge length areas where uniform elongation had occurred. Once the micro-cracking mechanism is recognized, it can be applied to triaxial tensile testing

regions.

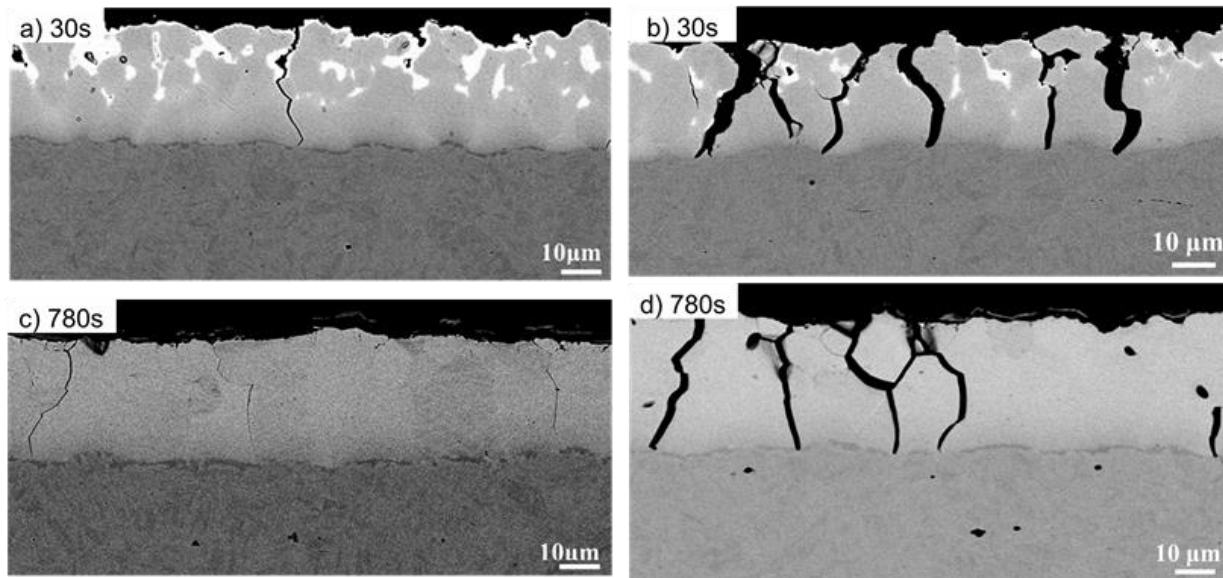


Figure 5. 10: BEI-SEM micrographs of (a,c) as-quenched and (b,d) after tensile testing GI70 samples annealed at 900°C for 30 s and 780s, and subsequently quenched by water-cooled planar dies.

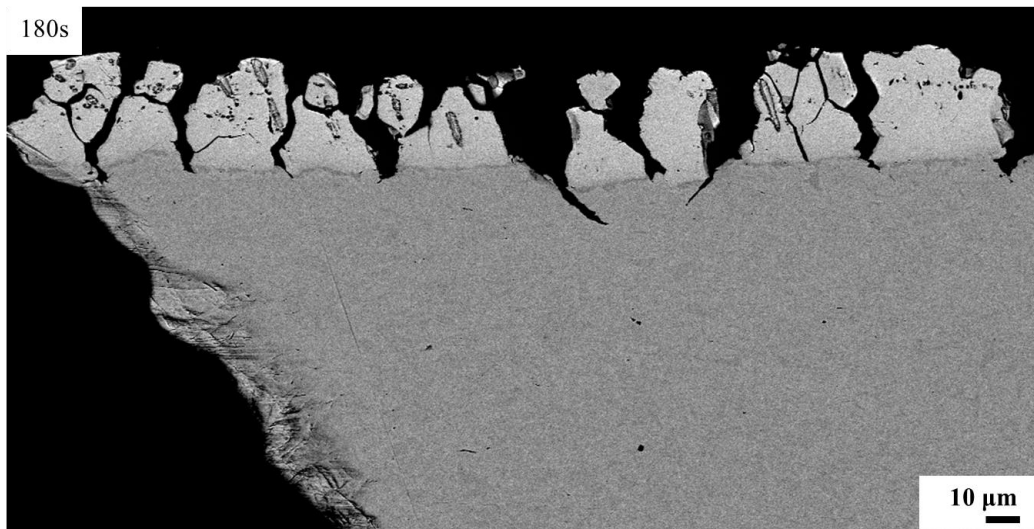


Figure 5. 11: Cross-sectional view on the fracture surfaces of a die-quenched Zn-coated sample annealed at 900°C for 180s.

The primary purpose of the EBSD application was to establish a phase map and to identify the coincident grain boundaries in between the grain boundaries of  $\alpha$ -Fe(Zn) and the PAGBs in 30 s and 780s as-quenched samples. EBSD maps were acquired from all the samples in Table 5.1.

## 5.6 EBSD Analysis on As-Quenched Samples

Figure 5.12 shows EBSD phase maps of the 30AQ (Figure 5.12 a) and 780AQ samples (Figure 5.12 b), respectively. The 30AQ EBSD phase map confirmed  $\Gamma$ -Fe<sub>3</sub>Zn<sub>10</sub> in between  $\alpha$ -Fe(Zn) grains within the coating (total thickness of  $\sim 26 \mu\text{m}$ ). The 780AQ EBSD phase map shows a thicker coating ( $\sim 37 \mu\text{m}$ ) comprised of only  $\alpha$ -Fe(Zn) phase. The  $\alpha$ -Fe(Zn) grain size had clearly increased to  $30 \mu\text{m}$  in length x  $20 \mu\text{m}$  in width for the longest annealing time (780s) compared to the shortest annealing time (30 s) which was  $13 \mu\text{m}$  in length x  $10 \mu\text{m}$  in width. As it was shown in Figure 5.8, the main oxide, ZnO, phase fraction increased with increasing the annealing time. For the longest annealing time (780s), the outermost layer was ZnO with a thickness of 2-4  $\mu\text{m}$ . Since this oxide layer was quite thin for the shorter annealing times, it was not detected on the EBSD maps. A fully martensitic substrate was observed in all EBSD maps.

A diffusion zone was observed in between the coating and the steel matrix on the EBSD maps of the samples (Figure 5.12). This zone had a plate-like morphology rather than the typical lath morphology of the bare substrate. It represented zinc-enriched martensite region created from the zinc-enriched austenite which arised from Zn diffusion after being die-quenched.

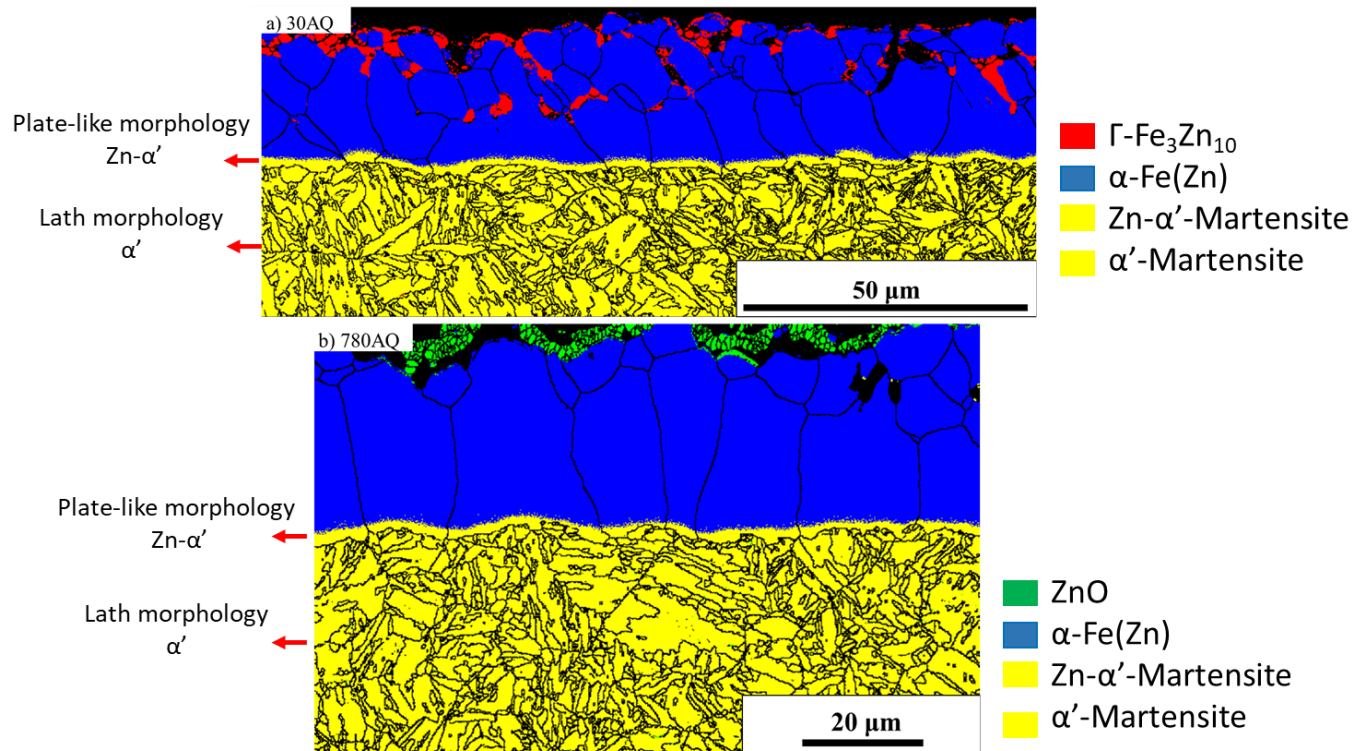


Figure 5. 12: EBSD phase maps of as-quenched after tensile testing samples, annealed at 900°C for a) 30 s and b) 780s.

## 5.7 EBSD Analysis on As-Quenched Samples After Tensile Testing

Figure 5.13 shows phase maps and Euler maps of the 30TS and 780TS samples, respectively. The EBSD maps of the samples shown in Figure 5.12 after tensile testing were similar to the maps of the samples prior to tensile testing. The only difference was the presence of cracks that had formed along the  $\alpha$ -Fe(Zn) grain boundaries and penetrated into the martensitic substrate.

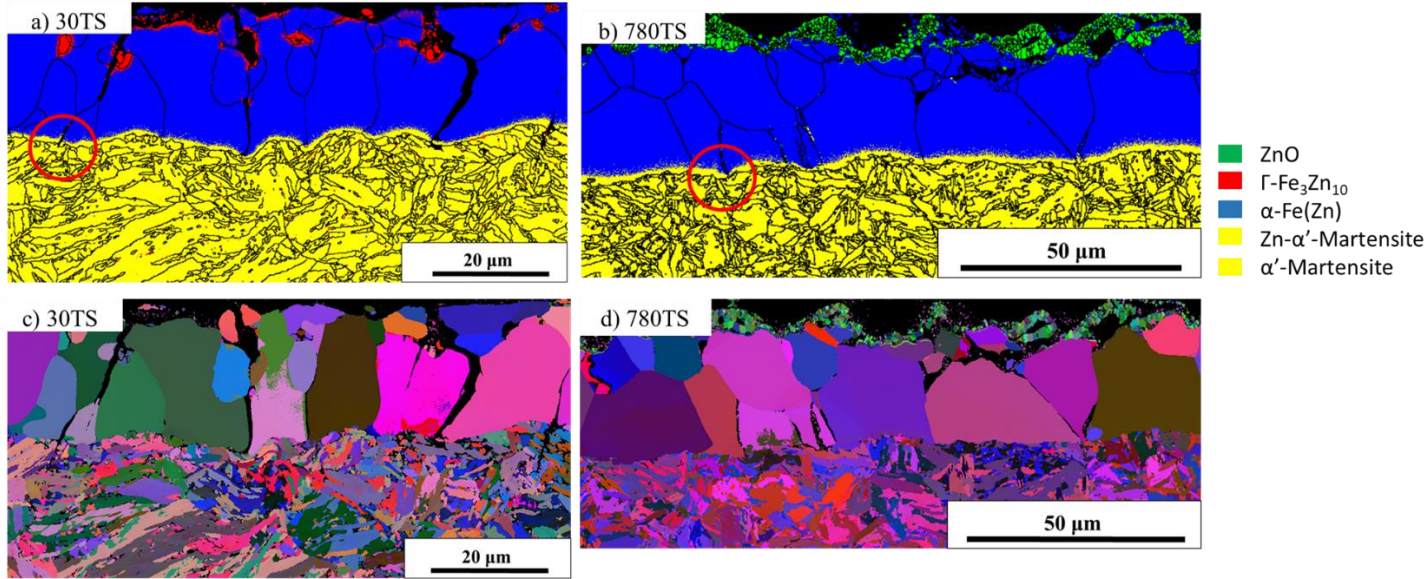


Figure 5. 13: a,b) EBSD phase maps, c,d) EBSD Euler maps after tensile testing for samples annealed at 900°C for 30 s and 780s - Noted that micro-cracks on the samples are highlighted with a red circle on the EBSD phase maps.

Considering the EBSD maps of before and after tensile testing and micro-crack formation (Figure 5.12 and 5.13), cracks initiated and propagated into the substrate through the GBs independent of grain misorientation relationships. In the coating, intergranular cracks were coincidentally formed in between the grains, regardless of the angle of the grain boundary (as observed from the Euler map). This point demonstrated that crack formation appeared to be independent of grain misorientation and likely dependent on the zinc concentration in these areas.

## 5.8 Prior Austenite Grain Boundary Detection

A Python computer program written by Cyril Cayron called “APRGE” was employed to detect the PAGBs [55]. This software automatically reconstructs the prior austenite grain boundaries within

different materials such as steels. It uses the phase transformation data including point groups, orientation relationships, and the groupoid composition table generated by the computer program GenOVa [55]. Besides the theoretical data, the program needed the experimental EBSD maps acquired by the HKL software from the EBSD detector. APRGE EBSD map reconstruction occurred in two main steps. First, the program compared the Euler angles of the grains leading to proposed pre-grains. Once the orientation of the neighboring pre-grains was close to the theoretical misorientation database for a parent grain, it specified them as daughter grains within one parent grain. Secondly, the composition of these neighboring daughter grains was compared with the groupoid composition table in order to identify each prior austenite grain. After uploading the EBSD map data into the program, each austenite grain was coded by a color indicating its corresponding Euler angle [55]. Figure 5.14 shows an example of APRGE austenite grain reconstruction on the die-quenched Zn-coated sample annealed at 900°C for 780s. Therefore, PAGB reconstruction was performed by this software on EBSD maps as a precursor to STEM-EELS analysis on the grain boundaries.

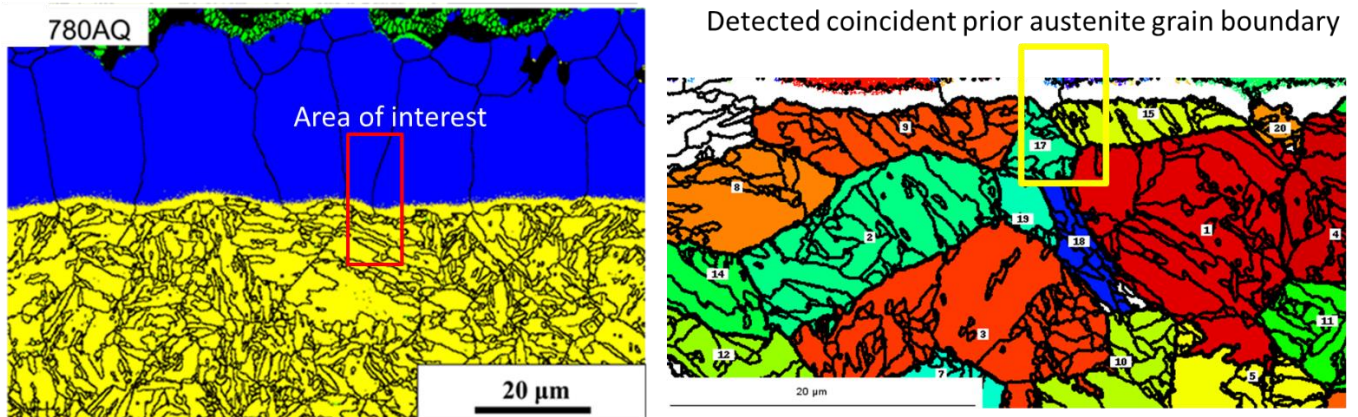


Figure 5. 14: APRGE austenite grain reconstruction on the die-quenched Zn-coated sample annealed at 900°C for 780s.

## 5.9 STEM-EELS Analysis on GBs Before Tensile Testing

Figure 5.15 and 5.16 show Zn and Fe EELS maps along a GB of the coating and a PAGB of the substrate of 30AQ and 780AQ samples, respectively. It shows the role of the grain boundary in zinc diffusion along the GBs and the PAGBs in each layer. Zn EELS maps of 30AQ and 780AQ samples, before tensile testing, showed that the grain boundary of the  $\alpha$ -Fe(Zn) coating was enriched with zinc. The Zn content along the PAGBs of both samples was enriched. Although the Zn EELS map for the 30AQ sample showed that some of the Zn had diffused into the Zn-enriched martensite layer, it still showed zinc enrichment in the PAGB (Figure 5.15).

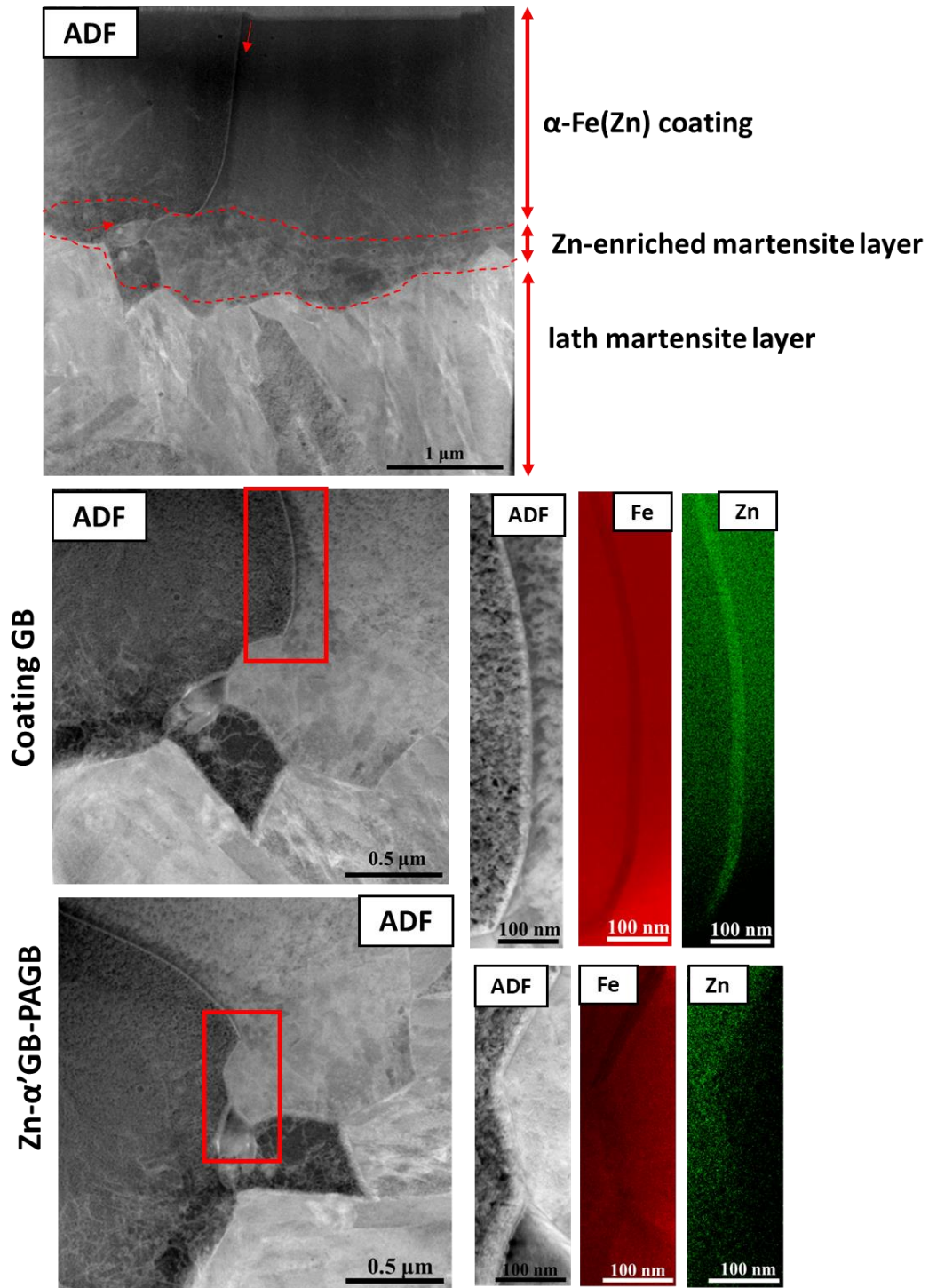


Figure 5. 15: STEM ADF images and EELS maps of the GB in the coating and substrate from a 30AQ sample.

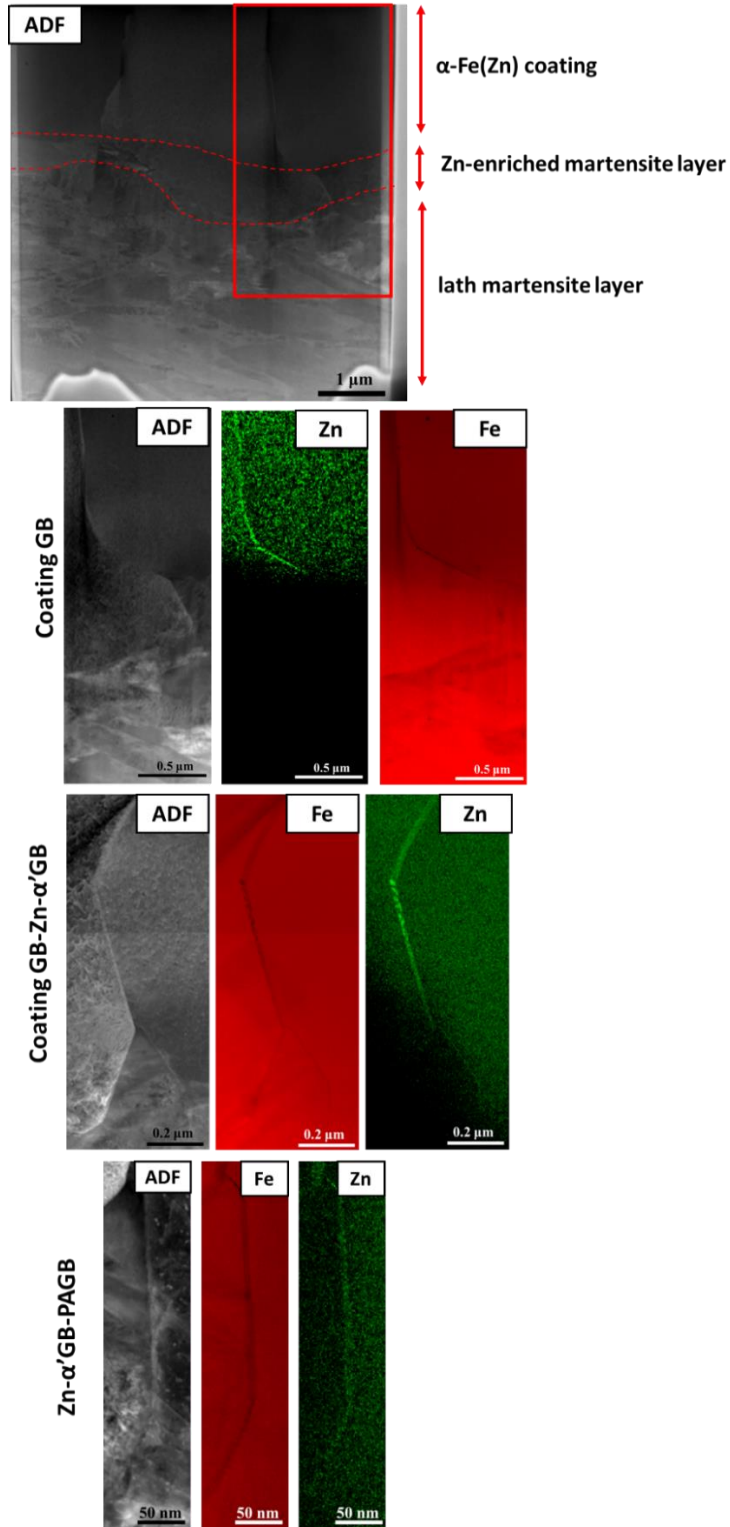


Figure 5. 16: STEM ADF images and EELS maps of the GB in the coating and substrate from a

780AQ sample.

Figure 5.17 shows the corresponding zinc distribution profile (generated by the GMS3 software) for the PAGB Zn EELS map and the coating GB Zn EELS map for the 780AQ sample. EELS semi-quantitative analysis showed that the zinc concentration in the coincident  $\alpha$ -Fe(Zn) GBs was 20 at% and, in the PAGBs, was 10-12 at% higher than that observed in the matrix. It should be noted that the same result was observed for 30AQ sample.

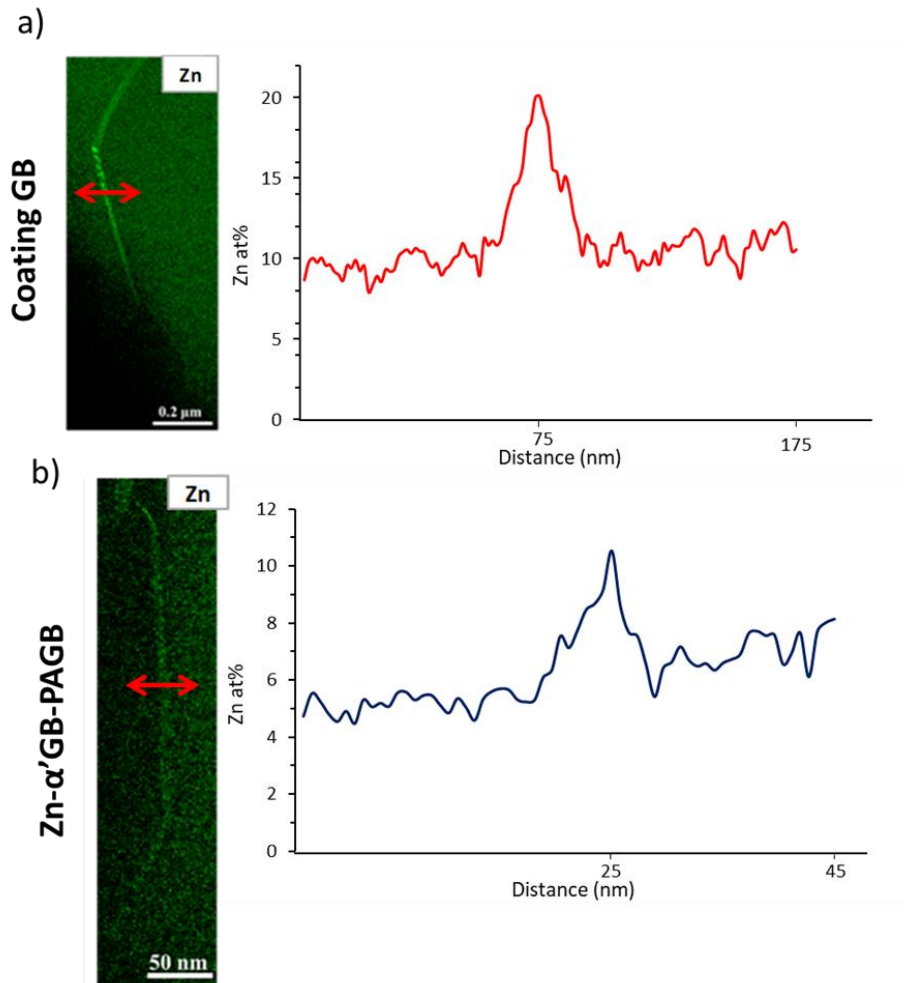


Figure 5. 17: Zinc distribution profile to a) the coating GB and b) the PAGB Zn EELS map Zn EELS map for a 780AQ sample.

Despite the decrease in average zinc concentration in the coating caused by increasing the annealing time, Zn EELS maps show zinc enrichment within both  $\alpha$ -Fe(Zn) grain boundaries and PAGBs for the 780s and 30 s annealing times.

## **5.10 STEM-EELS Analysis on GBs after Tensile Testing and Formation of Micro-Cracks**

Figure 5.18 shows EELS maps of the Zn, Fe, and O distribution inside the crack (Figure 5.18 a) and at the tip of the micro-crack region (Figure 5.18 b) for a 30TS sample. Figure 5.19 shows EELS maps of the Zn, Fe, and O distribution inside the crack (Figure 5.19 a) and at the tip of the micro-crack (Figure 5.19 b) for a 780TS sample. The EELS maps of the micro-crack tips which had entered the PAGB region also confirmed zinc enrichment. When Zn enrichment stopped, blunting of the crack tip was observed. This is evidence that the Zn presence was a necessary ingredient for crack propagation. This observation is unique since the origin of micro-cracking was not linked to the observation of LME. Therefore, solid-state diffusion of zinc played an important role in this observation.

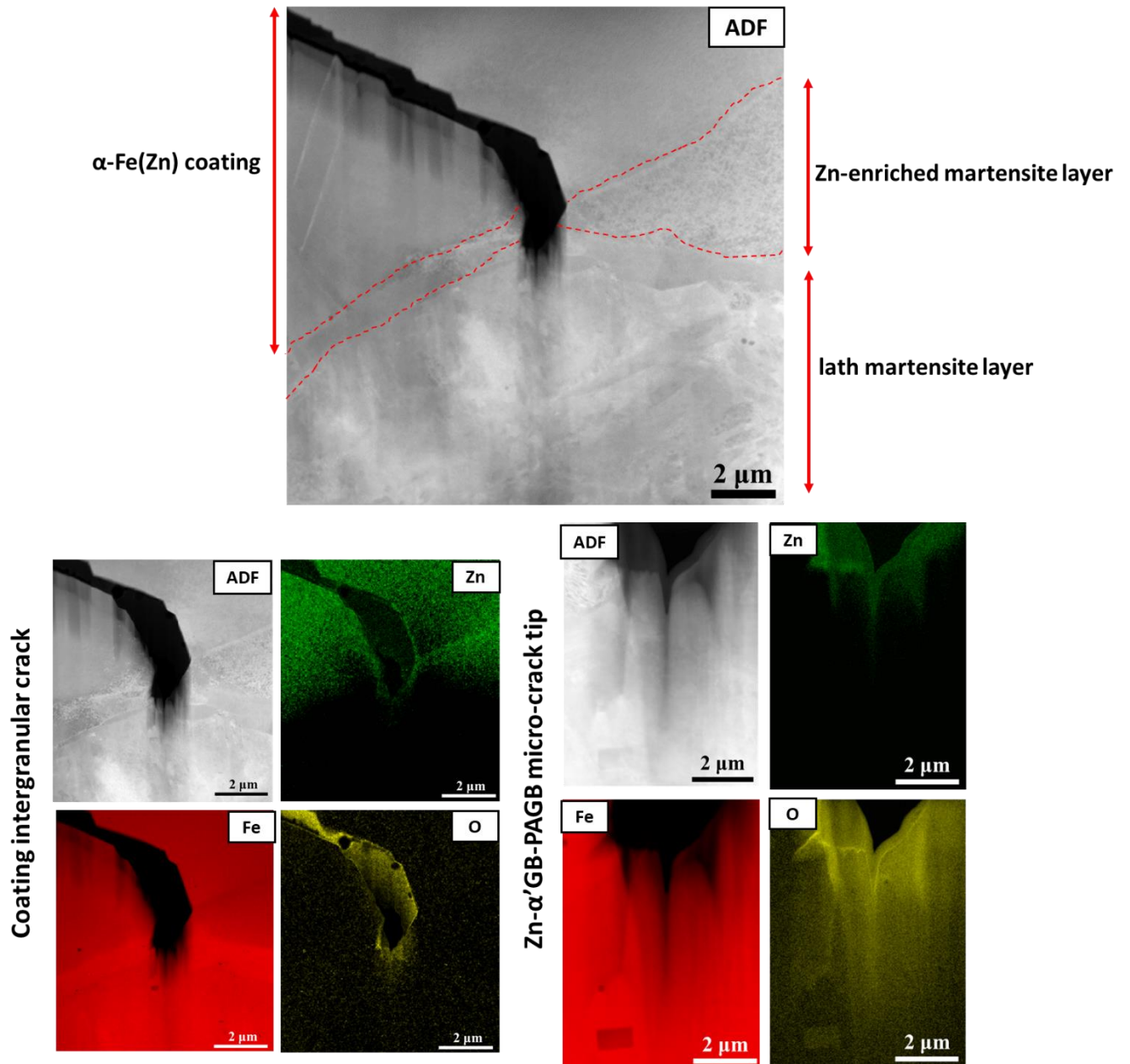


Figure 5. 18: STEM ADF images and EELS maps of 30TS, along the crack, and the micro-crack tip.

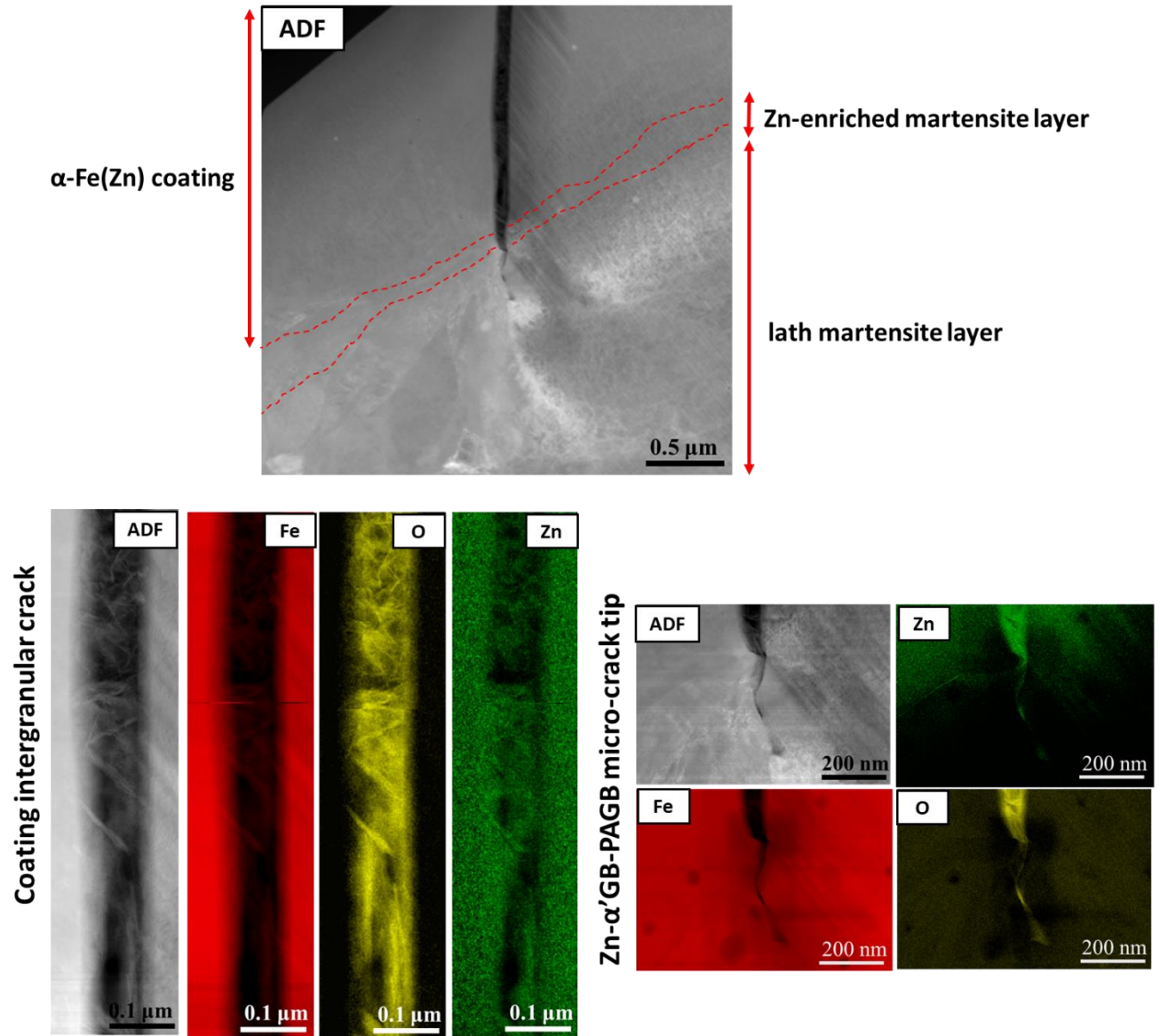


Figure 5. 19: STEM ADF images and EELS maps of 780TS, along the crack, and the micro- crack tip.

## **5.11 SEM and EDS Analysis on the Coating Microstructural Evolution for U-Shaped Die-Quenched Samples**

During U-shaped die-quenching the material either underwent tension, compression, bending, or a combination of forces. The level of the strain on the sample depends on the area of the U-shaped die. Lee and De Cooman reported that each region on the sample after the U-shaped press forming process underwent a certain level of strain [5]. Figure 5.20 shows a schematic diagram of different areas on a Zn-coated PHS U-shaped die-quenched labeled from 1 to 7 [5]. Table 5.2 describes the imposed strain for each region on the sample after the U-shaped press forming process [5]. The top surface (1) was not deformed during the process, therefore, no cracking was expected to be seen. The top inner corner (3) and bottom outer corner (6) underwent compressing bending which was not likely to create micro-cracks. These two areas first experienced bending and a subsequent compression load which likely closed any cracks. The top outer corner (2) and bottom inner corner (7), an opposite condition of regions 3 and 6, underwent tension bending deformation. Furthermore, applied tension on the U-shaped part is likely to open intergranular crack propagating from the coating into the steel substrate.

Another region where micro-cracking took place on the U-shaped sample was the outer wall (4). This area (area 4) had deformed by a mixture of compression bending followed by tension unbending. This condition resulted in micro-crack propagation into the PAGBs of the substrate as observed in previous literature [5]. Meanwhile, the inner wall of the same region (5) was only subjected to shear friction of the die which led to minor crack formation.

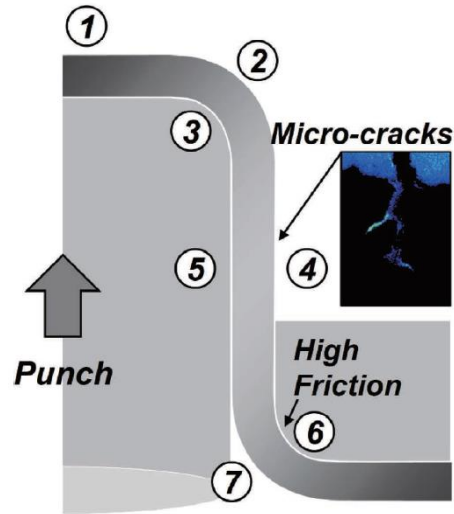


Figure 5. 20: Schematic of a cross-sectional view of U-shaped die-quenched of Zn-coated PHS [5].

Table 5. 2. Detailed conditions of each region on U-shaped sample after press forming process [5].

Site number	Condition	Description
1	No deformation	Uniform coating without cracks
2	Tension bending	Stretch bending causing crack formation
3	Compression bending	Uniform coating without cracks
4	Tension + Unbending	Crack formation
5	Die friction	Few shallow cracks

6	Compression bending	Uniform coating without cracks
7	Tension bending	Stretch bending causing crack formation

Figure 5.21 and 5.22 show BSE images and their corresponding EDS Zn elemental distribution of the Zn-coated U-shaped PHS annealed at 900°C for 30 s and 780s for the areas defined in Figure 5.20. As specified earlier, areas 2,7 and 4 in both cases (Figure 5.21 and Figure 5.22) displayed crack formation due to tension bending and/or tension plus die friction. Respectively, the DIC strain profiles (Figure 4.6) also demonstrated that first the outer wall and then the top outer and/or bottom inner corner were under the higher amount of strain, 8 to 10%. Whereas the other areas such as 3,6 and 5 did not show crack formation in the coating as they underwent either compression or no deformation (Figure 5.21 and Figure 5.22). Once more, it was observed that after 30 s annealing and subsequent U-shaped press hardening, the coating consisted of  $\alpha$ -Fe(Zn) +  $\Gamma$ -Fe<sub>3</sub>Zn<sub>10</sub> throughout the whole U-shaped sample. However, as expected, the same sample after 780s annealing was comprised of only  $\alpha$ -Fe(Zn) in the coating with a detectable ZnO layer on the top surface.

In order to determine the zinc concentration of the U-shaped PHS samples, two important areas from each sample (30 s and 780s) were chosen. One sample was from the top surface (area 1), where the sample had not undergone any significant deformation. This area was similar to the as-quenched samples prepared previously by planar die-quenching. Another selected area was from the outer wall (area 4), where the sample had experienced tension plus die friction leading

to a severe condition for micro-cracking. The procedure for observing the zinc concentration in these two areas was carried out in the same manner as for as-quenched samples and after tensile testing samples of planar die-quenched process (sections 5.5, 5.6, 5.7, 5.9 and 5.10). Therefore, GBs and PAGBs from the area 1, and micro-cracks from the area 4 of 30 s and 780s U-shaped samples (Table 5.3) were examined and analyzed using SEM-EBSD and STEM-EELS.

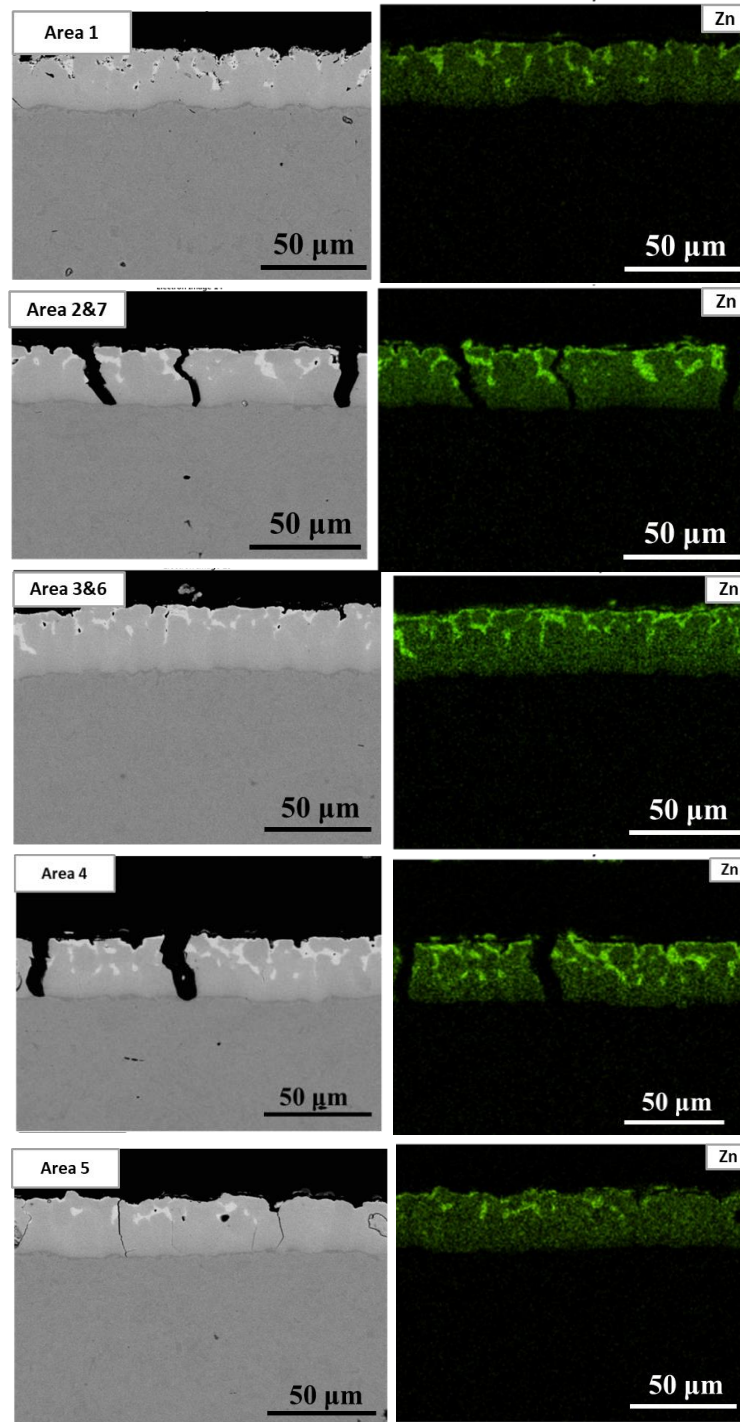


Figure 5. 21: BSE images and their corresponding EDS Zn elemental distribution of the U-shaped Zn-coated PHS sample annealed at 900°C for 30 s.

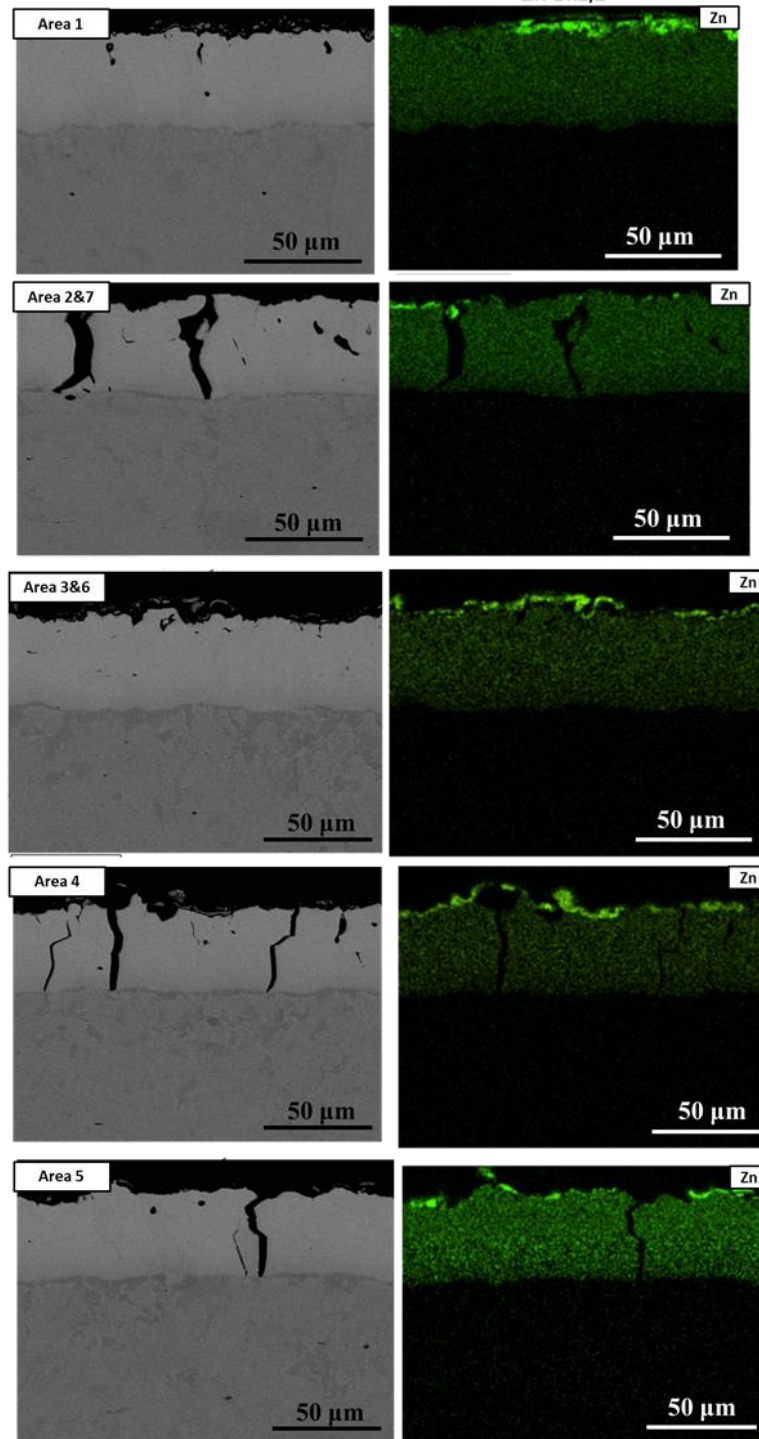


Figure 5. 22: BSE images and their corresponding EDS Zn elemental distribution of the U-shaped Zn-coated PHS sample annealed at 900°C for 780s.

Table 5. 3. Details on the examined U-shaped samples for zinc distribution using EM techniques.

Material	Annealing time (s) at 900°C	Production history after annealing		Final coating microstructure
30UR1	30	Press hardened by water-cooled U-shaped dies	Area 1	$\alpha$ -Fe(Zn) + $\Gamma$ -Fe <sub>3</sub> Zn <sub>10</sub>
780UR1	780			$\alpha$ -Fe(Zn)
30UR4	30		Area 4	$\alpha$ -Fe(Zn) + $\Gamma$ -Fe <sub>3</sub> Zn <sub>10</sub>
780UR4	780			$\alpha$ -Fe(Zn)

## 5.12 EBSD Analysis of U-Shaped Press Hardened Samples

Figure 5.23 shows EBSD phase maps of area 1 of the U-shaped samples annealed for 30 s and 780s at 900°C. It can be seen that EBSD map of this region was very similar to that of the as-quenched samples 30AQ and 780AQ (Figure 5.11 a,b). Therefore, it can be confirmed that this site was an ideal area of the U-shaped die to study PAGBs and GBs contribution to zinc solid-state diffusion, prior to micro-cracking.

In order to perform a precise measurement on the zinc distribution along a GB and a PAGB, as specified earlier, one area was chosen on each EBSD map of 30UR1 and 780UR1 (Figure 5.23). The prior austenite grain boundary of 30UR1 and 780UR1 samples was identified as specified in section 5.8. FIB milling was used to create TEM lift-out samples from an area that contained a coating grain boundary going through the  $\alpha$ -Fe(Zn)-Zn-enriched martensite interface and ultimately ending less than a micron deep into the substrate.

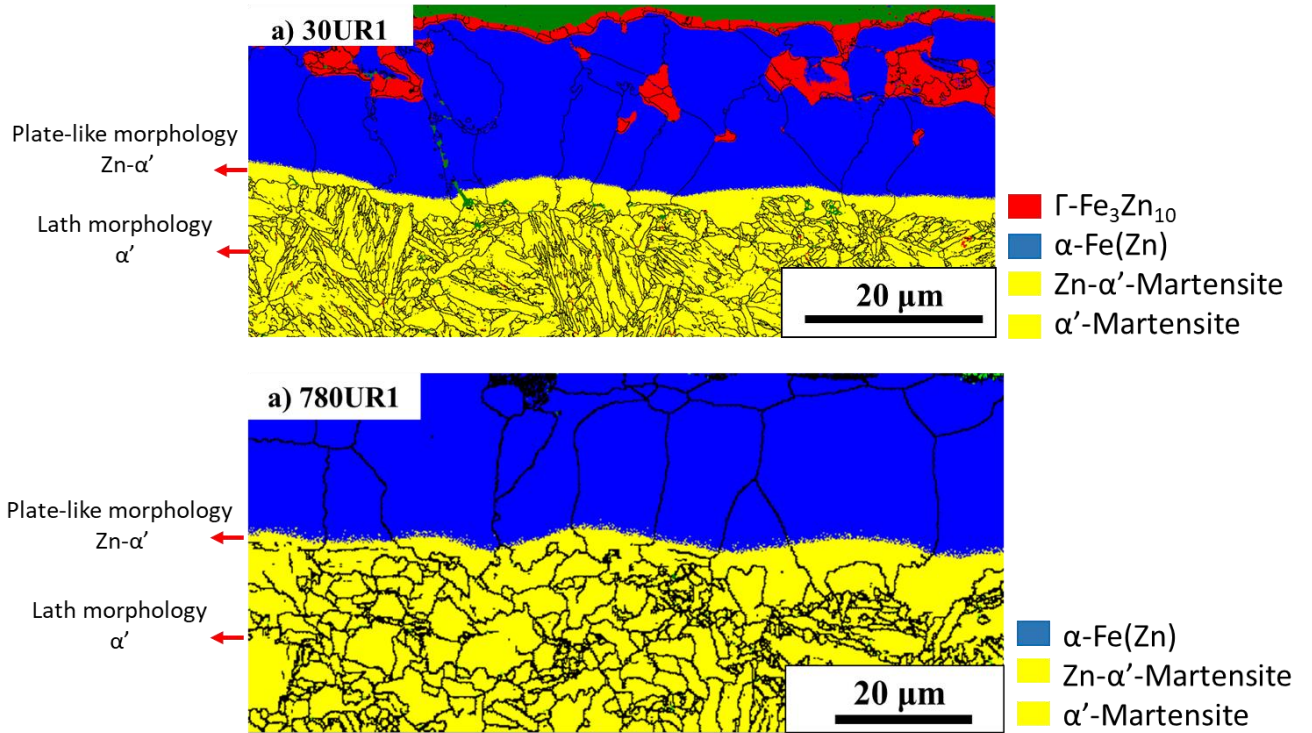


Figure 5. 23: EBSD phase maps of area 1 of the U-shaped samples annealed at 900°C for (a) 30 s and (b) 780s.

### 5.13 STEM-EELS Analysis on GBs of U-shaped Die-Quenched Samples

Figure 5.24 and 5.25 illustrate the Zn and Fe EELS maps on the extracted area taken from the 30UR1 and 780UR1 samples, respectively. It can be seen that the grain boundary of the coating was enriched with zinc as was the PAGB of both samples. This observation once more showed that diffusion of zinc along the GB and PAGB of the substrate occurred by solid-state diffusion whether the sample was composed of the two phase coating microstructure (30UR1,  $\alpha$ -Fe(Zn) +  $\Gamma$ -Fe<sub>3</sub>Zn<sub>10</sub>) or the single phase coating (780UR1,  $\alpha$ -Fe(Zn)).

To study U-shaped die-quenched sample micro-cracks, one crack from area 4 of 30 s and 780s annealed samples was chosen in order to extract in-plane FIB lift-outs. As mentioned before, area 4 of the U-shaped sample underwent a mixture of tension and die friction causing intergranular fracture. Area 4 of the U-shaped sample resembled the condition when planar die-quenched samples (30TS and 780TS) were pulled to fracture during tensile testing (Figure 5.11 c,d).

Figure 5.26 shows SAM-AES elemental mapping of a GI70 sample annealed at 900°C for 30 s. The planar die-quenched sample annealed for 30 s was used for this experiment to perform in-situ fracture testing under vacuum. The SAM-AES result for in-situ formed fracture surface for the 30 s as-quenched sample showed Zn-enrichment on the fracture surface in Zn-enriched martensite layer of the substrate.

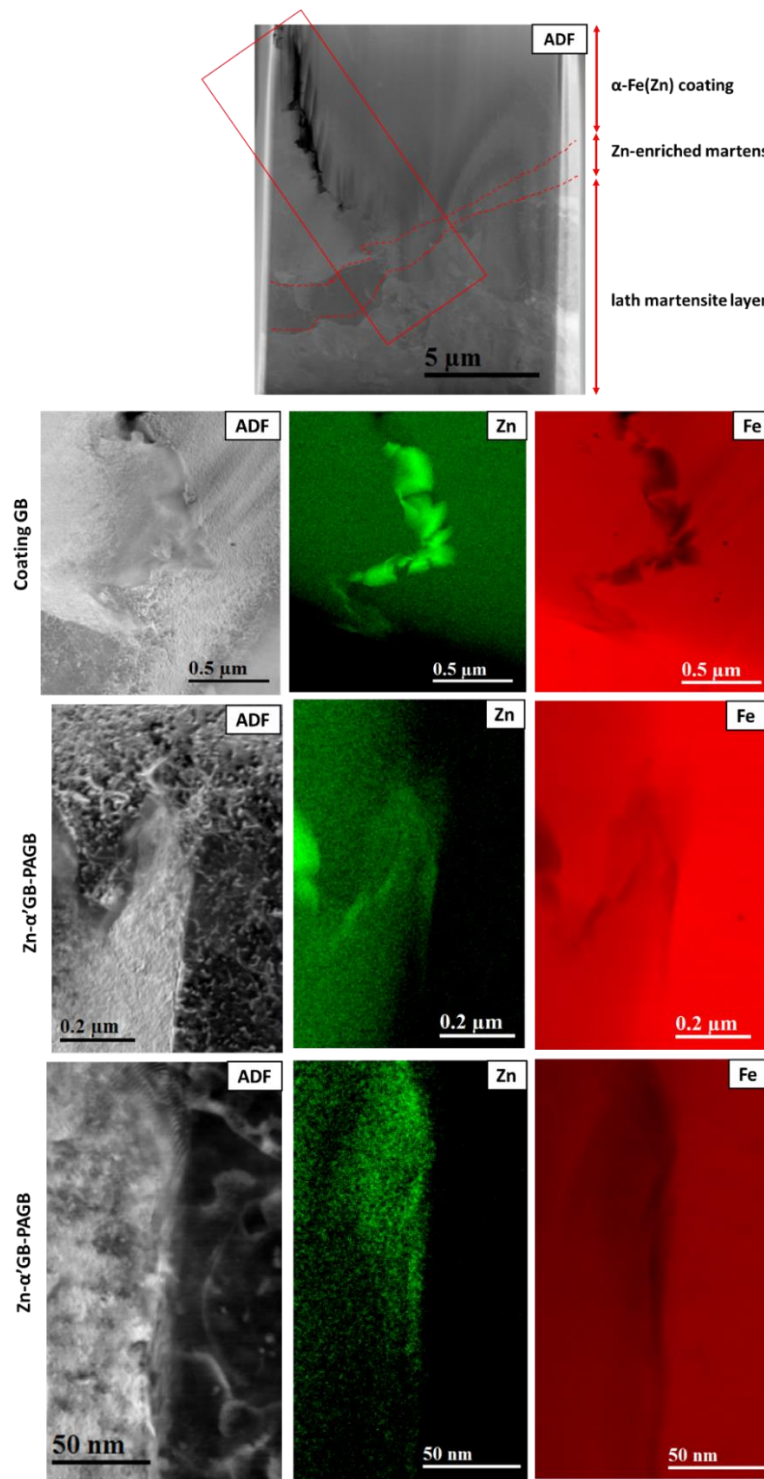


Figure 5. 24: STEM ADF images and EELS maps of the GB in the coating and PAGB in the substrate, 30UR1 sample.

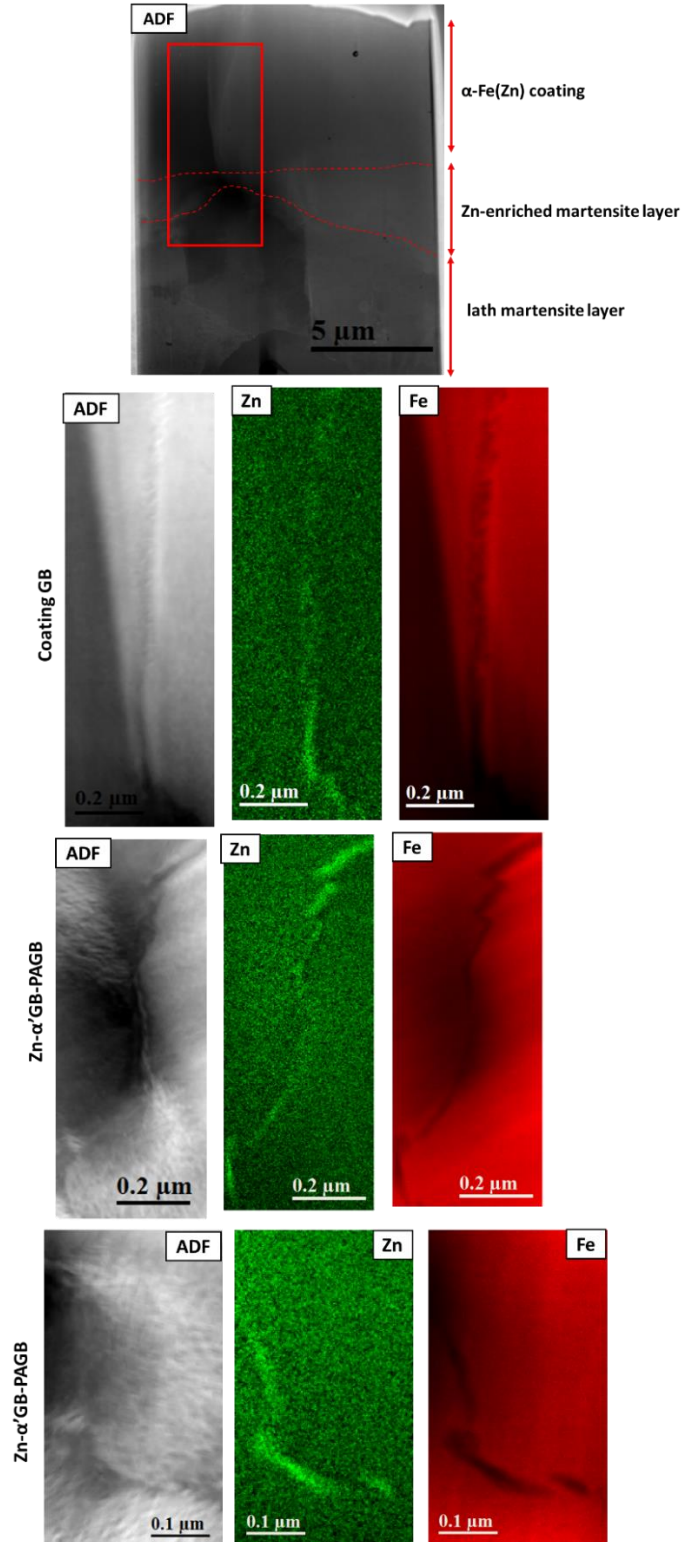


Figure 5. 25: STEM ADF images and EELS maps of the GB in the coating and PAGB in the substrate, 780UR1 sample.

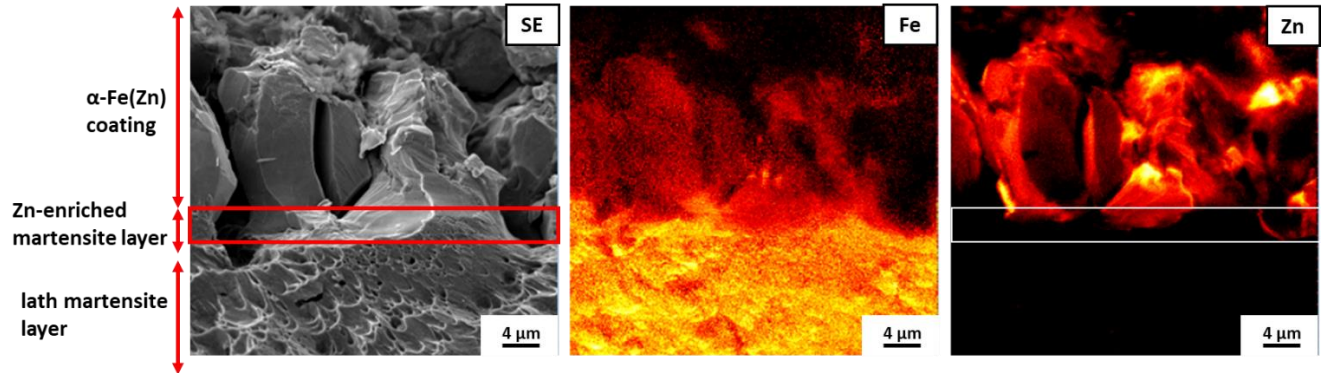


Figure 5. 26: Cross-sectional view SAM-AES map images of a GI70 sample annealed at 900°C for 30 s.

Figure 5.27 shows EELS maps of Zn, Fe, and O distribution inside the crack (Figure 5.27 a) and at the tip of the micro-crack region (Figure 5.27 b) for a 30UR4 sample. Also, Figure 5.28 shows EELS maps of Zn, Fe, and O distribution inside the crack (Figure 5.28 a) and at the tip of the micro-crack region (Figure 5.28 b) for a 780UR4 sample. Similar to the 30TS and 7807S samples, the 30UR4 and 780UR4 EELS maps of the crack tips which had entered the PAGB region also confirmed PAGB zinc enrichment. Therefore, the importance of intergranular zinc for crack propagation can be implied which also emphasized the role of the grain boundary diffusion of zinc. It can be seen that when the GB zinc enrichment had finished, blunting of the crack tip occurred. All the mentioned points clarified the importance of grain boundary diffusion and zinc enrichment being a key mechanism in micro-crack formation and propagation in Zn-coated press hardened steels.

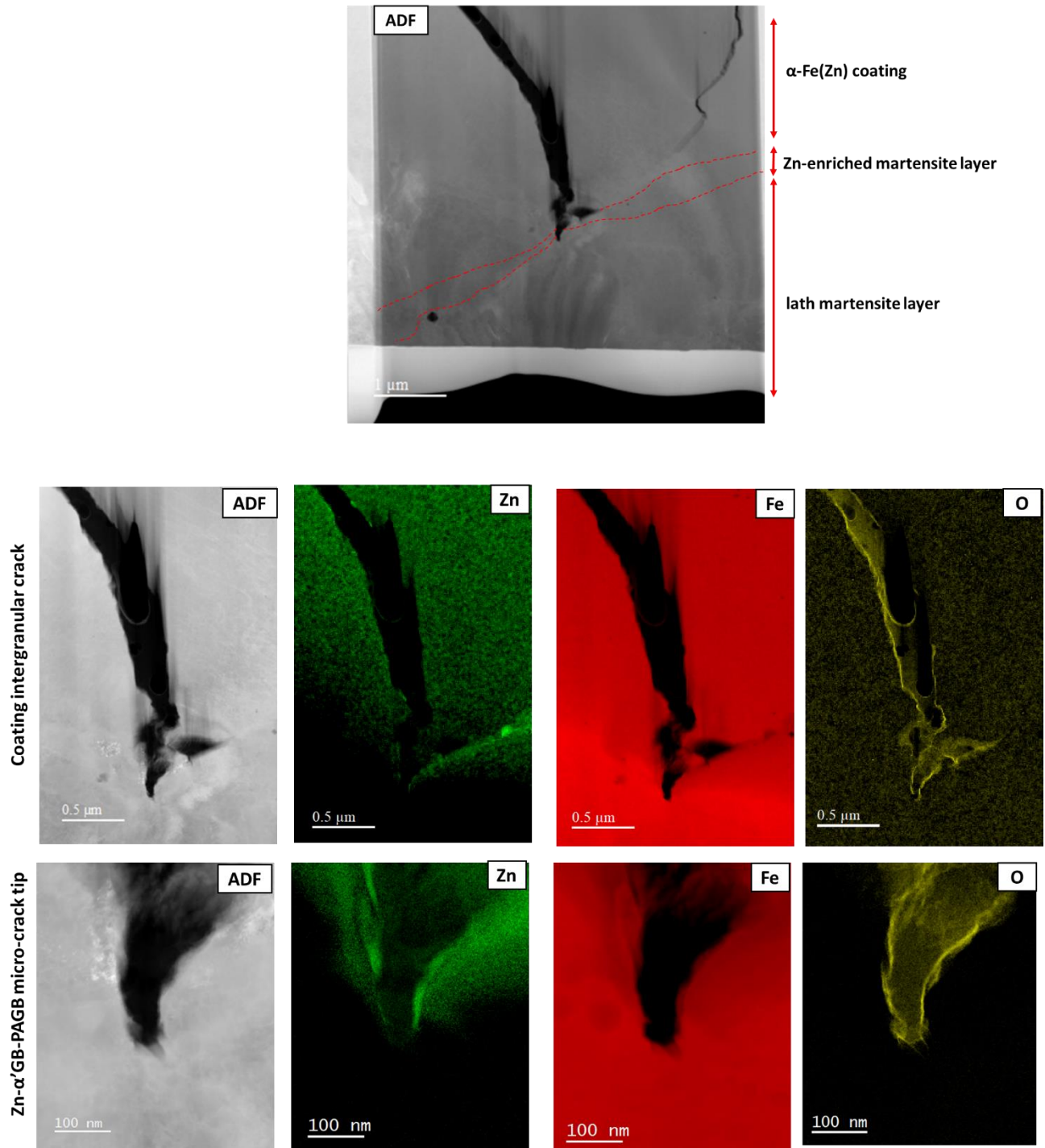


Figure 5. 27: STEM ADF images and EELS maps of 30UR4, along the crack and the micro-crack tip.

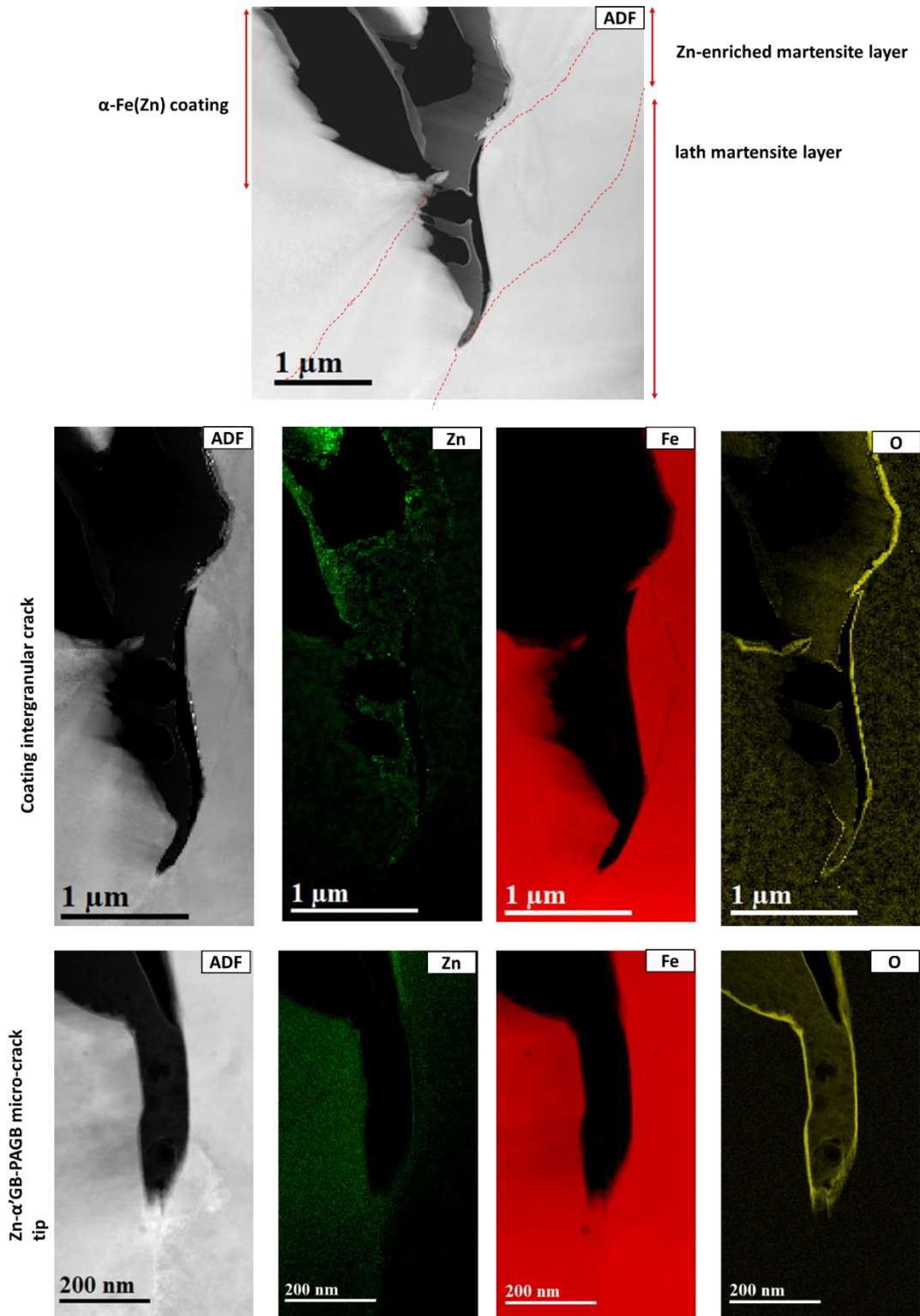


Figure 5. 28: STEM ADF images and EELS maps of 780UR4, along the crack and the micro-crack

tip.

## 6. Discussion

The origin of micro-cracking in GI70 coated 22MnB5 press hardened steel samples annealed at 900°C for a range of annealing times was determined. As a result of performing experiments at 900°C followed by a rapid die-quenching ( $\sim 100^\circ\text{Cs}^{-1}$ ) of the coating, zinc and iron started to interact with each other and consequently affected the diffusion depth of Zn into the (at that time) austenitic substrate and, thereby, the coating and the coating-substrate interfacial microstructural evolution. Simultaneously, the substrate, with an initial ferrite-pearlite microstructure, transformed into a fully lath martensitic ( $\alpha'$ ) microstructure because of the high cooling rate.

### 6.1 Coating Microstructural Evolution

The as-received (AR) GI70 22MnB5 samples consisted of a 10  $\mu\text{m}$  thick pure zinc coating with an interfacial intermetallic phase. EDS analysis on the AR GI70 22MnB5 samples (Figure 5.4) showed an Al-rich layer at the interface of coating-substrate which was indicative of the presence of the  $\text{Fe}_2\text{Al}_{5-x}\text{Zn}_x$  inhibition layer. However, during the heating process, this layer broke down and the Al migrated to the top surface where  $\text{Al}_2\text{O}_3$  formed, where it suppressed Zn oxidation and evaporation during the austenization annealing of the PHS [1, 6].

Figure 6.1 shows a schematic of the coating microstructural evolution as a function of temperature and annealing time for the GI70 22MnB5 DHPF samples. The phase configuration in the figure illustrates the formation of different Fe-Zn intermetallic phases by increasing the experimental temperature and eventually the annealing time, which is consistent with a diffusion

couple driven growth of the Fe-Zn intermetallic phases into the steel substrate [1, 46]. At 700°C, the coating was composed of only of  $\Gamma$ -Fe<sub>3</sub>Zn<sub>10</sub>, where it has been shown that prior to passing through the peritectic temperature at 782°C [1], the coating had completely transformed into  $\Gamma$ -Fe<sub>3</sub>Zn<sub>10</sub> with a thin diffusion driven layer of  $(\alpha$ -Fe)Zn below the liquid  $\Gamma$ -Fe<sub>3</sub>Zn<sub>10</sub> [51]. After reaching to 900°C, the liquid  $\Gamma$ -Fe<sub>3</sub>Zn<sub>10</sub> was being consumed in the formation of  $\alpha$ -Fe(Zn) and as a result of the inward diffusion of zinc, and after 30 s annealing time, the coating microstructure consisted of liquid  $\Gamma$ -Fe<sub>3</sub>Zn<sub>10</sub> and  $\alpha$ -Fe(Zn). After 780s annealing time at 900°C, the  $\alpha$ -Fe(Zn) continued to grow by Zn diffusion until no liquid was present.

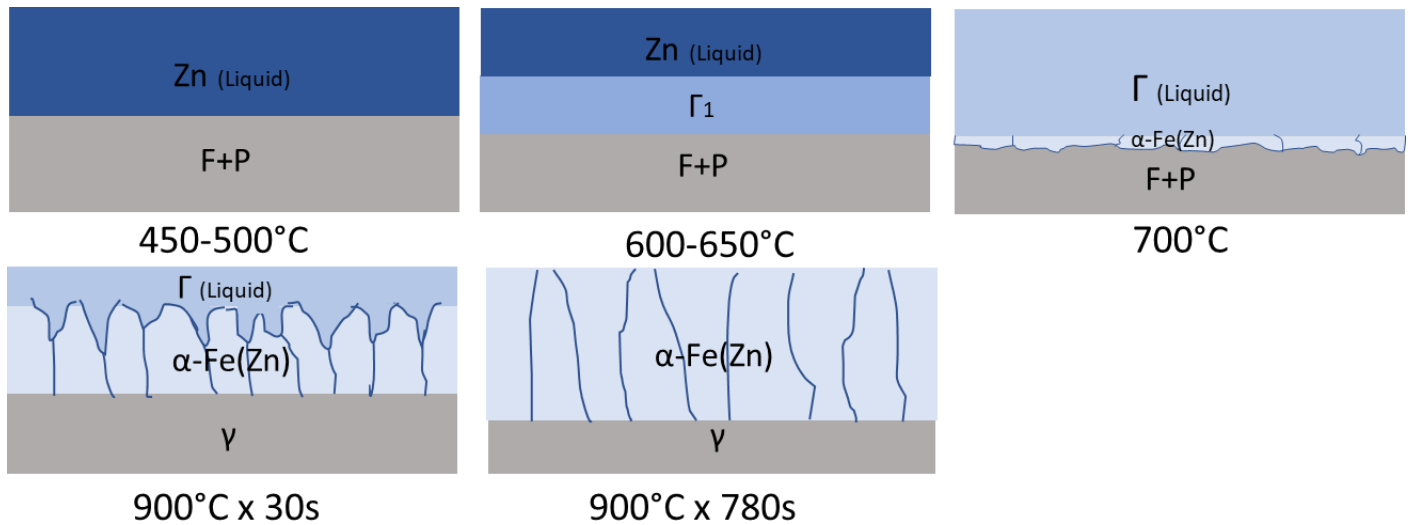


Figure 6. 1: A schematic of the microstructural evolution in GI70 22MnB5 DHPF samples as a function of temperature and holding time at 900°C.

SEM results (Figure 5.5 and Figure 5.6) indicated that by increasing the annealing time, the constituents of the coating microstructure changed while the coating thickness increased. After 30 s annealing, the coating consisted of a mixture of  $\alpha$ -Fe(Zn) +  $\Gamma$ -Fe<sub>3</sub>Zn<sub>10</sub> phases (Figure 5.5). The 300s annealing time was the transition time where the coating changed from a dual-phase ( $\alpha$ -

$\text{Fe(Zn)} + \Gamma\text{-Fe}_3\text{Zn}_{10}$ ) to a single-phase ( $\alpha\text{-Fe(Zn)}$ ) layer. And after annealing for 300s or longer, the coating microstructure was composed of only of  $\alpha\text{-Fe(Zn)}$  phase. Moreover, a wavy, detached oxide layer consisting of ZnO was found at the top surface of the coating. This lack of adhesion of the oxide layer was due to the presence of a liquid phase at the high annealing temperature [56]. Likewise, Figure 5.7 showed that squared coating thickness ( $X^2$ ) increased linearly as a function of holding time ( $t = 240\text{s}$  to  $780\text{s}$ ) which demonstrated that the  $\alpha\text{-Fe(Zn)}$  phase grew by diffusion, and the coating-substrate interface shifted towards the substrate. It was also observed that Zn concentration dropped from 65-70 at% for the 30 s time to 20 at% for the 780s annealing time. Relatively, the XRD results (Figure 5.8) confirmed the trends from the SEM data such that  $\Gamma\text{-Fe}_3\text{Zn}_{10}$  decreased by increasing annealing time and, after 300s holding time only the  $\alpha\text{-Fe(Zn)}$  solid solution was the main coating phase. The parabolic  $\Gamma\text{-Fe}_3\text{Zn}_{10}$  decreasing and  $\alpha\text{-Fe(Zn)}$  increasing trends emphasized diffusion couple growth again. Additionally, the fraction of formed ZnO was also found to increase slightly as annealing times increased.

The results of uniaxial tensile testing on uncoated 22MnB5 [51] indicated that the achieved mechanical properties of the uncoated 22MnB5 samples coincided with the industrial target mechanical properties of  $\sigma(\text{UTS}) \geq 1500$  MPa for a 22MnB5 PHS [1, 2, 51]. Tensile testing was performed on the planar die-quenched samples, the top surface (region 1) and the outer wall (region 4) of U-shaped die-quenched DHPF Zn-coated samples. Tensile results (Figure 5.9) obtained from the planar die and U-shaped DHPF Zn-coated samples revealed that as the annealing time increased, the UTS decreased until it no longer met the target UTS of at least 1500 MPa after annealing for 300s. It should be noted that the tensile samples from these three regions had very similar properties in terms of UTS and total elongation. The reduction in UTS

was because of substrate micro-cracking. Firstly, ex-situ micro-crack formation was used during tensile testing of the planar die-quenched samples. Secondly, the production of in-situ micro-crack formation during U-shaped DHPF process was studied.

## **6.1 Planar Die and U-shaped DHPF Process**

For the determination of the origin of micro-cracking, the microstructures prior to and after the application of tension (tensile testing or forming) were considered for the shortest austenization annealing time (30 s; with a coating composed of  $\alpha$ -Fe(Zn) +  $\Gamma$ -Fe<sub>3</sub>Zn<sub>10</sub>) and the longest austenitization annealing time (780s; with a coating composed of  $\alpha$ -Fe(Zn)). The PAGBs of the substrate and GBs of the  $\alpha$ -Fe(Zn) coating were studied before tensile testing to observe if zinc diffusion in these regions can contribute to later crack formation. Moreover, the micro-crack tips were investigated after tensile testing and micro-crack formation.

### **6.1.1 Ex-Situ Micro-Cracking**

Zn-coated PHS samples were fabricated using a water-cooled planar die-quench, followed by tensile testing at room temperature. After tensile testing, the 30TS and 780TS samples both exhibited crack formation and few of them showed a slight propagation into the substrate (Figure 5.10). It should be noted that some cracks formed in the coating of the as-quenched samples during the planar die-quenching DHPF process due to the applied compressive load (350 kPa). Also, Figure 5.11 depicted micro-crack formation with a penetration depth of over 15  $\mu$ m into the substrate close to the fracture surface in the necking region where stress triaxiality occurred.

However, for the purpose of a precise and easily-constrained micro-crack study, cracks were selected from the gauge length areas where uniform elongation had occurred.

Prior to tensile testing, grain boundaries of the coating and the PAGBs were studied using EBSD and STEM-EELS. The primary purpose of the EBSD application was to establish a phase map and to identify the coincident grain boundaries in between the grain boundaries of  $\alpha$ -Fe(Zn) and the PAGBs of the 30 s and 780s as-quenched samples, (Figure 5.12). A coating layer, a transition layer of Zn-enriched martensite, and a martensitic substrate layer were detected on the maps. Moreover, the zinc-enriched martensite layer in between the coating and the substrate on the EBSD maps (Figure 5.12), had a plate-like morphology with an approximate zinc content of 10-15 wt.%. This layer has also been observed and reported previously [57, 58].

For both samples in the presence or absence of the solidified liquid zinc ( $\Gamma$ -Fe<sub>3</sub>Zn<sub>10</sub>), zinc enrichment was observed along the PAGBs and the  $\alpha$ -Fe(Zn) GBs (Figure 5.16 and Figure 5.15). It should be noted that EELS semi-quantitative analysis showed that the zinc concentration in the coincident  $\alpha$ -Fe(Zn) GBs was 20 at% and, in the PAGBs, was 10-12 at% higher than that observed in the matrix (Figure 5.17). Thus, the semi-quantitative analysis demonstrated that the phase formed along the PAGBs was likely  $\alpha$ -Fe(Zn). The SAM-AES result for in-situ formed fracture surface for the 30 s as-quenched sample showed Zn-enrichment on the fracture surface in Zn-enriched martensite layer of the substrate (Figure 5.26). This observation also implied the presence of a thin  $\alpha$ -Fe(Zn) layer in the PAGB region. Therefore, the mentioned points were indicative of the occurrence of solid-state diffusion of zinc along the PAGBs of the substrate and GBs of the  $\alpha$ -Fe(Zn) coating. In the previous literature, zinc enrichment has been observed along the grain boundaries of  $\alpha$ -Fe(Zn) grains [2, 5, 6, 46]. However, here, solid-state diffusion of zinc

had contributed to the presence of zinc enrichment in PAGBs and had not been pointed out so far.

After tensile testing, it was observed that intergranular cracks were initiated in the coating and propagated along the coincident  $\alpha$ -Fe(Zn) grain boundaries and coincident PAGBs in the substrate. The STEM-EELS results (Figure 5.18 and Figure 5.19) showed Zn-enrichment along the crack and at the micro-crack tip in the PAGB region. It was observed that crack propagation stopped, and crack blunting occurred where PAGB zinc enrichment was no longer observed.

Figure 6.2 shows a schematic of the hypothesised micro-cracking mechanism in GI70 22MnB5 DHPF samples. Generally, due to higher diffusion rates in the grain boundaries compared to that of bulk diffusion [46, 59], zinc can be transported faster along the GBs and PAGBs, as was observed by the STEM-EELS maps (Figure 5.15 and Figure 5.16). A coincident PAGB and a GB in  $\alpha$ -Fe(Zn) became Zn-enriched as diffusion continued and a thin layer of  $\alpha$ -Fe(Zn) formed along the PAGBs as a result of the solid-state diffusion of zinc. Thus, because of grain boundary diffusion and formation of a brittle phase, when tension was applied on the sample, these zinc-enriched pathways (GBs and PAGBs) were prone to crack initiation and propagation. It can be seen from the schematic that the cracks initiated from a  $\alpha$ -Fe(Zn) grain boundary and propagated into a coincident PAGB of the substrate in which a brittle intermetallic GB layer ( $\alpha$ -Fe(Zn)) had formed previously as a result of zinc diffusion. During tensile testing, the crack propagated along this Zn embrittled interface as it debonded and fractured the weak  $\alpha$ -Fe(Zn) layer and propagated into the PAGB of the Zn-enriched martensite. After the micro-cracking stops at the PAGB, a thin pre-wetting layer ahead of the crack-tip was observed (Figure 5.18 and Figure 5.19).

Additionally, Figure 5.10 indicated that the tip of the micro-crack in the PAGB region appeared sharper for the samples with the shortest annealing time (30 s) whereas for 780s annealing time the micro-crack tip was more blunted. According to the micro-cracking mechanism, it can be concluded that the sharpness or the bluntness of the micro-crack was dependent on the amount of zinc in the  $\alpha$ -Fe(Zn) thin layer at the crack tip region in the PAGB. Relatively, Janik et al. observed that the appearance and the penetration depth of cracking in Zn-coated 22MnB5 DHPF relied on the amount of embrittler atoms feeding the crack [46].

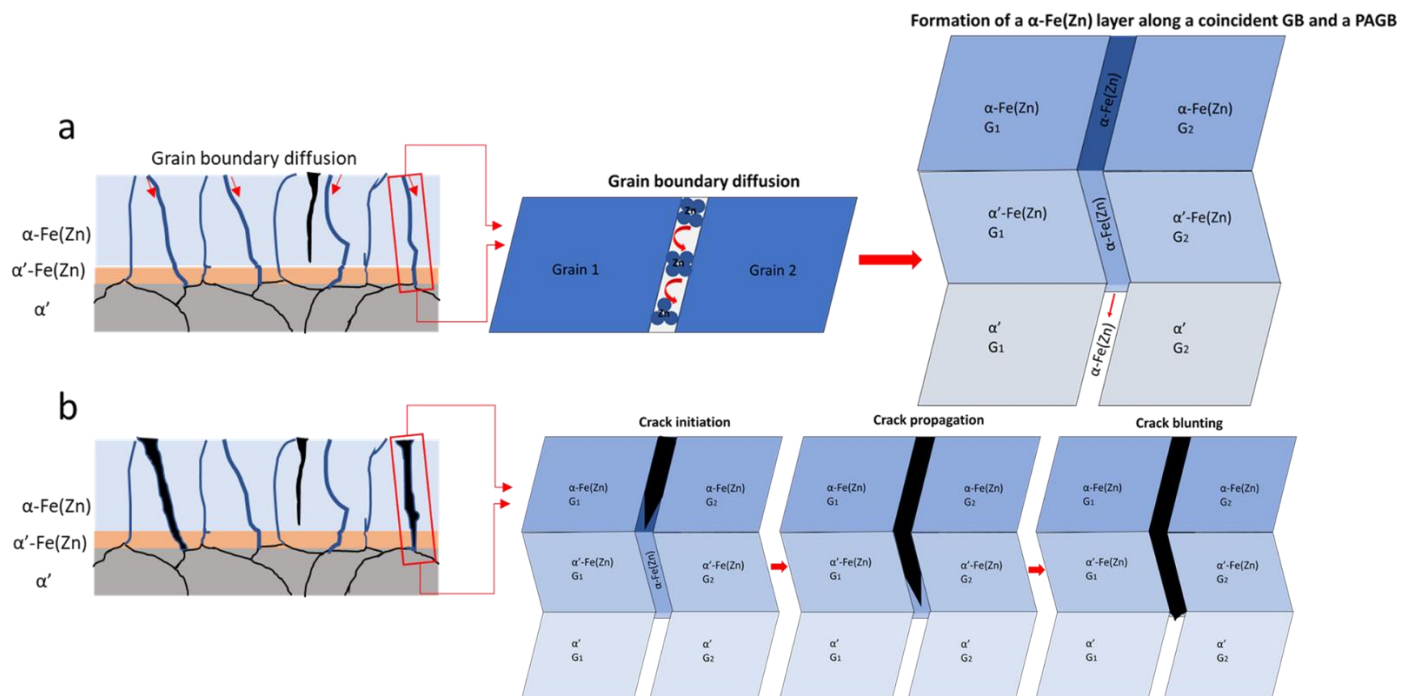


Figure 6. 2: A schematic of the proposed micro-cracking mechanism in Zn-coated DHPF steels annealed at 900°C: a) before the application of tension; solid-state diffusion of zinc along the grain boundaries results in the formation of a Zn-enriched  $\alpha$ -Fe(Zn) layer in the  $\alpha$ -Fe(Zn) GBs and in the PAGBs - Note that different shades of blue in the GBs indicate that Zn enrichment

was slightly declining from the coating to the Zn-martensite layer and finally to the fully lath martensitic substrate. b) after tensile testing; micro-cracking showed three stages of crack initiation, crack propagation, and crack blunting - Note that the cracking process initiated along the Zn-enriched  $\alpha$ -Fe(Zn) GBs and propagated along the weaker  $\alpha$ -Fe(Zn) layer in the PAGBs.

### 6.1.2 In-Situ Micro-Cracking

For in-situ micro-crack formation, samples were examined with a set of U-shaped DHPF substrates in which cooling and forming occurred at the same time. During U-shaped die-quenching, various strain paths were applied to different portions of the panels since the samples underwent a mixture of tension, compression, and bending [5] as shown in Figure 5.21 and Figure 5.22. Two regions were studied on the U-shaped die-quenched samples: the top surface (zone 1) and the outer wall surface (zone 4) (Figure 5.20) [5]. The top surface (zone 1) of the U-shaped samples was very similar to planar die-quenched samples (prior to tensile testing). Likewise, the outer wall surface (zone 4) on the U-shaped die-quenched samples had very similar condition as the planar die-quenched samples with post-quenching tensile testing. The outer wall of the deformed sample clearly underwent the highest tensile load, a strain of 8-10%, while the top surface had barely deformed under compression (Figure 4.6). Zn-enrichment was observed along the coincident PAGB and  $\alpha$ -Fe(Zn) GB at the top surface for both 30 s and 780s U-shaped die-quenched samples (Figure 5.24 and Figure 5.25). The concentration of diffused zinc along PAGBs fell within the zinc content of  $\alpha$ -Fe(Zn). Therefore, the presence of solid-state diffusion of zinc was confirmed with the U-shaped die-quenched press hardening process. Observations indicated that in the presence (30 s) or absence (780s) of  $Zn_{liq}$  which is the first prerequisite for LME, micro-crack formation was still observed. As a result, STEM-EELS maps observations for ex-situ and in-

situ micro-cracking at the crack tip and in the PAGB region of Zn-coated DHPF samples proposed a new mechanism for micro-cracking. It can be concluded that solid-state diffusion of zinc along  $\alpha$ -Fe(Zn) GBs and PAGBs weakened the grain boundaries by the formation of a thin layer of  $\alpha$ -Fe(Zn) and promoted micro-cracking.

## 7. Conclusions

The key findings of the present research are summarized as follows:

- As the annealing time increased, the zinc concentration in the coating decreased while the coating thickness increased parabolically. An annealing time of 300s was the transition time where the coating changed from a dual-phase ( $\alpha$ -Fe(Zn) +  $\Gamma$ -Fe<sub>3</sub>Zn<sub>10</sub>) to a single-phase ( $\alpha$ -Fe(Zn)) layer. The coating Zn concentration dropped from 65-70 at% for the 30 s annealing time to 20 at% for 780s annealing time. XRD analysis confirmed the SEM results that  $\Gamma$ -Fe<sub>3</sub>Zn<sub>10</sub> decreased with increasing annealing time, and the after 300s holding time only the solid solution  $\alpha$ -Fe(Zn) was the main coating phase. The decrease of  $\Gamma$ -Fe<sub>3</sub>Zn<sub>10</sub> and  $\alpha$ -Fe(Zn) increasing trends were found to be parabolic, which emphasized diffusion couple driven growth.
- Tensile results obtained from the planar die and U-shaped die-quenched DHPF Zn-coated samples revealed that as the annealing time increased, the UTS decreased until it no longer met the target UTS of at least 1500 MPa after annealing for 300s. The reduction in UTS was because of substrate micro-cracking.

- EBSD determined that for a  $\alpha$ -Fe(Zn) or dual phase  $\Gamma$ -Fe<sub>3</sub>Zn<sub>10</sub> +  $\alpha$ -Fe(Zn) coating layer, a transition layer of Zn-enriched martensite (Zn- $\alpha'$ ), and a martensitic ( $\alpha'$ ) substrate layer were present in the as-quenched samples. The Zn-enriched martensite layer in between the coating and the substrate had a plate-like morphology with an approximate zinc content of 10-15 wt.%.
- STEM-EELS results for both ex-situ and in-situ micro-cracking, in the absence of tension, indicated zinc enrichment in the PAGBs and GBs for both the 30 s and 780s DHPF samples. EELS semi-quantitative analysis showed the zinc concentration in the  $\alpha$ -Fe(Zn) GBs and was 20 at%, and in the coincident PAGBs was 10-12 at% higher than that observed in the matrix. The SAM-AES results for in-situ fracture of the as-quenched 30 s annealed sample also displayed zinc enrichment on the fracture surface in Zn-enriched martensite layer.
- STEM-EELS results for both ex-situ and in-situ micro-cracking, in the presence of tension, for the 30 s and 780s DHPF samples showed Zn-enrichment along the crack and at the micro-crack tip in the PAGB region. Crack propagation stopped, and crack blunting happened where PAGB Zn enrichment was no longer observed. The micro-crack tip for the 30 s annealed samples was sharper than that of 780s samples. The sharpness or bluntness of the micro-crack was dependent on the amount of zinc in the  $\alpha$ -Fe(Zn) thin layer at the crack tip region in the PAGB.
- A new mechanism was proposed for the origin of micro-cracking in Zn-coated 22MnB5 DHPF. A coincident PAGB in the substrate and a coincident GB in the  $\alpha$ -Fe(Zn) became Zn-enriched and a thin layer of  $\alpha$ -Fe(Zn) formed along the PAGBs as a result of the solid-state diffusion of zinc during austenitization annealing at 900°C. During tensile testing, the

micro-crack propagated along the weakened  $\alpha$ -Fe(Zn) grain boundaries and into the Zn-enrichment weakened coincident PAGBs.

## 8. References

- [1] D.W. Fan, B.C. De Cooman, State-of-the-Knowledge on Coating Systems for Hot Stamped Parts, 83(5) (2012) 412-433.
- [2] B.C. De Cooman, Jung, W., Jo, K.R., Sulistiyo, D.H, Cho, L., Zinc Coated Steel Sheets for Press Hardening Applications, Galvatech 2017 Conference Proceedings, Tokyo, Japan. ( November 12-16, 2017).
- [3] P. Belanger, J. Hall, J. Coryell, J. Singh, Automotive body press-hardened steel trends, International Symposium on the New Developments of Advanced High-Strength Steel, 2013, pp. 239-250.
- [4] L. Cho, H. Kang, C. Lee, B.C. De Cooman, Microstructure of liquid metal embrittlement cracks on Zn-coated 22MnB5 press-hardened steel, Scripta Materialia 90 (2014) 25-28.
- [5] C.W. Lee, W.S. Choi, L. Cho, Y.R. Cho, B.C. De Cooman, Liquid-metal-induced embrittlement related microcrack propagation on Zn-coated press hardening steel, ISIJ International 55(1) (2015) 264-271.
- [6] C.W. Lee, D.W. Fan, I.R. Sohn, S.-J. Lee, B.C. De Cooman, Liquid-metal-induced embrittlement of Zn-coated hot stamping steel, Metallurgical and Materials Transactions A 43(13) (2012) 5122-5127.

- [7] S. Shibli, B. Meena, R. Remya, A review on recent approaches in the field of hot dip zinc galvanizing process, *Surface and Coatings Technology* 262 (2015) 210-215.
- [8] A. Marder, The metallurgy of zinc-coated steel, *Progress in materials science* 45(3) (2000) 191-271.
- [9] E.A. Silva, Private Communication, (2005).
- [10] S. Maeda, Surface chemistry of galvanized steel sheets relevant to adhesion performance, *Progress in organic coatings* 28(4) (1996) 227-238.
- [11] P. Bicao, W. Jianhua, S. Xuping, L. Zhi, Y. Fucheng, Effects of zinc bath temperature on the coatings of hot-dip galvanizing, *Surface and Coatings Technology* 202(9) (2008) 1785-1788.
- [12] R. Kolley, R. Veit, M. Merklein, J. Lechler, M. Geiger, Investigation on induction heating for hot stamping of boron alloyed steels, *CIRP annals* 58(1) (2009) 275-278.
- [13] Y. Jin, Development of advanced high strength steels for automotive applications, *La Metallurgia Italiana* (6) (2011).
- [14] D. Horstmann, Reaction between iron and zinc, Zinc Development Association, London (1978).
- [15] R. Autengruber, G. Luckeneder, S. Kolnberger, J. Faderl, A.W.J.s.r.i. Hassel, *Surface and Coating Analysis of Press-Hardened Hot-Dip Galvanized Steel Sheet*, 83(11) (2012) 1005-1011.
- [16] W. Xiong, Y. Kong, Y. Du, Z.-K. Liu, M. Selleby, W.-H.J.C. Sun, Thermodynamic investigation of the galvanizing systems, I: Refinement of the thermodynamic description for the Fe–Zn system, 33(2) (2009) 433-440.
- [17] A.H. Committee, *Properties and Selection: Irons, Steels, and High-Performance Alloys*, ASM International (1990).

- [18] C.A. Sciammarella, F.M. Sciammarella, *Experimental mechanics of solids*, John Wiley & Sons 2012.
- [19] S. Lynch, Metal-induced embrittlement of materials, *Materials Characterization* 28(3) (1992) 279-289.
- [20] T. Kurz, G. Luckeneder, T. Manzenreiter, H. Schwinghammer, A. Sommer, Zinc coated press-hardening steel-challenges and solutions, SAE Technical Paper, 2015.
- [21] P. Drillet, R. Grigorieva, G. Leuillier, T. Vietoris, Study of cracks propagation inside the steel on press hardened steel zinc based coatings, *La Metallurgia Italiana* (1) (2011).
- [22] S. Lynch, Solid-metal-induced embrittlement of aluminium alloys and other materials, *Materials Science and Engineering: A* 108 (1989) 203-212.
- [23] P. Gordon, Metal-Induced embrittlement of metals—an evaluation of embrittler transport mechanisms, *Metallurgical Transactions A* 9(2) (1978) 267-273.
- [24] F. Rhines, A. Gokhale, *Embrittlement by Liquid and Solid Metals*, Edited by MH Kamdar (1984).
- [25] N.M. Parikh, *Conference on Environment Sensitive Mechanical Behaviour* edited by A. R. C. Westwood and N. S. Stoloff, (Gordon and Breach, New York, 1966) p. 563.
- [26] P. Hancock, M. Ives, The role of plastic deformation in liquid metal embrittlement, *Canadian metallurgical quarterly* 10(3) (1971) 207-211.
- [27] D. Jiang, C. Wang, J. Yu, Z. Gao, Y. Shao, Z. Hu, Cleavage and intergranular fracture in Al–Mg alloys, *Scripta materialia* 49(5) (2003) 387-392.
- [28] W. Grubb, Cadmium metal embrittlement of Zircaloy-2, *Nature* 265(5589) (1977) 36.

- [29] J.C. Lynn, W.R. Warke, P. Gordon, Solid metal-induced embrittlement of steel, *Materials Science and Engineering* 18(1) (1975) 51-62.
- [30] D.C. Drucker, J.J. Gilman, Fracture of solids(Proceedings of an International Conference), Metallurgical society of conferences, Interscience publishers, 1963.
- [31] S. Dinda, W. Warke, The effect of grain boundary segregation on liquid metal induced embrittlement of steel, *Materials Science and Engineering* 24(2) (1976) 199-208.
- [32] C. Preece, ADSORPTION-INDUCED EMBRITTLEMENT OF METALS, State Univ. of New York, Stony Brook, 1972.
- [33] M. Nicholas, C. Old, Liquid metal embrittlement, *Journal of Materials Science* 14(1) (1979) 1-18.
- [34] P.J.L. Fernandes, D.R.H. Jones, Mechanisms of liquid metal induced embrittlement, *International Materials Reviews* 42(6) (1997) 251-261.
- [35] A. Griffith, The phenomenon of rupture and flow in solids. *Phil, Trans, Roy. Soc. A221*, (1920).
- [36] E. Orowan, Fatigue and fracture of metals, SYMPOSIUM AT MASSACHUSETTS INSTITUTE OF TECHNOLOGY. New York, 1950.
- [37] R. Eborall, P. Gregory, The mechanism of embrittlement by a liquid phase, *J Inst Met* 84 (1956) 88-90.
- [38] N. Stoloff, T. Johnston, Crack propagation in a liquid metal environment, *Acta Metallurgica* 11(4) (1963) 251-256.
- [39] A. Westwood, C.M. Preece, M.H. Kamdar, Adsorption-induced brittle fracture in liquid-metal environments, *Engineering Fundamentals and Environmental Effects*, Elsevier 1971, pp. 589-644.

- [40] A. Westwood, C. Preece, M.H. Kamdar, APPLICATION OF A CRACK PROPAGATION CRITERION TO LIQUID-METAL EMBRITTLEMENT--CLEAVAGE OF ALUMINUM MONOCRYSTALS IN LIQUID GALLIUM, ASM TRANS QUART 60(4) (1967) 723-725.
- [41] T. Slavin, N. Stoloff, Embrittlement cracking of metal glasses, Mater. Sci. and Eng 68(1) (1984) 55-71.
- [42] S. Lynch, Environmentally assisted cracking: overview of evidence for an adsorption-induced localised-slip process, Acta Metallurgica 36(10) (1988) 2639-2661.
- [43] S.P. Lynch, Mechanisms and Kinetics of Environmentally Assisted Cracking: Current Status, Issues, and Suggestions for Further Work, Metallurgical and Materials Transactions A 44(3) (2013) 1209-1229.
- [44] T. Reiley, Creep cavity observation using liquid metal embrittlement, Scr. Metall.:(United States) 15 (1981).
- [45] R. Van Stone, J. Low, J. Shannon, Investigation of the fracture mechanism of Ti-5Al-2.5 Sn at cryogenic temperatures, Metallurgical Transactions A 9(4) (1978) 539-552.
- [46] V. Janik, Y. Lan, P. Beentjes, D. Norman, G. Hensen, S. Sridhar, Zn Diffusion and  $\alpha$ -Fe(Zn) Layer Growth During Annealing of Zn-Coated B Steel, Metallurgical and Materials Transactions A 47(1) (2016) 400-411.
- [47] M. Fleischanderl, S. Kolnberger, J. Faderl, G. Landl, A.E. Raab, W. Brandstätter, Method for producing a hardened steel part, Google Patents, 2011.
- [48] K. Imai, Y. Yoshikawa, T. Toki, T. Nishibata, K. Uematsu, M. Uchihara, T. Takayama, South East Asia Iron Steel Inst, Q 34 (2005) 47.

- [49] T. Manzenreiter, M. Rosner, T. Kurz, G. Brugger, R. Kelsch, D. Hartmann, A. Sommer, Challenges and advantages in usage of zinc-coated, press-hardened components with tailored properties, *BHM Berg-und Hüttenmännische Monatshefte* 157(3) (2012) 97-101.
- [50] ASTM International, PA, , “ASTM A90/A90M-13, Standard Test Method for Weight [Mass] of Coating on Iron and Steel Articles with Zinc or Zinc-Alloy Coatings,” (2013.).
- [51] C.E. Dever, McMaster University, Effect of coating microstructure on the electrochemical properties of continuous galvanized coatings on press hardened steels, (2018).
- [52] J.R. Davis, Tensile testing, ASM international, 2004.
- [53] Vanessa, Pickerd. "Optimisation and Validation of the ARAMIS Digital Image Correlation System for use in Large-scale High Strain-rate Events, Maritime Division DSTO Defence." Science and Technology Organisation (2013).
- [54] F. Hild, S. Roux, Digital image correlation: from displacement measurement to identification of elastic properties—a review, *Strain* 42(2) (2006) 69-80.
- [55] Cayron, C., ARPGE: a computer program to automatically reconstruct the parent grains from electron backscatter diffraction data. *Applied Crystallography*, October 2007.
- [56] S. Hayashi, T. Sekimoto, K. Honda, T. Kinoshita, K. Tanaka, K. Ushioda, T. Narita, S. Ukai, The effect of S and Mn on the high-temperature oxidation and scale spallation behavior of low-carbon steels, *ISIJ international* 49 no.12 (2009) 1938-1944.
- [57] H. Peng, W. Peng, R. Lu, G. Wu, J. Zhang, Diffusion and cracking behavior involved in hot press forming of Zn coated 22MnB5, *Journal of Alloys and Compounds* (2019) 195-205.

[58] H. Järvinen, M. Honkanen, M. Patnamsetty, S. Järn, E. Heinonen, H. Jiang, P. Peura, Press hardening of zinc-coated boron steels: Role of steel composition in the development of phase structures within coating and interface regions, *Surface and Coatings Technology* 352 (2018) 378-391.

[59] E.S. Wajda, Grain boundary self-diffusion in zinc, *Acta Metallurgica* 2.2 (1954) 184-187.